651

HADRON PRODUCTION IN HIGH ENERGY NEUTRINO INTERACTIONS

by

Jaswent Singh Chima

A thesis submitted for the degree
of Doctor of Philosophy of the
University of London

Department of Physics
Imperial College
London SW7

January 1981

To   My Mother

ABSTRACT

Results are presented based on data obtained from high energy neutrino interactions in the Big European Bubble Chamber, BEBC, filled with a heavy mixture of Ne/H_2 and exposed to a narrow-band beam. Detailed tests are made, based on the structure of the observed hadrons, of the theory of Quantum Chromodynamics (QCD). A comparison is also made of the jet properties of the hadrons resulting in neutrino interactions with those resulting in e^+e^- annihilations and hadron interactions.

Preface

The results presented in this thesis are based on data taken during two exposures of the Big European Bubble Chamber (BEBC) filled with a heavy Neon-Hydrogen mixture, and exposed to the CERN Narrow Band Beam. During the first exposure, which took place in early 1977, (WA19), 106,000 neutrino and 181,000 anti-neutrino pictures were taken, and during the second exposure, which took place in late 1978, (WA47), 156,500 neutrino and 261,000 anti-neutrino pictures were taken. The film was divided amongst the members of the, (ABCLOS), collaboration to be measured independently. The final data summary tape made available to each laboratory contained the entire data sample.

The author was involved in the closing stages of the event checking of the WA19 data, but participated in all stages, ie. data taking, event measurement, and event checking, of WA47. Since the final data samples were not available until late 1980, parts of the physics results, particularly those on anti-neutrino interactions presented in chapter 4, are based on less than the full data samples.

The aim of this experiment was to obtain neutrino and anti-neutrino data, at the highest possible energies currently available, suitable for total cross-section measurements and the study of charged current and neutral current phenomena. The analysis presented in this thesis concentrates on the study of final state hadrons resulting from charged current interactions.

CONTENTS

CHAPTER 4 Inclusive Study of the Hadronic System

CHAPTER 5 Hadron Structure in Momentum Space

CONTENTS (continued)

CHAPTER 6 Fragmentation Functions

CONTENTS (continued)

CHAPTER 1

Theoretical Background

1.1 Introduction

A brief summary of the theory of weak interactions, and the application of this to neutrino interactions is presented. The kinematical variables used are defined, and the hypotheses behind the quark-parton model, and the basic ideas behind QCD are presented.

1.2 Weak Interactions

The theoretical study of weak interactions began with the work of Fermi (1934) who described β-decay using a vector current - current interaction in analogy with the well understood electromagnetic case. This description however was insufficient for a general weak interaction process which may violate parity (Lee and Yang 1956, τ-θ paradox), and of the possible forms of the current operator in the weak interaction Langrangian; scalar, vector, axial vector, and pseudoscalar; experiments on lepton polarisation showed that only V and A interactions could produce the observed lepton helicities. The interference between V and A interactions in mixed transitions, such as that determined from a study of the angular correlations in the decay of polarised neutrons ($n \to p + e + \nu$) suggested the correct form of the current to be (V - A).

This pure (V - A) description however holds good at low energies only since it predicts a weak process cross-section proportional to the total energy, so violating unitarity, (conservation of probability), at high energies. The problem arises because this, 'four-fermion' interaction has zero range. If however the weak interaction is assumed to be mediated by an intermediate vector boson, w, in analogy with QED where interaction between two electrons is produced by the exchange of a photon, the weak interaction process does become non-local. Since weak interactions are short range, the w boson must have a large mass and since weak currents are electric charge changing ($n \rightarrow p$, $e^- \rightarrow \nu$) the w boson, besides having unit spin like the photon, also carries an electric charge. The cross-section for weak processes then rises logarithmically with energy, so that the violation of unitarity recurs at very high energies.

Gauge theories offer a way of converging the weak interaction theory. In this framework the bad high energy behaviour of the cross-section is cancelled by having extra exchange particles, besides the w - boson, which cancel the divergent process. In a particular example the Weinberg-Salam model, a neutral current, z^o, is introduced to achieve this. In fact there are four vector bosons in the model, three massive, w^+, w^-, z^o, and one massless, A, the photon. The neutral members are given by:

$$z^o = -w_3 \cos\theta_W + B \sin\theta_W$$

$$A = w_3 \sin\theta_W + B \cos\theta_W$$

so that the weak and electromagnetic interactions are unified, being described by a single Langrangian. This gives a theoretical reason for comparing $e^+ e^-$ and neutrino data; they would be expected to show similar properties on the basis of the basic interaction being similar. Any differences may be attributable to differences in the quark 'dressing' process or to QCD effects (section 1.4). W_3 is a member of the triplet (j = 1): (w^+, w^-, w_3), and B is a singlet boson (j = 0) with couplings g and g' respectively to the usual lepton currents. The only free parameter of the model is θ_W, (Weinberg-Salam angle) which is given by the ratio of the couplings: $\tan\theta_W = g'/g$. The mass scale of the w-boson is given by the coupling of the photon:

$$m_W^2 = \frac{e^2}{\sin^2\theta_W} \frac{1}{4\sqrt{2}G}$$

e being the electron charge and G the Universal Fermi constant. Thus $m_W \sim 38/\sin\theta_W \sim 80$ Gev using the currently determined value of $\sin^2\theta_W \sim 0.25$. Thus observation of the w-boson in fixed target experiments such as this one is unlikely.

The first evidence for the neutral current z^0, was the observation of the reaction $\bar{\nu}_\mu + e^- \rightarrow \bar{\nu}_\mu + e^-$, (Gargamelle 1973) which is only predicted by the Weinberg-Salam model, and not by the standard (V - A) theory. The Weinberg-Salam model is thus highly favoured to give the correct description of weak interactions.

1.3 Neutrino Interactions

The above picture suggests neutrino interactions are mediated by a charged vector boson, (only charged current interactions will be considered) which couples to the parton isospin. The following reactions are then possible:

$$\begin{aligned} \nu + d &\rightarrow \mu^- + u \\ \bar{\nu} + u &\rightarrow \mu^+ + d \end{aligned} \qquad (1)$$

with contamination from the sea quarks:

$$\begin{aligned} \nu + \bar{u} &\rightarrow \mu^- + \bar{d} \\ \bar{\nu} + \bar{d} &\rightarrow \mu^+ + \bar{u} \end{aligned} \tag{2}$$

where d, u are the eigenquarks of strong interactions[†]. Since the Cabibbo angle θ_c, ($\sim 15^0$), is small the contribution from $\bar{s} \rightarrow \bar{u}$ and $s \rightarrow u$ is suppressed by $\sin^2 \theta_c \sim (0.26)^2$.

Diagramatically the neutrino reaction can be represented by:

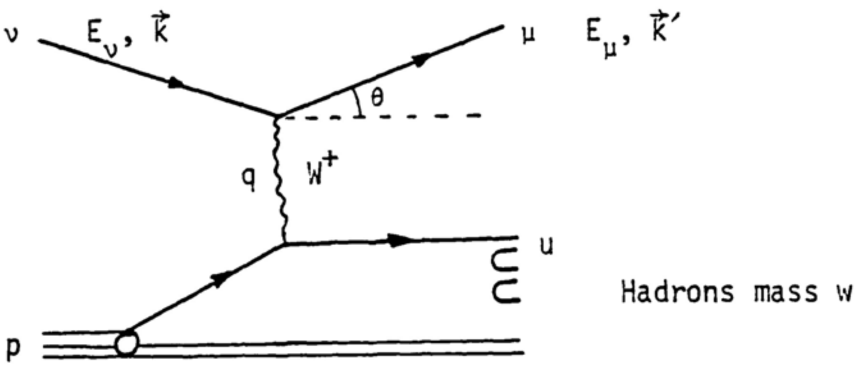

Fig 1.1

In the theory of weak interactions sketched out above, the Langrangian of the process can be represented by a w-boson propagator, a lepton

---

[†] The eigenquarks of weak isospin are related to those of strong interactions by:

$$d_W = d \cos\theta_c + s \sin\theta_c$$

$$s_W = s \cos\theta_c - d \sin\theta_c$$

current, describing the well understood upper, leptonic vertex, and a quark current, describing the lower, hadronic vertex. This leads to a cross-section for an isoscalar target of the form:

$$\frac{d^2\sigma^{\nu,\bar{\nu}}}{dQ^2\,d\nu} = \frac{G^2E_\mu}{2\pi E_\nu}\left[2W_1^{\nu,\bar{\nu}}\sin^2\frac{\theta}{2} + W_2^{\nu,\bar{\nu}}\cos^2\frac{\theta}{2} \mp W_3^{\nu,\bar{\nu}}\frac{(E_\nu+E_\mu)}{m_p}\sin^2\frac{\theta}{2}\right] \quad -(3)$$

where θ is the lab scattering angle, and the terms $W_i(Q^2,\nu)$, $i = 1,3$ are scalars that describe the hadronic vertex in terms of the independent Lorentz invariants constructed from the four vectors p and q given by:

$$\begin{aligned} Q^2 &= -(k-k')^2 = -q^2 \\ \nu &= \frac{p.q}{m_p} = E_\nu - E_\mu \end{aligned} \quad (4)$$

These are related through the invariant w which gives the hadron mass:

$$w^2 = (p+q)^2 = m_p^2 + 2m_p\nu - Q^2 \quad (5)$$

(The variable y, used later, is defined by: $y = \nu/E_\nu$).

The kinematic regions of interest of the reactions (1) are shown in fig 1.2, where the neutrino data is shown on a Q^2 vs ν plot. The study presented in this thesis is concerned with the deep inelastic region, away from the quasi-elastic boundary.

1.4 The Parton Model

The scattering of high energy electrons with a significant probability of large energy and momentum transfers, (Panofsky 1968) suggests that the proton charge is localised to a few scattering centres. The energy and angular distributions of the scattered electrons appear as if from point-like spin 1/2 Dirac particles. This result combined with the data on neutrino interactions indicates that these structureless constituents have the same quantum numbers as quarks(q) which successfully classified the hadrons as mesons consisting of $q\bar{q}$ pairs and baryons of qqq in various states of orbital angular momentum, each quark having spin 1/2 and possible unitary spin states u,d,s,c,b(t...), and fractional charge.

The idea of considering hadrons as bound states of pointlike constituents, partons, was introduced by Feynman to describe data on high energy scattering experiments |2|; and applied to lepton scattering by Bjorken and Paschos |3|. This naive parton model contains the features |2,4|:

i) Although the nucleon is a tightly bound system, partons can be treated as quasi-free by choosing a Lorentz frame such that the nucleon moves relativistically. Thus the internal motion of the partons due to their strong interactions will be slowed down by time dilation and during the time of the current interaction the internal interactions can be ignored. Under these conditions the incoherent impulse approximation becomes valid. Implicitly this means that final state interactions which confine the quarks act at large space-time distances of the order of the proton size, much larger than the parton size, and the time-scale of the current parton interaction. Such a relativistic frame is the Breit frame in which the virtual boson has four-momentum: $q = (0, -Q, \vec{0})$, where Q is the z component of three-momentum transfer and the proton has four-momentum: $p = (Q/2x, Q/2x, 0)$, (chapter 6.3), x being defined in (iii).

ii) The rest mass of the intermediate parton with which the w-boson interacts is negligible, so its four-momentum is given by:

$$k = (E_k, k_z, k_t)$$

with $$E_k = (k_z^2 + k_t^2 + k^2)^{\frac{1}{2}}$$

where k^2 is the virtual mass of the off-shell parton and k_z is given fraction, f, of the proton longitudinal momentum: $k_z = f.Q/2x$. In the parton model it is assumed the distribution of virtual masses and transverse momenta (chapter 4.6) for partons in the proton is damped, so that terms of order k^2/Q^2 can be neglected. This gives $E_k \sim f.Q/2x$ when k^2 and k_t^2 are ~~be~~ neglected; the parton acts like a real on-mass shell parton and its momentum is proportional to that of the proton:

$$k \simeq (f.\frac{Q}{2x}, f.\frac{Q}{2x}, 0)$$

Since the interacting parton is quasi-real, the scattering process can be described by a quark distribution function, F(f), which gives the probability of finding a parton with fraction, f, of the proton momentum, and a factor proportional to the point-like cross-section for the scattering of the parton on the virtual boson, $\sigma_{point}(k + q)$, (first term on the L.H.S of equation 7). Since $(k + q)^2$ must equal the squared mass of the final parton:

$$(k + q)^2 = +q^2 \left(1 - \frac{f}{x}\right) = 0$$

ie $$\sigma_{point} (k + q) \propto \delta\left(\frac{f}{x} - 1\right)$$

so that only partons of momentum fraction $f = x$ can interact with the virtual boson in the Breit frame.

iii) In the limit ν and $Q^2 \rightarrow \infty$, the inelastic boson nucleon scattering can be treated like elastic boson - parton scattering. From equation (5), the invariant mass of the system is given by

$$w^2 = m_q^2 + 2m_q\nu - Q^2 \qquad (6)$$

where m_p, the proton mass has been replaced by m_q, the quark-parton mass. Since for elastic scattering off the parton $w^2 = m_q^2$, equation (6) gives $2m\nu = Q^2$,

ie $$x = \frac{Q^2}{2m_p\nu} = \frac{m_q}{m_p}$$

Thus elastic scattering is described by just one dimensionless variable and no explicit scale of Q^2 is present. This is the phenomena of Bjorken scaling, |3|, that in the limit of Q^2 and $\nu \rightarrow \infty$, when masses became unimportant, and if there is no intrinsic mass in the system greater than m_p, then the cross-section should be independent of this mass, m_p and so the physics is independent of the scale. This means that the structure functions cannot depend on Q^2 and ν, because these have scale, and must depend on a dimensionless quantity eg x:

$$\begin{aligned} W_1\,(Q^2, \nu) &\rightarrow F_1\,(x) \\ \nu W_2\,(Q^2, \nu) &\rightarrow F_2\,(x) \\ \nu W_3\,(Q^2, \nu) &\rightarrow F_3\,(x) \end{aligned}$$

Deviations from Bjorken scaling are discussed in chapter 6. The differential cross-section given by equation (3) is then given in terms of the variables x and y:

$$\frac{d^2\sigma^{\nu,\bar{\nu}}}{dx\,dy} = \frac{G^2 m_p E_\nu}{\pi}\left[(1 - y - \frac{xym_p}{2E_\nu})F_2 + xy^2F_1 \mp (y - \frac{y^2}{2})xF_3\right] \qquad (7)$$

The coefficient of F_2 in terms of m_p can be dropped since $E_\nu >> m_p$. The factor $G^2m_pE_\nu/\pi \simeq 1.5\ 10^{-38}\ cm^2\ E_\nu$. The structure functions represent the sea quark (F_2), and valence quark, (xF_3) distributions:

$$\begin{aligned} F_2(x) &= q(x) + \bar{q}(x) \\ xF_3(x) &= q(x) - \bar{q}(x) \end{aligned}$$

with $F_2 = 2xF_1$ (Callan-Gross relation)

1.5 Quantum Chromodynamics

The discovery of the (V - A) stucture of the charged weak current lead to the non-abelian gauge theory constructed from su(2) x u(1), namely Weinberg-Salam model, to describe the electromagnetic and weak interactions (section 1.1). The phenomenological successes of the Quark Parton Model (QPM) have shown that hadrons are composite, and so it becomes necessary to find an adequate theory of q-q interaction, and account for the short comings of the QPM in providing a complete description. A theory which seems to have a good chance of doing this is Quantum Chromodynamics (QCD), tests of which are the main topic of this thesis |5|.

QCD involves only quark fields: ψ_i^α α = colour charge
i = flavour
and gauge gluon fields: A^β β = colour.

Since gluon (g) field is flavour insensitive, flavour plays no dynamical role in QCD (unlike weak interactions where the weak interaction current couples to the flavour), and it is the colour which distinguishes the 3 colours of quarks that is the active ingredient.

The colour quantum number gives an exact SU(3) symmetry of QCD, so that the gluons are octets in colour space and singlets in flavour, thus carrying the quantum numbers of a $q\bar{q}$ pair. Quarks interact by the emission of gluons, such that colour is conserved, eg a red quark (R_q) can go to a green quark (G_q) by emitting a red anti-green gluon ($R\bar{G}_g$). $R_q \rightarrow G_q + R\bar{G}_g$. Since gluons carry a colour charge, they can also self-interact:

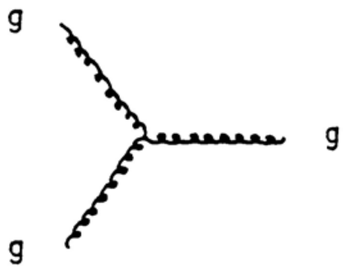

and observation of this process, eg through the decay of heavy vector mesons ψ, $\Upsilon \rightarrow ggg$, is a distinct test of the theory. The presence of this vertex, and the fact that gluons carry a higher colour charge which means they can Bremsstrahlung more efficiently, is expected to produce gluon jets which are more dispersed in momentum than quark jets.

The fact that (colour) charge is exchanged between the quark and gluon fields, means that the effective charge is not tied to the quark but spreads over the adjacent fields so that at high Q^2, (small distance), only part of the charge is seen, and at low Q^2 the whole charge is seen. This leads to a running coupling constant:

$$g \sim \frac{\text{constant}}{\ln(Q^2/\Lambda^2)}$$

where Λ is a free parameter of the theory which determines a mass Λ, and a length Λ^{-1}.

For $Q < \Lambda$, the infrared or 'non-perturbative' region, the coupling becomes large. It is believed that the effective coupling becomes strong enough to confine quarks, (and gluons) which have never been observed as free particles inside hadrons. The hadrons are of the size Λ^{-1}, and the hadron masses are $\sim\Lambda$. With $\Lambda \sim 1$ Gev, the effective coupling becomes: $g(Q^2 \sim 1) \sim 1$. Such a large value of the coupling means perturbation theory breaks down, and the mechanism which causes confinement in QCD is unproven.

The region $Q > \Lambda$ leads to a decreasing value of the coupling, and 'asymptotic-freedom' in the ultraviolet or 'perturbative' region thus allowing perturbation calculations to be performed. The fact that at short distance, (large Q^2), the effective coupling tends to zero means that the assumptions of the QPM are recovered. At these distances the dominant interquark force will arise from single gluon exchange.

Thus in the context of QCD a picture emerges of how 'jets' of final state hadrons are produced in deep inelastic neutrino scattering.

Consider the scattered quark in reaction (1) loosing all its energy by successive emission of collinear gluons. The gluon couples to a $q\bar{q}$ pair, so consider the decay of this pair in its centre of mass system The $q\bar{q}$ will be the source of a colour, 'chromoelectric', field which will be confined into tubes of flux between the q and $\bar{q}$, (because of self interactions of the gluon), which are the minimum energy configerations, by a process assumed to be similar to the Meissner effect in superconductivity.

As the $q\bar{q}$ separates the energy gets converted into field energy, and the process continues until it becomes energetically favourable to produce a $q\bar{q}$ pair from the vacuum, which breaks the flux tubes. The new $q\bar{q}$ pair being found somewhere between the original pair in momentum space. The process repeats until all the kinematic energy is used up and a jet of hadrons emerges, strongly collimated into a one-dimensional configuration in momentum space, (fig 1.3a). The QCD picture of hadron production in neutrino interactions is shown in Fig 1.3b.

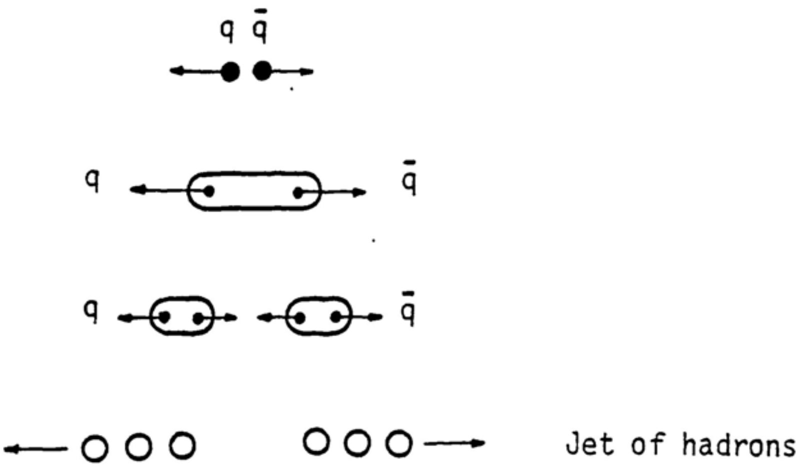

Fig 1.3a

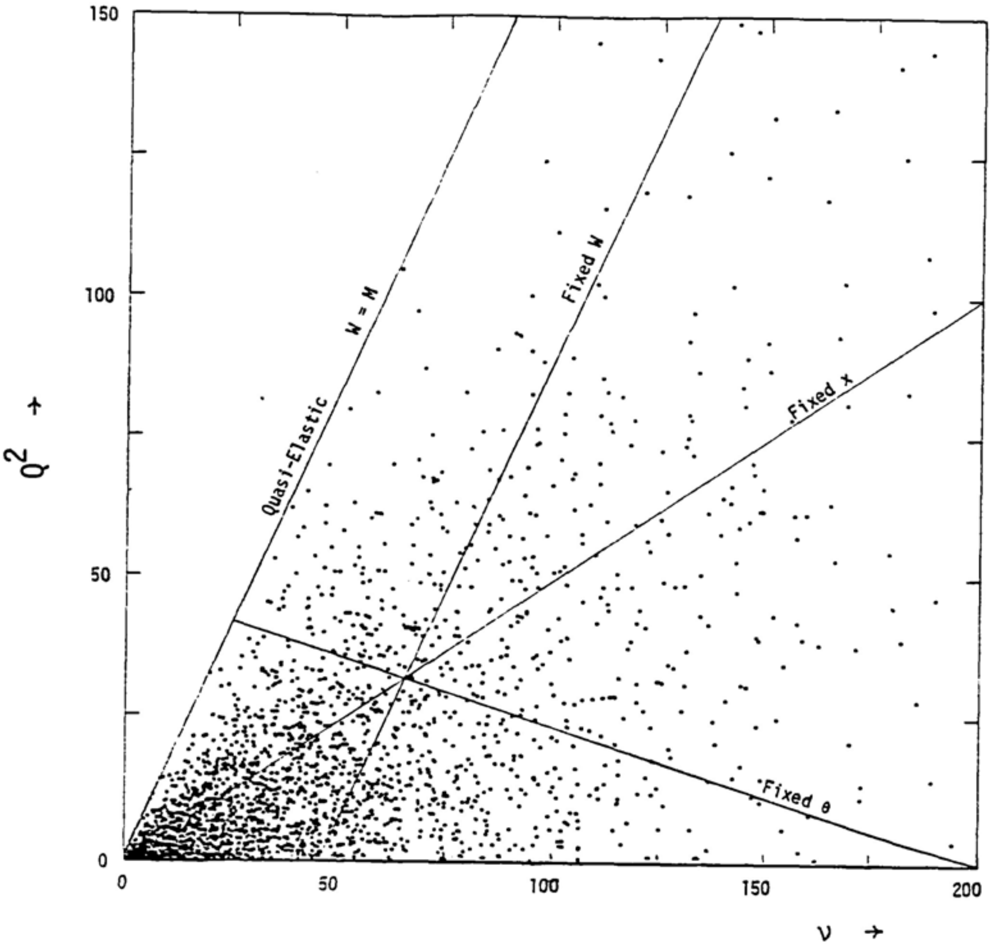

Fig 1.2 Q^2 vs ν plot for the neutrino data

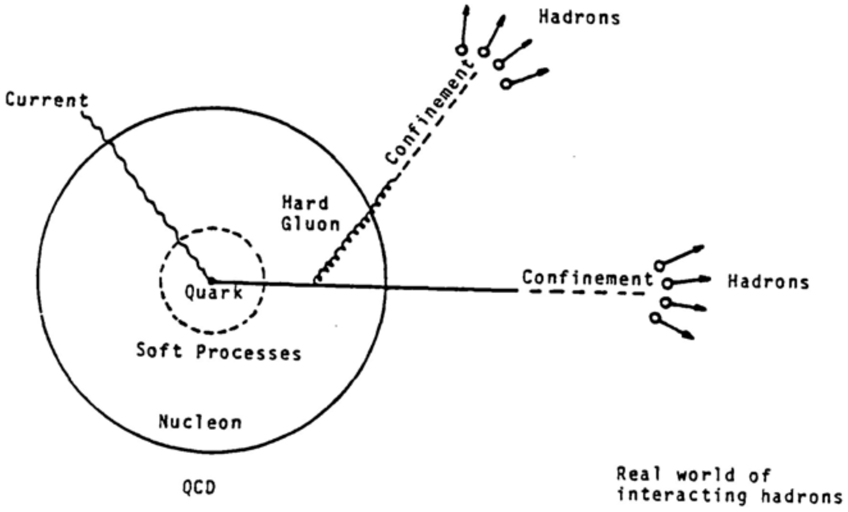

Fig 1.3b QCD picture of hadron production in neutrino interactions

It is implicity assumed that the global kinematic features of the jets of hadrons which are observed survive the confinement forces which convert the quarks and gluons into hadrons.

In the chain of fig 1.3 the original quark could also radiate a hard gluon, so that instead of the quark producing a thin pencil-like jet, a broad, or even two distinctly separated jets will be produced. In neutrino interactions it is the struck quark, which is in an excited state, that is likely to radiate a hard gluon. The QCD diagrams which contribute up to first order are:

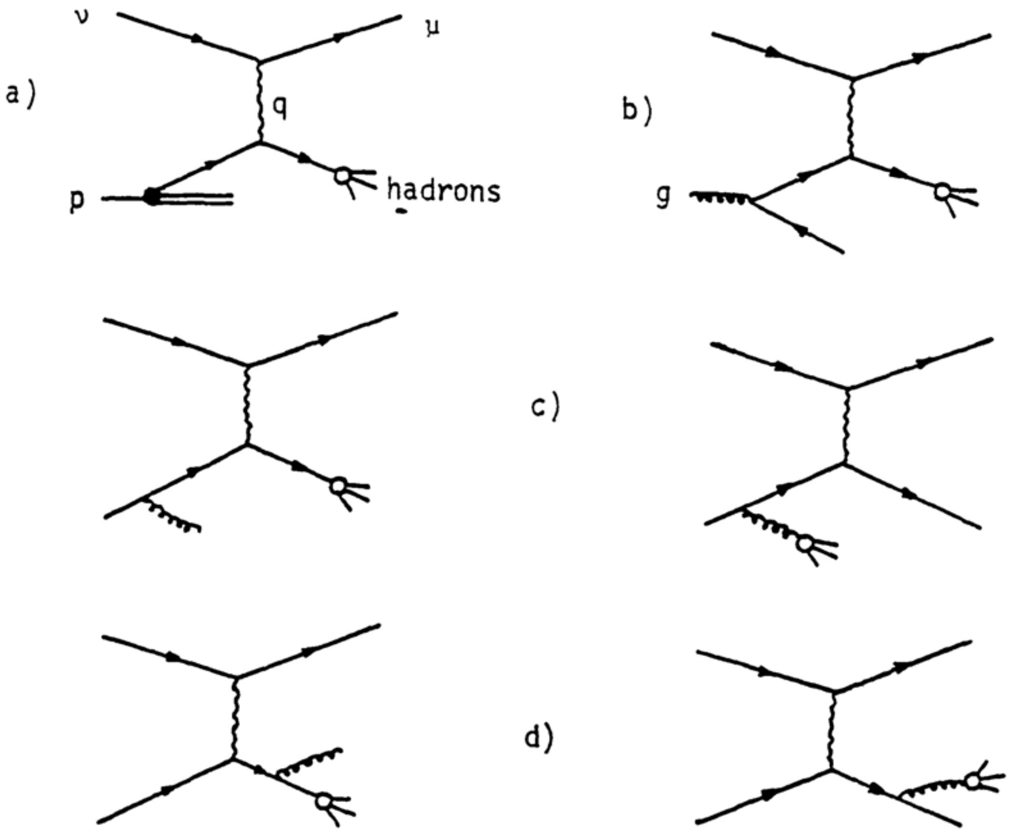

Fig 1.4

where the solid lines represent quarks, (and anti-quarks) the wavy lines the current, and the curly lines gluons. The solid blob, (shown in the zeroth order QCD or QPM diagram, a), represents Q^2 dependent structure functions and the open blob represent z dependent quark and gluon fragmentation functions. The contributions from higher order QCD are discussed in chapter 6.

The emission of soft or collinear gluons in some hadronic processes leads, in perturbative QCD calculations, to logarithmic infrared divergences. The theoretical predictions in which these singularities are absent are based on two approaches

i) Final states are summed so as to cancel out different infrared singular contributions. Test of predictions based on this approach are presented in chapter 4 and 5.

ii) The infrared singularities are absorbed into structure or fragmentation functions which are hopefully universal, ie independent of the particular process studied. Tests of predictions based on this approach are presented in chapter 6.

Since QCD is a fast developing theory, some of the predictions tested in this thesis may change as the methods of calculation become more sophisticated. This is exemplified by the discussion of chapter 5.3.1b.

References

1 D H Perkins, Introduction to High Energy Physics, (Addison Wesley 1972)
Rutherford School for Young High Energy Physicists (1978) 158
Editor C Lewellyn-Smith, Weak and Electromagnetic Interactions at High Energy (North-Holland 1976) 311

2 R P Feynmann, Phys. Rev. Letters 23 (1969) 1415

3 J D Bjorken and E A Paschos Phys. Rev. 158 (1969) 1975
J D Bjorken Phys. Rev. 179 (1969) 1547

4 R P Feynmann, Photon Hadron Interactions (Benjamin Reading, 1972)

Editor J T T Van, Recontre de Moriond XII, Vol. 2 (1978) 395

5 H D Politzer, Phys. Rep. 14c (1974) 129

W W Marciano abd H Pagels, Phys. Rep. 36c (1978) 137

V F Weisskopf, Ref. TH 2732-CERN

H Fritzch, Ref. TH 2483-CERN

J Kogut and L Susskind, Parton Models and Asymptotic Freedom
Phys. Rev. D Vol. 9, no. 12 (1974) 3391

6 M K Gailliard, Lapp TH-01 (1979)

CHAPTER 2

Experimental Aspects

2.1 Introduction

The CERN narrow-band (di-chromatic) beam used in this experiment is produced by allowing momentum selected pions and kaons to decay, producing neutrinos. Since in general neutrino energies can be deduced on an event by event basis only from the visible hadronic energy, narrow-band beams are unique in allowing the energy to be obtained from the kinematics of the parent hadron decay and the geometry of the experimental setup.

In this chapter the kinematics of the Narrow Band Beam (NBB), the experimental setup used to produce the beam, and the general features of the bubble chamber and external muon identifier are described.

2.2 Beam Kinematics[1,2]

The main source of neutrinos for high energy neutrino beams is from the 2 body decay of pions and kaons:

$$\pi^{\pm} \rightarrow \mu^{\pm} + \overset{(-)}{\nu}$$

$$k^{\pm} \rightarrow \mu^{\pm} + \overset{(-)}{\nu}$$

The decays are overwhelmingly two-body ($\sim$100% for pions and $\sim$64% for kaons) so that the energy spectrum is simply given by:

$$E_{\nu} = p_{lab} = \gamma \, p_{cm} (\cos \theta^{*} + 1) \qquad (1)$$

where $\gamma_{\pi,k} = E_{\pi,k}/M_{\pi,k}$ is the Lorentz factor for the decaying meson;

$p_{cm} = \frac{m_\pi}{2}\left(1 - \frac{m_\mu}{m_\pi}\right)^2$ is the neutrino momentum in the π,k centre of mass (cm) system , and θ^* is the cm decay angle. Since the parents are momentum selected ($\Delta p/p \sim 5\%$) a flat distribution in $\cos\theta^*$ leads to an essentially flat energy spectrum, so producing a substantial number of high energy events; with the energy bounded by:

$$0 < \frac{E_\nu}{E_{\pi,k}} < \frac{2p_{cm}}{m_{\pi,k}} = \begin{matrix} 0.43 & \text{for} & \pi \\ 0.95 & \text{for} & k \end{matrix}$$

Assuming a fixed parent momentum, with zero angular spread the transverse momentum of the neutrino relative to the beam direction is given by:

$$\begin{aligned} p_t &= p_{cm} \sin\theta^* \\ &= \theta\,\gamma\,p_{cm}(\cos\theta^* + 1) \end{aligned} \qquad (2)$$

where θ is the laboratory angle between a line joining the event vertex position to the parent decay point and a line joining the bubble chamber centre to the parent decay point (fig. 2.1), given by $\theta \simeq \frac{r}{(L + \frac{L_d}{2})}$

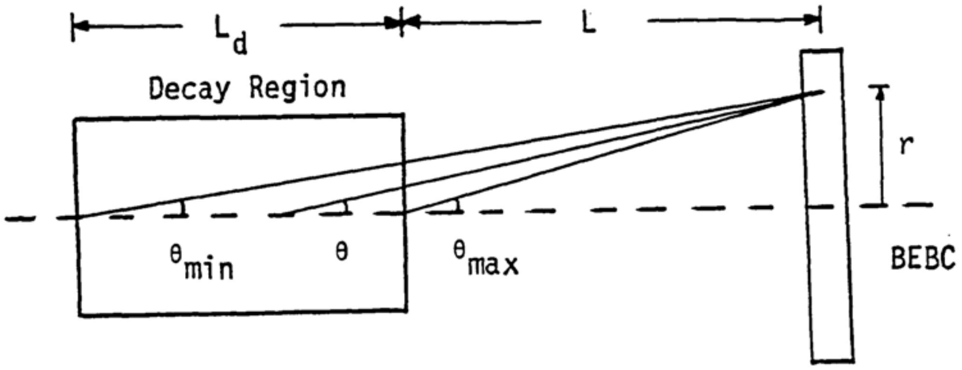

Fig 2.1

Using equation (2) to substitute into equation (1) gives:

$$E_{\nu}\,(R) \;=\; \frac{2\gamma p_{cm}}{(1 + \gamma^2\,\theta^2)} \;=\; \frac{E_{\nu_{max}}}{(\,1 + \gamma^2\,\theta^2)} \tag{3}$$

Since the parent decay point corresponding to each neutrino interaction is not known, at a given radius r the energy resolution is determined by the angles θ_{min} and θ_{max}:

$$\frac{\Delta E_{\nu}}{E_{\nu}} \approx \frac{\gamma^2(\theta^2_{max} - \theta^2_{min})}{1 + \gamma^2\,(\theta^2_{max} + \theta^2_{min})} \tag{4}$$

Best energy resolution is clearly attained for interactions near the chamber axis ($r \sim 0$) and for high energy neutrinos i.e. ν_k interactions. For this $\Delta E_{\nu}/E_{\nu}$ is ∿8% at $r = 0$, which is much smaller than to ∿20% energy resolution attainable from measuring the secondary hadrons.

The neutrino energy as a function of r predicted by equation(3) is shown by the ~~dotted~~ solid lines of Fig2.2. The neutrino data which has been corrected for neutral energy loss (chapter 3.2.2) is also shown. The effects of the finite beam divergence (∿0.2 mrad),and the parent momentum spread ($\Delta p/p \sim 5\%$) are indicated by the dotted lines which give the boundary within which 90% of all events at a given radius must lie.

The main source of background to the two body decay of neutrinos comes from the three body decays: $k \rightarrow \pi + \mu + \nu_{\mu}$ which contribute of order 2-3% at the higher energy, and from decays of low energy kaons before momentum selection, giving a wide-band background. The second source however is small due to the finite (15 mrad) angle between the beam in this region of the beamline and the detector. The net effect of these background sources is to fill the region between the peaks from two-body decays of π's and k's.

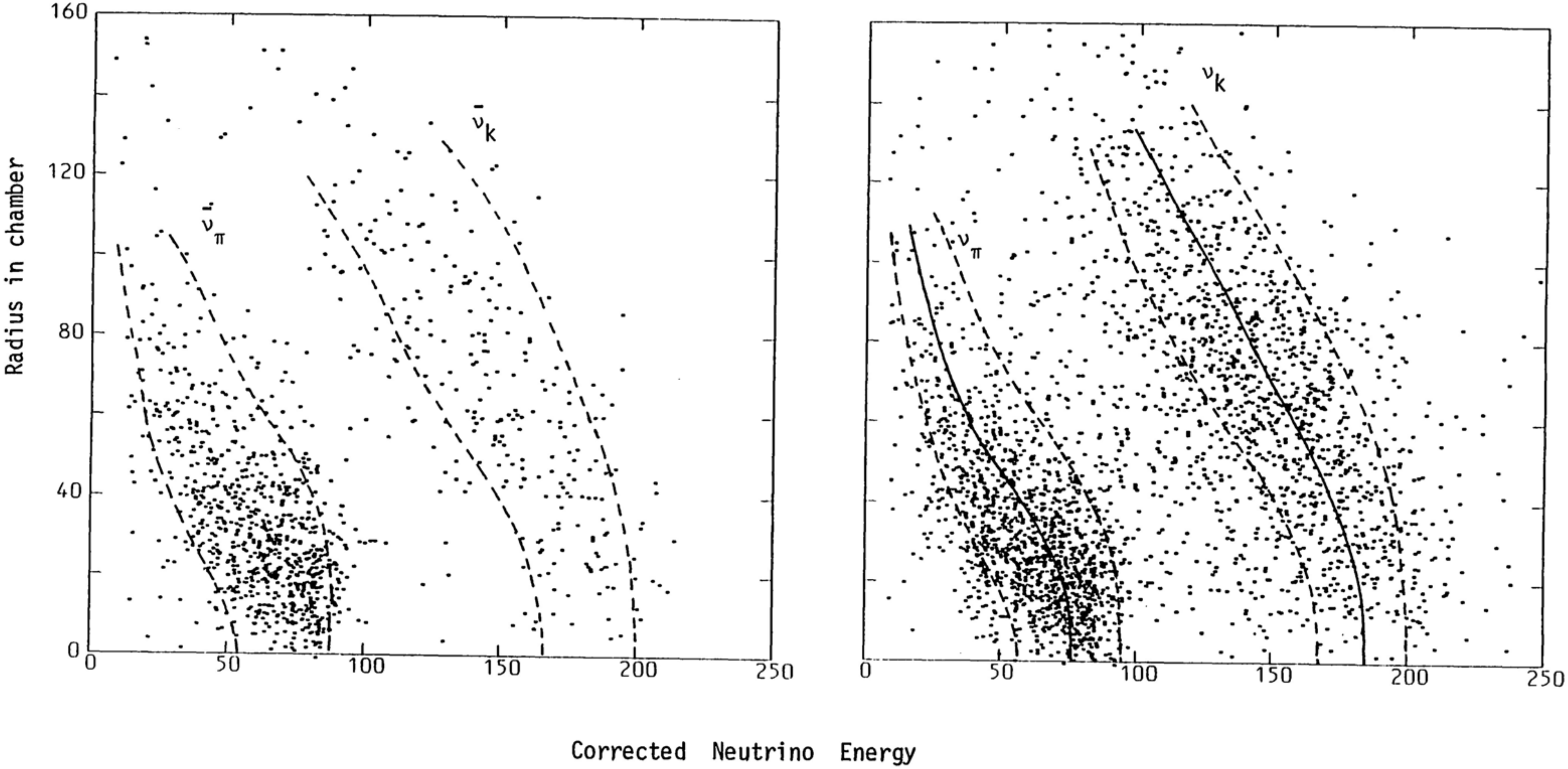

Fig 2.2 Radial distribution of Neutrino/Anti-Neutrino energy showing ν_π, ν_k separation. Dotted lines are the 90% boundary for events.

2.3.1 Neutrino Beam Line[3,4]

The use of the Narrow Band Beam (NBB) coupled with the fact that neutrino cross-sections are extremely small ($\sigma_{\nu} \sim 3\sigma_{\bar{\nu}} \sim 10^{-38}$ E(Gev) cm^{-2}) means that beams of high intensity, and large detector masses are required in order to achieve an adequate event rate. To obtain such beam intensity requires: optimisation of the target shape and material in order to achieve maximum proton usage and reduce reabsorption of the π's and k's within the target; good focussing of π's and k's; and long decay tunnels (since the pion decay path is 55 m/Gev). The requirement for long decay tunnels has to be compromised with the need for good energy resolution which requires small decay paths (equation 4). The experimental setup used to produce the CERN NBB is shown schematically in Fig 2.3.

Protons extracted from the SPS in a short spill of 2ms at 400 Gev/C transport momentum, are directed on to a three interaction length (90cm) beryllium target at an angle of $\sim$15mrad relative to the direction of the detector. The finite angle ensures that the wide band background of neutrinos due to hadrons decaying before momentum selection is minimised at the position of the detector.

The protons emerging from the target are dumped onto a copper block, and the rest of the secondary hadrons bent horizontally and focussed by quadruple magnets on a momentum slit which transmits hadrons with a momentum within a narrow range around 200 Gev/C ($\Delta p/p \sim 5\%$). The secondary hadrons are then further bent and focussed, and enter the vacuum decay tunnel as a beam which is parallel within ± 2 mrad.

Along the tunnel 3% of the π's and 32% of the k's decay producing neutrinos and muons. The muons are absorbed by shielding consisting of $\sim$ 185m of iron and $\sim$ 173m of earth and rock at the end of the decay tunnel.

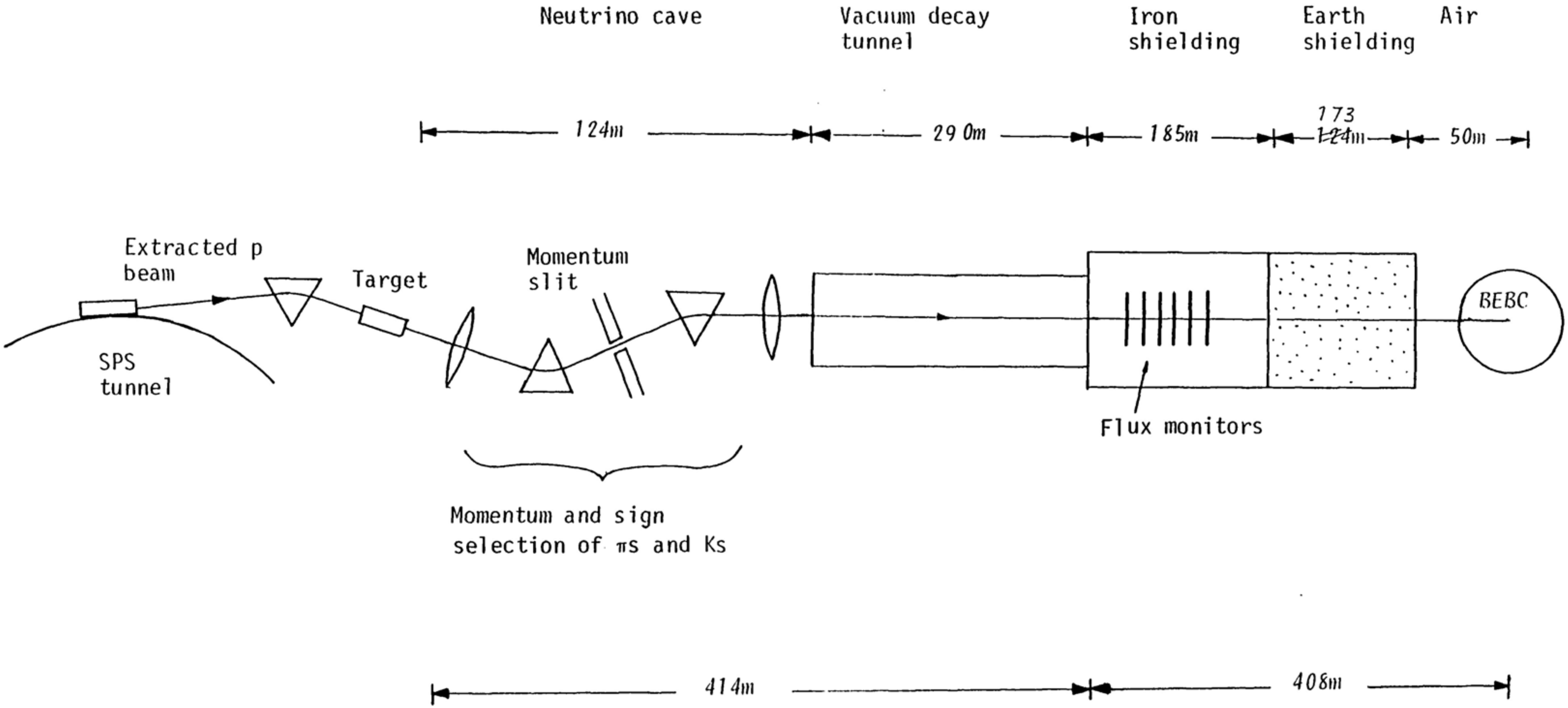

Fig 2.3 Schematic layout of the neutrino beam line, showing positions of bending/focussing elements, decay tunnel, μ shielding and BEBC.

2.3.2 Beam Monitoring

The quality of the beam is continuously checked from its production at the proton target to the iron shielding:

i) The intensity and profile of the proton beam is continuously monitored by detectors placed up and down stream of the target.

ii) A differential Cerenkov at the begining of the decay tunnel measures the hadron composition of the beam. (The relative proportions of π's and k's being required to determine the neutrino spectrum).

iii) Monitors at the begining and end of the decay tunnel measure the hadron beam profile, so providing information on the beam divergence.

iv) Silicon detectors placed in 6 gaps at various depths in the iron shielding continuously monitor the μ flux. Signals from the detectors represent the number of μ/cm^2 for each complete ejection of the SPS, and if the flux exceeds a preset level a flash trigger pulse is sent to BEBC. Information on the μ-flux intensity, radial symmetry, and central positioning is provided by online programs running in the neutrino beam monitoring (NFM) computer.

The fixed detectors in each gap are relatively calibrated by movable reference detectors which are themselves calibrated by counting the μ tracks in a nuclear emulsion mounted on top of the reference detector exposed to a few ejections of the SPS.

2.3.3 The Bubble Chamber

The Big European Bubble Chamber (BEBC) consists essentially of a stainless steel vessel, $\sim$ 4m high and $\sim$ 3.6m diameter, capable of withstanding working pressures of up to 10 bar (Fig 2.4). The chamber which is thermally insulated by an outer tank kept under vacuum of $\sim 10^{-5}$ -10^{-6} torr, contains two regions where the chamber body is relatively thin and represent the beam entry and exit windows, chapter 3, Fig 3.2.

The chamber vessel is subject to a magnetic field of $\sim$ 3.5 Tesla applied along the long axis of the chamber. The magnetic field is produced by two coils consisting of 3t of superconducting material embedded in 92t of copper reinforced by stainless steel ribbons and placed in a cryostat vessel housed in a common vacuum tank.

The upper hemispherical dome of the chamber has five optical units mounted at the corners of a regular polygon. Each of the units consists of three concentric windows, allowing thermal isolation from the chamber liquid; with four having a wide-angle lens, each with an annular flash tube in their centre. The fifth unit can be installed either with another camera or a periscope for monitoring during chamber filling and emptying. The cameras are mounted with the optical axis $\sim 13^0$ to the vertical allowing particle tracks to be reconstructed in space to better than 0.3mm, irrespective of direction. Each camera sees $\sim 22m^3$ of the same volume.

Incorporated in each camera is a data-box which projects binary and alphanumeric coded light signals from LED's onto the film when a bubble chamber picture is taken. The signals provide information about the roll, frame, and view numbers; and existing operating conditions. When BEBC is used in its double pulsing mode (as during part of WA 47 data taking), bits are set on the data box to distinguish hadron beam frames.

The inside of the chamber is covered with Scotchlite which reflects back the flash light providing a bright field illumination for the particle tracks. Fiducial marks consisting of the crosses printed on the Scotchlite in various planes perpendicular to the beam axis provide reference points for film measurement purposes.

2.3.4 The External Muon Identifier [5]

The External Muon Identifier (EMI) consists of two planes of multiwire proportinal chamber placed downstream of BEBC, (Fig 2.4). The inner plane which is 4m from the centre of BEBC, consists of 32 modules covering an area of 18m^2, and subtending a solid angle -43^0 to +35^0 horizontally, and -18^0 to +18^0 vertically. The outer plane which is 7.6m from the centre of BEBC, consists of two rows of 49 modules, covering an area of 150m^2, and subtending a solid angle -80^0 to +80^0 horizontally, and -20^0 to +20^0 vertically.

Each EMI module provides 3 hit co-ordinates from a set of cathode strips and two independent set of anode sense wires inclined at 30^0 to the cathode strips. The inner chamber provides a spatial resolution of 32mm. The spatial resolution of the outer planes is made to vary from 8mm in the central region, where the highest concentration of background hits occurs, to 32mm at large angles. This is achieved by varying the number of anode wires and cathode strips that are connected to a single electronic output channel.

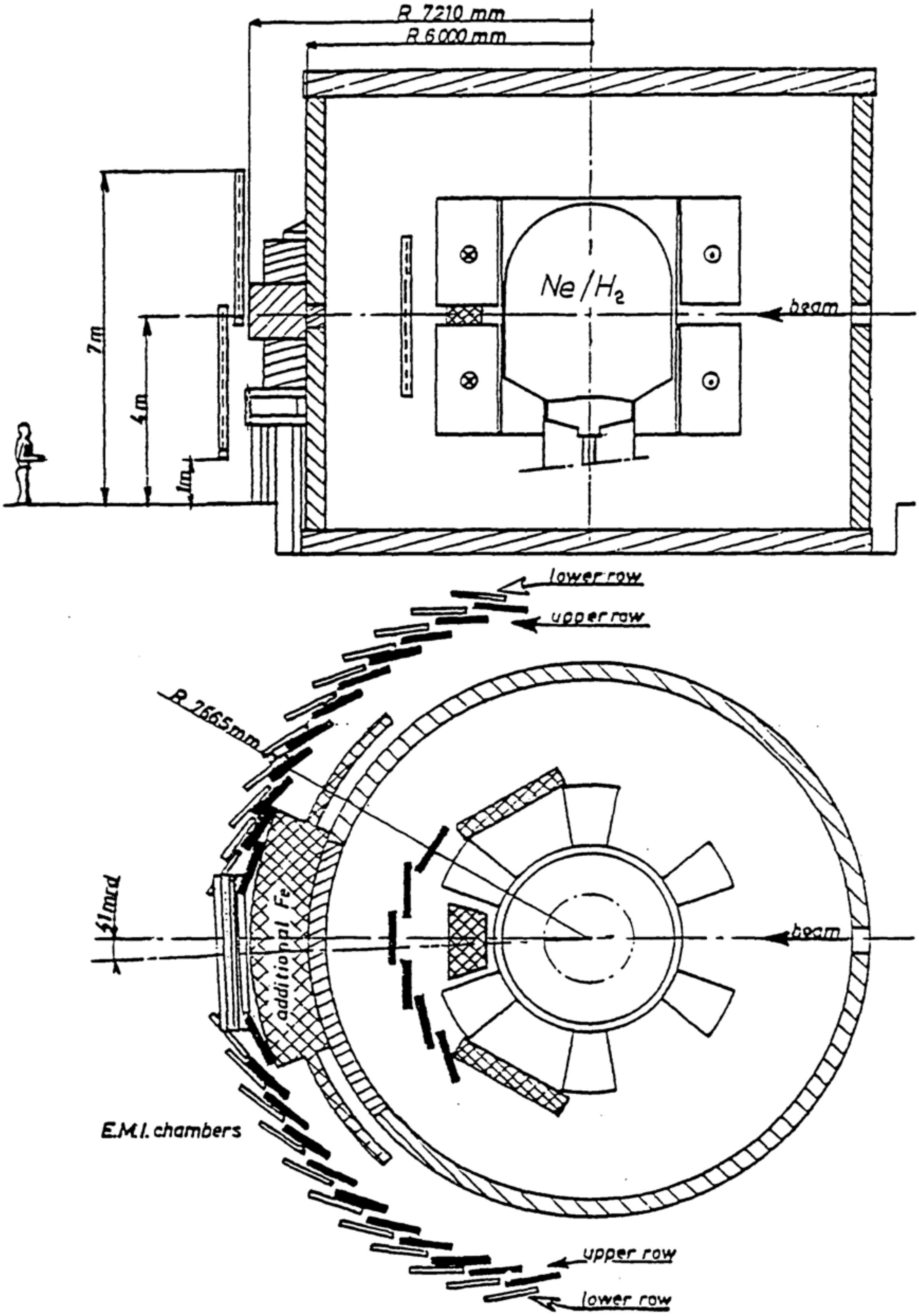

Fig 2.4 Schematic layout of inner and outer planes of EMI chambers behind BEBC

In order to reduce μ background produced by π decay, 50cm of lead absorber are placed in the forward cone region ~~down~~upstream of the inner planes. A further 2.1m of iron, (making ten hadron interaction lengths of absorber including the coil material), help to reduce the π punch through to the outer chamber to $< 1\%$ and the π decay to a few per thousand.

The NBB used in this experiment ensures that background hits in the EMI are very low (< 20 hits/pulse over the whole EMI sensitive surface), so that the efficiency for detection of muons depends mainly on the geometrical and electronic efficiencies. The geometrical efficiency is $\sim 98\%$, and rises to $\sim 100\%$ for $p_\mu > 5$ Gev/c, giving an overall μ detection efficiency of $\sim 98\%$ for $p_\mu > 5$.

References

1 K Kleinknecht, CERN School of Physics, CERN 78-01, p. 43

2 J Steinberger, CERN School of Physics, CERN 76-20, p. 57

3 BEBC Users Handbook

4 H Wachsmuth, CERN EP/PHYS 77-43

5 R Beuselinck et al, Nuclear Instruments and Methods, 154 (1978) 445-454

CHAPTER 3

Data Acquisition

3.1 Introduction

The production of a data summary tape (DST) from the raw events on film can be divided into the approximate stages:

i) Film scanning
ii) Event measuring (and on-line geometrical reconstruction)
iii) Off-line geometrical reconstruction and kinematical interpretation
iv) Checking for correct interpretation
v) Production of a DST

These stages, as applied to this experiment, are described in this chapter and summarised in the 'processing chain' flow chart of Fig 3.1. Also presented are the corrections applied to compensate for neutral energy losses.

3.1.1 Scanning [1,2]

The bubble chamber film was initially double scanned using two out of the four views available. The third view being used to check in more detail any events found, and a fourth view was kept as back-up in case of missing frames on the other three views.

All frames containing neutrino event candidates were noted. A neutrino event was defined by the criteria:

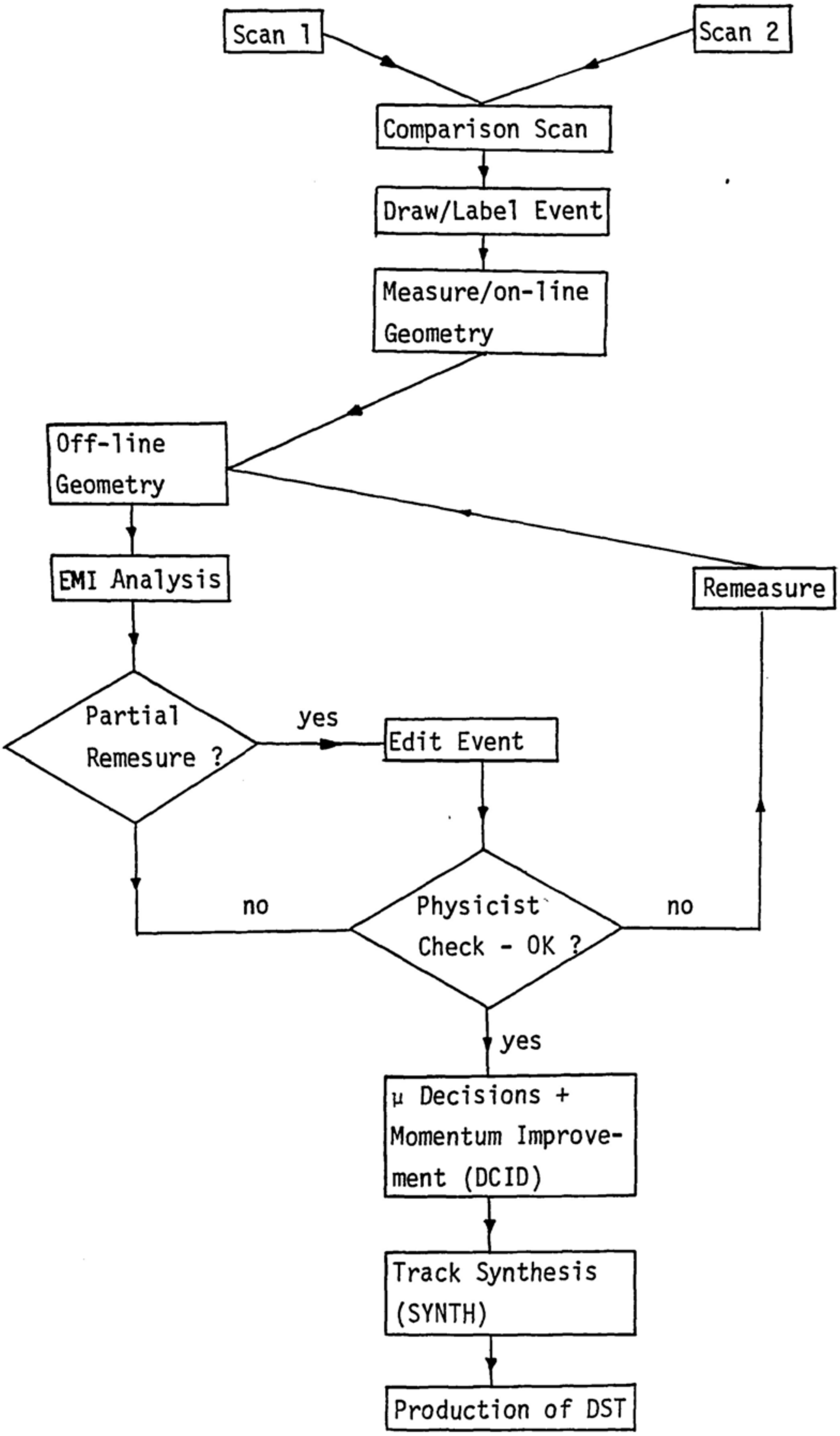

Fig 3.1 Data processing chain

i) It should have at least 2 charged prongs (1 prongs were not scanned for due to the low scanning efficiency for finding them). At least one of the tracks must be minimum ionising, straighter than a 1 Gev template, and forward relative to the beam direction. If such a track did not exist, an event was accepted as a neutrino interaction candidate if it had an electron pair on which one or both of the tracks were straighter than a ½ Gev template.

ii) The event originated in the chamber (ie was not due to charged tracks entering the chamber).

At this stage frame numbers of background events were also recorded. These events were defined as:

i) Type X: When a δ-ray on a charged track indicated an incoming track as the cause of an event otherwise thought to be due to a neutrino interaction.

ii) Type Y: When an event was thought to be due to an incoming charged track but there was no clear indication as to whether the track was leaving or entering the bubble chamber. To be of this type the event had to have a track which was straighter than a template for a 3 Gev track, and backwards from the ~~vertex~~ event vertex.

iii) Type Z: When all tracks failed the criterion for a neutrino event indicated above. (These are neutron stars which were measured if there was also a neutrino event on the same frame).

iv) Type W: When three or more charged tracks came from within the distance in the x and y direction (Fig 3.2) given by the width of a Scotchlite panel (34cm). To be a type W (Wallon) at least one of the tracks should scatter or kink without spiralling. In WA47 neutrino events on frames containing Wallons were measured if the neutrino event was clearly unassociated; the fastest Wallon track also being measured for use by off-line geometry for event association checks.

Using the results of the two independent scans an event check list consisting of the frame numbers of all possible events and ambiguous back ground events observed in either scan was prepared.

Each frame was then checked, with the aid of a physicist where necessary. Events which were relatively clear (no complicated secondary scatters, or electromagnetic showers), and lay within the fiducial region, were drawn and labelled ready for measuring on a X18 magnification table. The labelling scheme is given in section 3.1.2. More complicated events were left to be drawn at the measuring stage on a X50 magnification table.

The fiducial volume region used consisted of $\sim 17m^3$ of the chamber liquid. The region was defined in the X - Y plane by a semi-circle of radius 180cm in the upstream direction, and a semi-circle of the same radius, but with its centre displaced 50cm upstream, in the downstream direction (Fig 3.2). In the z direction the region was defined by a cut at $z = \pm$ 100cm.

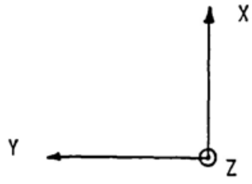

Co-ordinate System

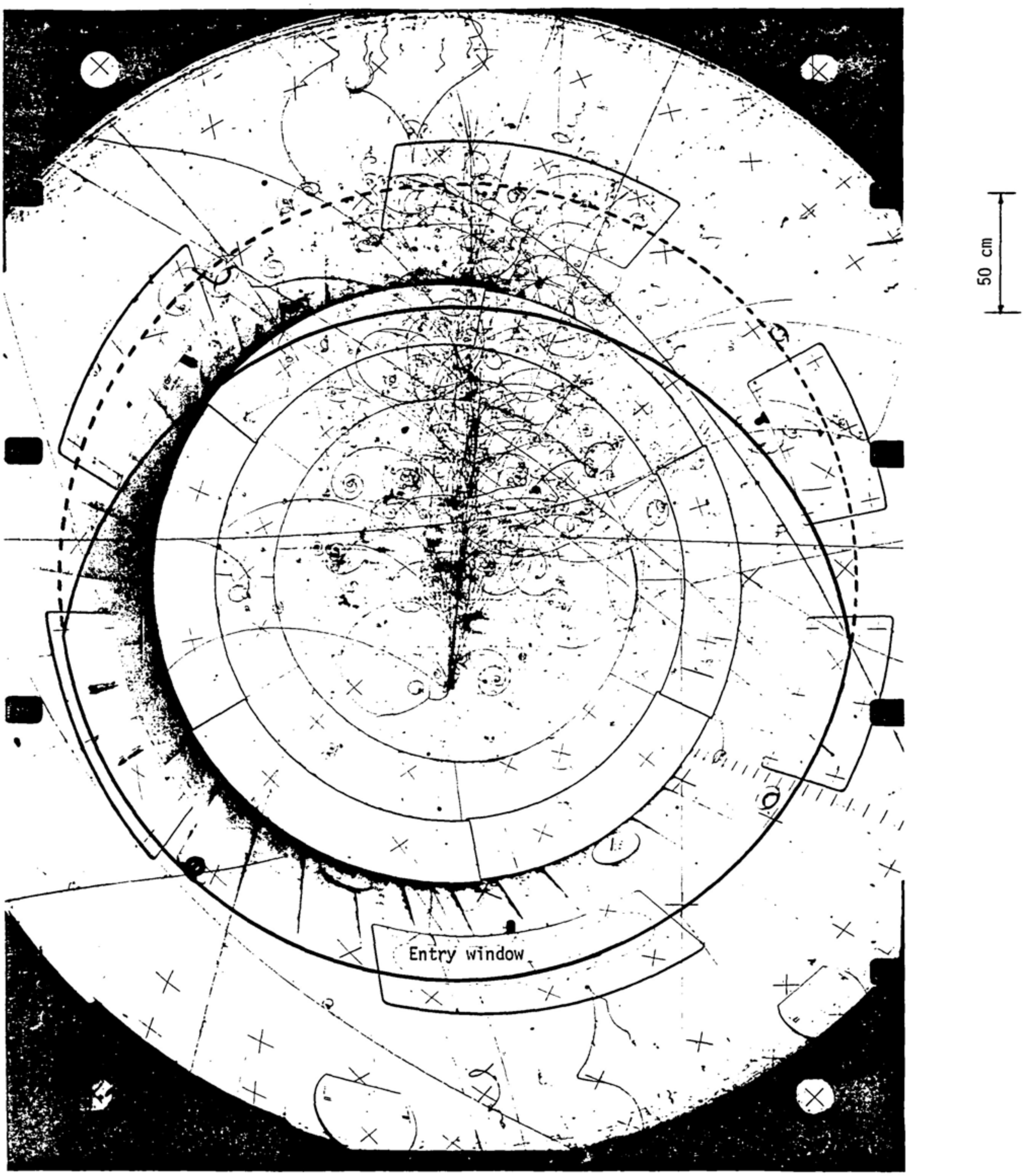

Fig 3.2 Fiducial region in the x-y plane used for accepting events.

Scanning Efficiency

The probability of finding an event as a result of the two independent scans is given by:

$$p = \frac{N_{12}\,(N_1 + N_2 - N_{12})}{N_1\,N_2}$$

Where N = All events found

N_{12} = Events found on both scans (= $p_1\ p_2\ N$

p_1, p_2 being the probabilities of finding the events in scans one and two respectively)

N_1 = Events found on the first scan (= p_1 N)

N_2 = Events found on the second scan (= p_2 N)

Where all events are assumed to be detectable with equal efficiency. The above formula gives a scanning efficiency for finding a neutrino event on film of ∿ 99%, in WA47 which is comparable to the ∿ 98% efficiency which was found in WA19.

3.1.2 The Measuring System[2,3]

The complexity of high energy neutrino events in a bubble chamber filled with heavy Ne/H_2 mixture means that a check on the precision of the event measurement has to be made during the measuring stage in order to avoid repeated remeasures. The system used at Imperial College is described briefly in this section.

An essential simplifying feature that has been employed is the use of a comprehensive track/vertex labelling scheme for the event drawing made at the third scan stage. These track labels serve essentially three purposes:

i) Helps the measurer in conversation with the measuring control program, and sorting out complicated events.

ii) The track-end type labels are useful for the geometry program for matching of tracks from secondary scatters. (Individual tracks from primary vertices are measured view by view, but those from secondary scatters are all measured on one view at a time so that the geometry program then has to match the corresponding track measured on each view). Also the track labels are used to reduce the number of mass hypotheses attempted (eg no muon hypothesis attempted on an interacting track); and the vertex labels used for association of γ's and V^0's to vertices.

iii) Since the track end-type labels are produced on the final DST, they can be useful for eventual physics analysis.

The definitions of the various vertices used in the event labelling are:

i) Primary vertex: All vertices which can possibly be neutrino events. Also included in this category are neutron stars from primary neutrino events; the linking or exclusion being done at a later stage.

ii) Secondary vertices: All interaction points, kink points, stopping points and decays.

iii) V^0 vertices: charged decays of V^0's.

iv) γ vertices: vertices of e^+, e^-, and e^+e^- pairs.

The track and end-type labels used are:

Leaving(L) : Non-interacting tracks which leave the bubble chamber. All such tracks are possible muon candidates.

Stopping (S) : For these all mass hypotheses are tried and the fit rejected if there is a momentum-range incompatibility, ie for π^- disappearance in flight.

Protons (P) : For short straight tracks which are obviously protons from ionization.

Decay (D) : For decays of $\mu^\pm$, π^+ or k^+.

Capture (C) : For visible recoil protons at the end of an apparently stopping track. Only the hypothesis π^- is tried for these.

Electron (E) : These are either called definite electrons for which only the electron mass hypothesis is tried (eg as at gamma vertices); and possible electrons (eg from primary vertices) for which other mass hypotheses are also attempted.

Interacting (I) : For these the μ hypothesis is excluded.

Kink (K) : One prong interactions where the outgoing track scatters through a small angle.

The measuring system consisted of a X18 measuring machine used for relatively simple events, and a X50 magnification machine for more complicated events. The measuring machines are connected via a PDP8L mini-computer to a PDP10 computer in which resides one measurement control program for each of the machines, and a common on-line geometry program.

The operator first enters the roll, frame numbers and the event topology, followed by a measurement of the fiducial marks. The control program then asks for each of the tracks to be measured on three views in turn, and for the track and vertex labels to be supplied. At the completion of the measurement of the current item the control program calls the on-line geometry program. This then reconstructs the vertices and tracks using helix fits and attempts kinematic fits at V^o and gamma vertices. If the measurement is diagnosed bad (large chi-squared or residuals), it is reported to the measurer by the control program and a remeasure requested.

Once all events have been acceptably measured, they are processed by Hydra off-line geometry. This program attempts various mass hypotheses (depending on the measurers labelling) and performs kinematical reconstruction of measured V^o's and gammas and attempts to associate them to upstream primary and secondary vertices. The output from the geometry program together with the raw EMI data, are then used as input for the EMI analysis program. This program follows each track leaving the bubble chamber, through the fringe field and iron shielding down to the EMI planes assuming it to be a muon. If a hit is found in the EMI planes a chi-square of association of the predicted hit is calculated and the leaving track labelled or not as a muon candidate on the basis of this chi-square.

3.1.3 Measurement Checking[4]

The output from the EMI analysis program, consisting of a summary of the off-line geometrical and kinematical reconstruction, and the EMI track extrapolation results, are then used by physicists in conjunction with the original hand drawing, and graphical drawings of the measured event, to check the event measurement quality at the scan table.

The basic checks made consist of ensuring that:

i) All primary charged tracks have been measured with small measurement errors (generally $\Delta p/p < 30\%$ for hadrons and $\Delta p/p < 50\%$ for electrons), and that tracks carry the correct end-type labels, ie that the right mass hypotheses exsist.

ii) A minimum momentum estimate has been obtained from measurement of secondary tracks in cases where the primary track was too short to give an accurate momentum estimate.

iii) As much as possible of the primary neutral energy has been measured (an event being defined as completely measured on the final DST if > 95% of the visible energy had been measured), and in particular that all V^0's have been measured. A critical check is also made at this stage to reduce the number of V^0's ambiguous with gammas.

iv) EMI associations have been made for each track leaving the bubble chamber and the best candidate chosen.

On the basis of these checks, events are remeasured and the procedure repeated until satisfactory measurement for each event is obtained. Generally, because of the checks on the measurements made by the on-line geometry, remeasurement consists of measuring only part of the events, eg γ's or secondary scatters.

3.1.4 Production of the DST[5]

The final event measurements from each of the collaborating laboratories were then collected at CERN and processed by a series of analysis programs. The basic functions of these programs are as follows:

To make final decisions on muon candidates; and in cases where the muon momentum is badly determined ($\Delta p > 10$ Gev/c), an attempt is made to improve the error by comparing the position of the extrapolated points to the EMI hit positions. (Program DCID).

To select the best origins for the associations of neutron stars, gammas and V^o's, and synthesise neutral track connections for neutron stars and V^o's. (Program SYNTH). In the case of neutron stars the best vertex is selected as the one which gives the minimum angle between the line of flight obtained from the vertex under test and the neutron stars' vertex; and the sum of the momenta of the outgoing tracks from the neutron star vertex, Σp_i. If the transverse momentum of the Σp_i relative to the line of flight is greater than 5 Gev/c the vertex is rejected altogether. In the case of V^o's and gammas the best origins are determined from the results of 3c fits to each vertex.

Finally the program DSTOUT was used to make the mass selections and create a DST which was circulated amongst the laboratories.

3.2.1 Basic features of the Data

The kinematic region exploited by the data is shown in Fig 3.3 for the neutrino and anti-neutrino data using some of the variables which will be referred to most often for physics analysis. All variables have been corrected for energy losses as discussed in chapter 2.2.2.

The final data samples obtained are given in the table below.

Events	Neutrino	Anti-neutrino
Total (Within Fiducial Region)	5739	2457
Neutral Current (NC)	2545	1232
Charged Current (CC) (p_μ > 5 Gev/c)	3036	1167
Events used for Analysis (CC)	2887	1108

The charged current events used for eventual analysis are defined as those for which $p_\mu > 5$ Gev/c, and for which all variables (x, w^2 etc) are within physical limits. Also events containing tracks with $\Delta p/p >$ 30% and carrying greater than 30% of the event energy were rejected.

A guide to the quality of the measurements is provided by the distribution of $\Delta p/p$ of the tracks on the final DST, shown in Fig 3.4. The large track length of the muons (and momentum improvement of badly measured ones) gives a good estimate of its momentum with: $\langle\Delta p/p\rangle \sim 5\%$ for muons of momentum greater than 5 Gev/c. The charged hadron momentum is also relatively well measured with $\langle\Delta p/p\rangle \sim 6\%$. However gammas generally have a poor measurement of their momentum. This is due to bremsstrahlung and subsequent spiralling of electrons from converted

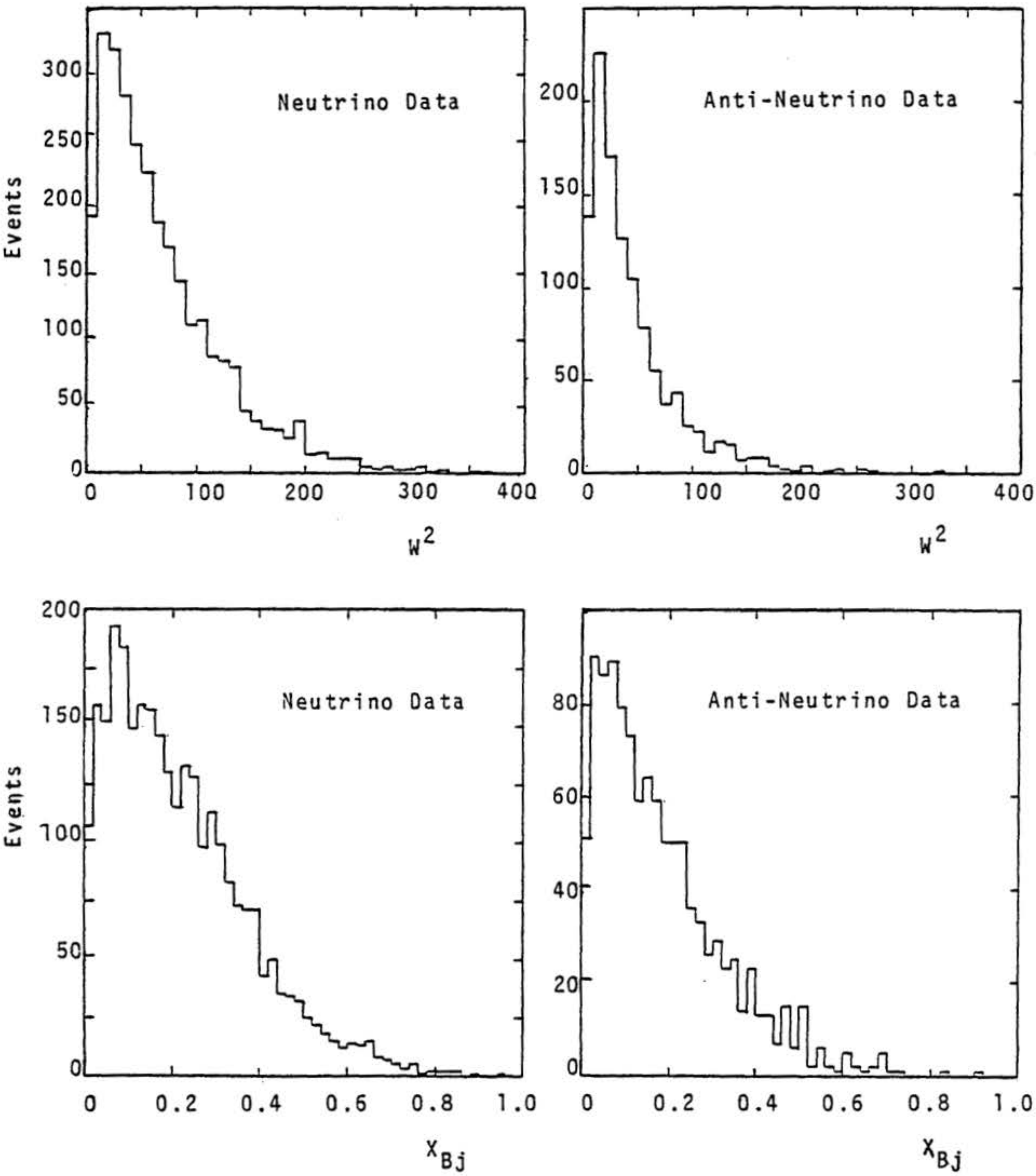

Fig 3.3 Distribution of W^2 and x_{Bj} showing the kinematic regions accessed by the data.

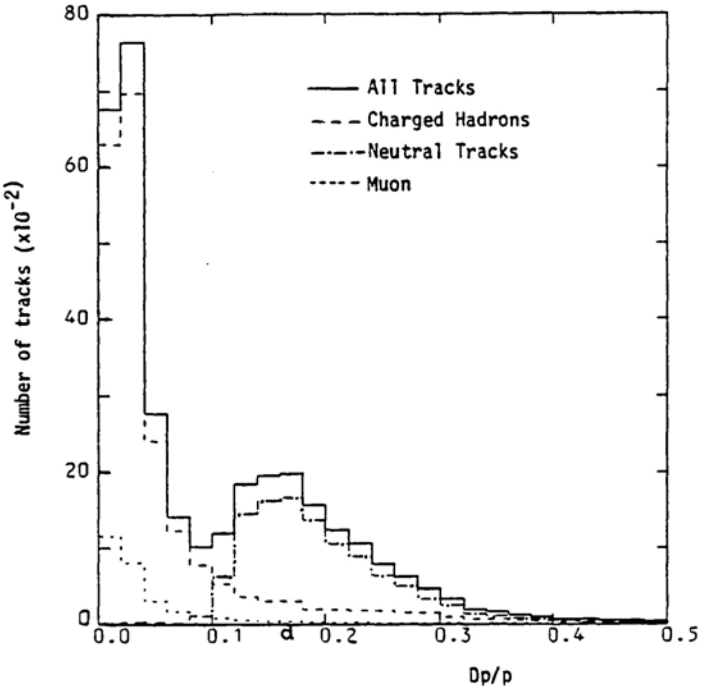

Fig 3.4 Distribution of measurement errors on various track types.

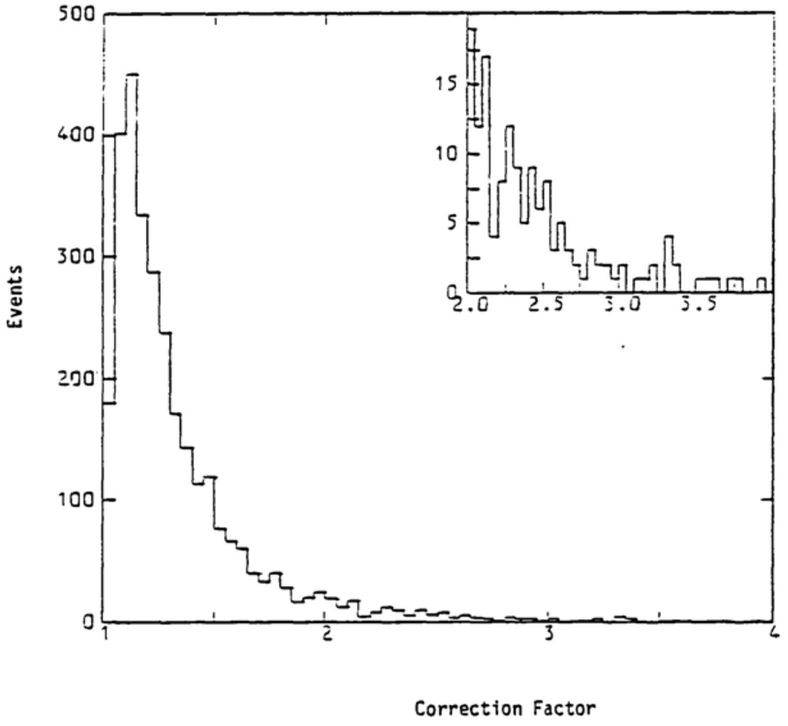

Fig 3.5 Distribution of the event by event energy correction.

(insert shows tail of distribution)

gammas providing a relatively short length of electron track for momentum estimates.

3.2.2 Energy Corrections

The estimation of the hadronic energies by measurement of the tracks observed in the bubble chamber represent only a lower limit on the true hadronic energy. This is because of neutral energy losses through unconverted gammas and undetected neutron stars, and due to incompletely measured complicated electromagnetic showers and secondary scatters. In order to account for such energy losses corrections have been made based on two methods: a) an event by event energy correction, and b) a global energy correction for all events; and attempts made in order to determine which method is more suitable.

a) Event by Event Correction

This correction factor (c_h) is obtained from the formula |6|:

$$c_h = 1 + \frac{\Sigma \mid \vec{p}_{t_{had}} + \vec{p}_{t_{\mu}} \mid}{\Sigma \mid \vec{p}_{t_{had}} \mid}$$

Where the transverse momenta are measured relative to the neutrino direction, and the sum runs over all observed hadrons with $\Delta p/p < 0.3$. The distribution of this correction factor is shown for the entire data sample in Fig 3.5. The mean values for the distributions of the various data samples are:

	Neutrino	Anti-neutrino
WA19	1.39	1.40
WA47	1.30	1.31

b) Global Correction[7]

This method of energy correction, relies on balance of the transverse momentum of the muon relative to the neutrino direction, with the transverse momentum of the sum of observed hadrons multiplied by the correction factor to be determined:

$$p_\mu \sin \theta_\mu = \frac{p_h}{\varepsilon} \sin \theta_h$$

Where ε is the inverse of the energy correction factor the other quantities appearing in the equation are shown in Fig 3.6.

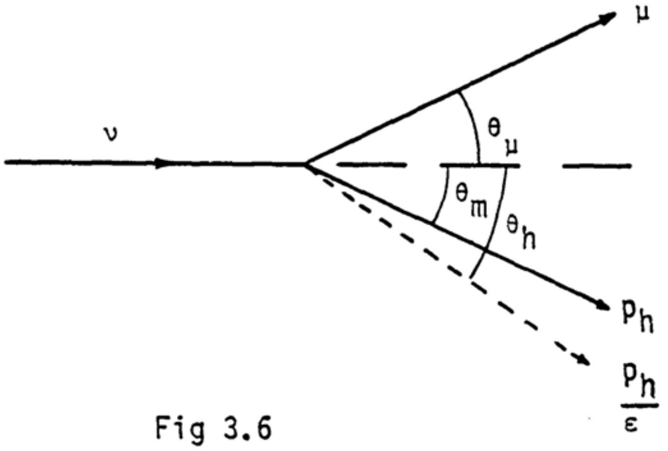

Fig 3.6

Adjustment of the value of ε gives $\Delta\theta = (\theta_m - \theta_h)$ as a function of ε. Here θ_m is the measured value of θ, and θ_h the value of θ required to balance the transverse momentum of the muon with that of the hadrons for the given value of ε. Then a least-squares fit gives the value of ε corresponding to $\Delta\theta = 0$. The procedure is repeated for various bins of the observed hadronic energy, (using only tracks for which $\Delta p/p < 0.3$ since this cut is applied in the physics analysis presented later).

The results on the value of $\langle\varepsilon\rangle$ as a function of the hadronic energy are shown in the plots of Fig 3.7. The method becomes less reliable at

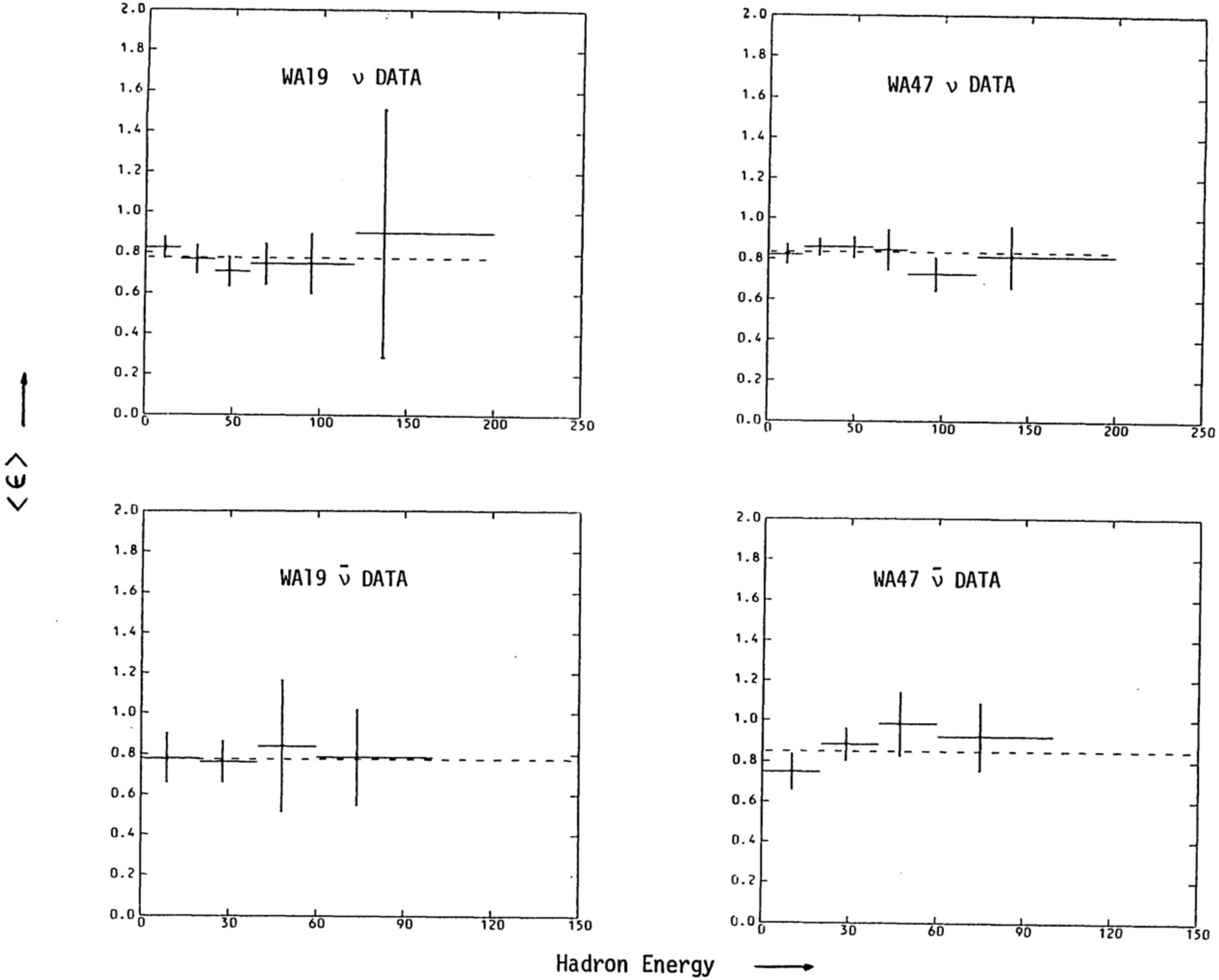

Fig 3.7 Energy dependence of the global energy correction factor.

high energies due to a relatively small adjustment in the value of θ_h being required for a given change in ε (so that $\Delta\theta$ shows a weaker dependence on ε). The value of $\langle\varepsilon\rangle$ is seen to be independent of energy, so the value of the correction factor; $c = 1/\langle\varepsilon\rangle$ obtained from the weighted average of $\langle\varepsilon\rangle$ are given here:

	Neutrino	Anti-neutrino
WA19	1.29 ± 0.06	1.29 ± 0.12
WA47	1.19 ± 0.03	1.17 ± 0.07

The results indicate that the hadronic energy has been better measured by ∿ 10%, in the second part (WA47), of the experiment than in the first part. The same trend is shown by the average values of event by event corrections, and is reflected in the visible quantities (no $\Delta p/p$ cut): $\langle E_{vis}\rangle = 100.6$ Gev for WA47 and $\langle E_{vis}\rangle = 94.5$ Gev for WA19. The difference is due to a substantial improvement, mainly in neutral energy measurements in WA47:

Mean Energy (Gev)	WA19	WA47
$\Delta p/p < 0.3$		
Charged Tracks	26.1	27.7
Neutral Tracks	6.6	10.5

Test of Correction Factors

In order to determine how well the correction factors obtained by the two methods correct for energy losses, the ratio

$$R = \frac{E_\nu^{cor}}{E_{\nu_k}(r)}$$

has been used where E_ν^{cor} is the energy determined from the hadron energy corrected by the appropriate method and the muon energy, and $E_\nu(r)$ is the energy obtained from the decay kinematics (chapter 2.2.1) treating all neutrino interactions as if they are from ν_k. The plot of Fig 3.8a shows the distribution of R. The event by event correction gives a slightly larger peak at R = 1 and a few less events in the region between the pion and kaon peaks so indicating a better ν_π, ν_k separation than by the constant correction. However the difference is only small, and on average both methods correct the data in a similar way. The ν_π, ν_k seperation achieved by both the methods is reasonably good. (For the event by event correction this is shown in chapter 2 Fig 2.2 for neutrino and anti-neutrino interactions).

Thus the distributions of measurable quantities such as the neutrino energy (Fig 3.8b) are very similar when corrected by the two methods, and the two correction methods cannot be distinguished. However since the global energy correction produces an arbitrary upper cut-off to the z $(= E_{h_i}/(\text{corr.} \times \Sigma E_{h_i}))$ distribution, the energy correction determined on an event by event basis has been used for analysis purposes. It has been checked that the physics conclusions drawn do not change if the global method is used.

References

1 K W J Barnham, Imperial College Physics Note, IC/HENP/PN/52

2 K W J Barnham, Imperial College Physics Note, IC/HENP/PN/56

3 S Banerjee, Imperial College Physics Note, IC/HENP/PN/54

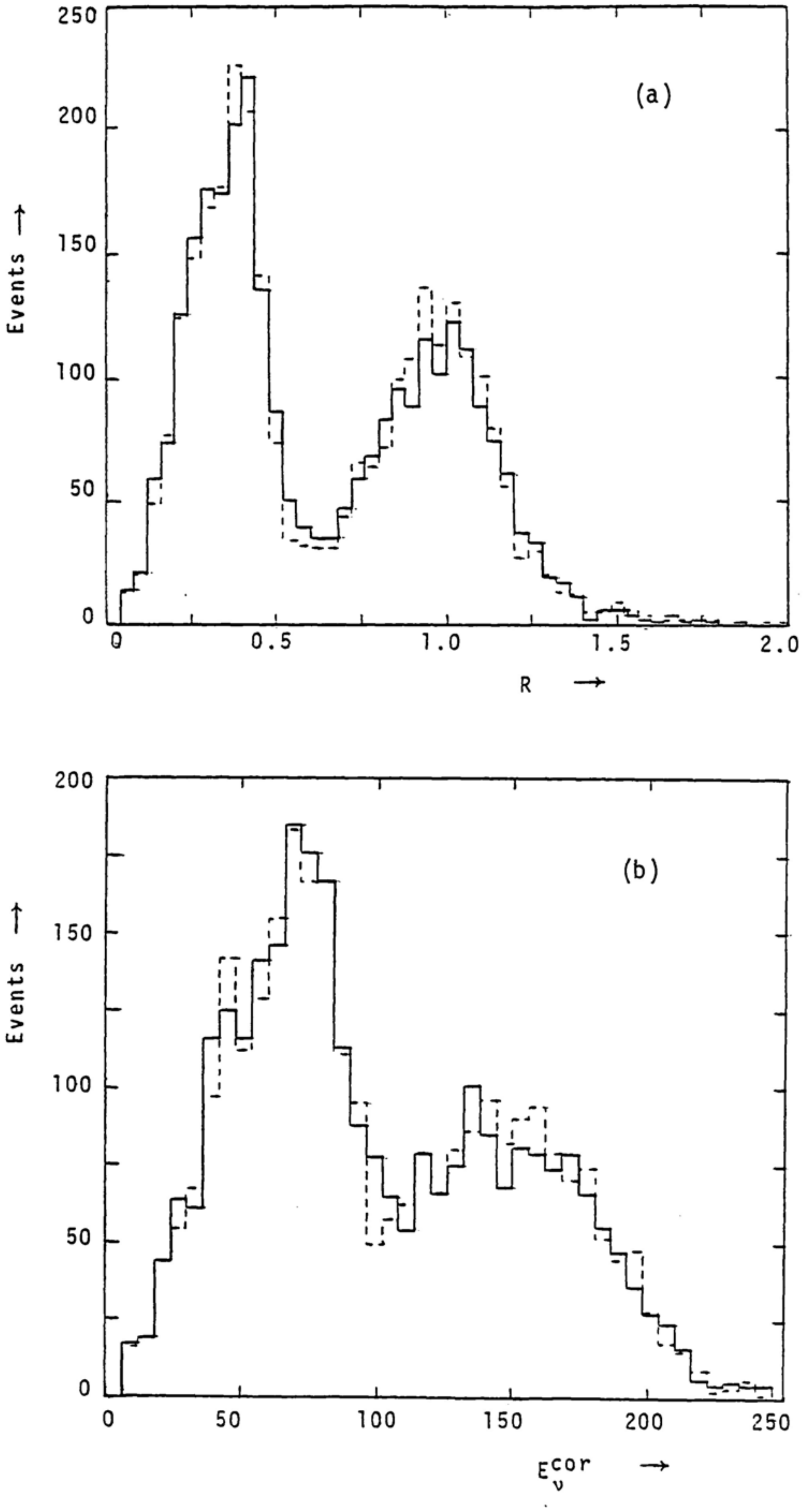

Fig 3.8 a) Comparison of the energy correction methods and, b) distribution of the corrected neutrino energy. In both cases the dotted line represents an event by event, and the solid line a global correction.

F Bruyant et al, HYDRA applications library Long Write-up GEOPAM, CERN

4 D C Cundy et al, CERN/EP/NPC/76-3

5 L Pape, Minutes of the ABCDLOS Collaboration Meeting, March 1979

6 Method due to Heilmann, University of Bonn Internal Report

7 H Deden et al, Nucl. Phys. B149 (1979) 1-12

CHAPTER 4

Inclusive study of the Hadronic System

4.1 Introduction

The phenomenological consequences for the hadronic system of leptonic interaction, arising from the effects of the 1st order QCD diagrams (chapter 1.4) involve quantitative and qualitative predictions in terms of:

i) Asymmetries in the azimuthal distributions of hadrons.

ii) Increase in the transverse component of the momentum of the hadrons with w^2 (or q^2).

In this chapter such predictions are tested and attempts made to determine the primordial transverse momentum of valence quarks, and to estimate the value of the strong interaction coupling α_s (q^2). A comparison is also made with the structure of hadrons resulting from $e^+ e^-$ annihilations.

4.2 Azimuthal Correlations

The cross-section for the 1st order QCD processes (chapter 1 Fig 1.4) is given by |2|:

$$\frac{d\sigma}{dx\ dy\ dz\ d\phi} = A + B \cos\phi + c \cos 2\phi \qquad (1)$$

where A represents the zeroth order 'naive' quark parton model term in which all non-scaling effects due to quark masses and transverse momenta are neglected and B and C are terms depending on q and g fragmentation functions. The angle ϕ is the angle between the projection of the outgoing μ and the hadron in the plane orthogonal to the measured current direction (Fig 4.1).

Predictions about the sign and magnitude of the terms B and C will thus determine the behaviour of $\langle\cos\phi\rangle$ and $\langle\cos 2\phi\rangle$ as functions of the kinematic variables y, z, etc. In order to make a comparison between the data and these predictions, it is essential to understand any systematic effects that may be induced. Such effects may be due to the lack of knowledge of the neutrino energy causing the current direction, relative to which these predictions are made, to be badly determined.

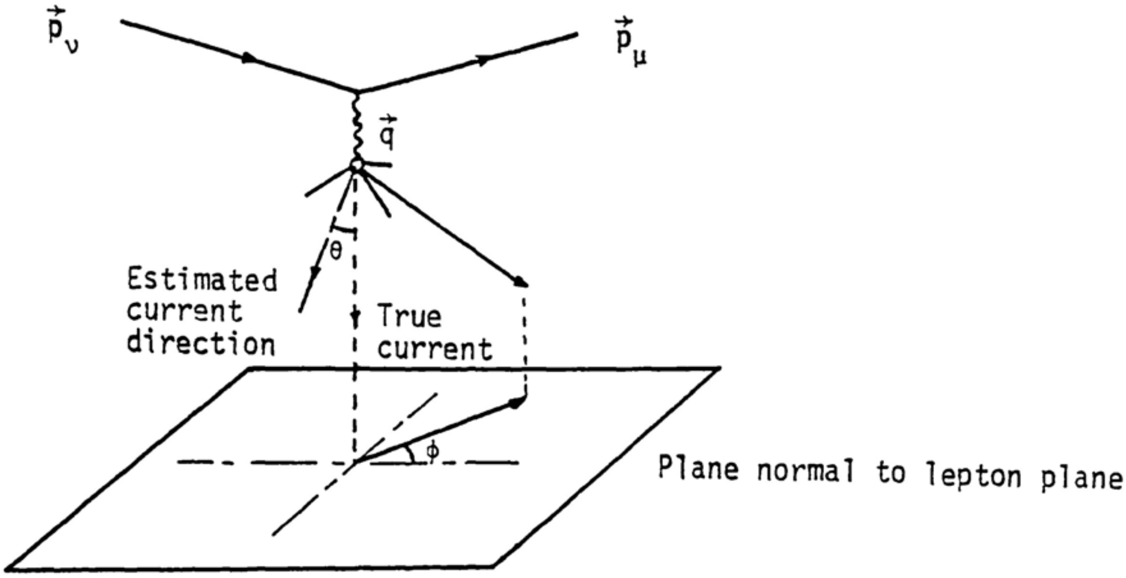

Fig 4.1

4.2.1 Determination of the Current Direction

An estimation of the current direction can be obtained in the following ways:

i) $\vec{q} = \vec{p}_\nu^{\,cor} - \vec{p}_\mu$	Current axis using corrected neutrino energy.
ii) $\vec{q} = \sum_i \vec{p}_{hi}$	Hadronic axis using observed hadron momenta.
iii) $\vec{q} = \vec{p}_\nu^{\,rad} - \vec{p}_\mu$	Using neutrino energy determined from radial position in the bubble chamber

In (i) the uncertainties arise due to an average of ∿20% of the hadronic energy being unmeasured through missing neutrals. This then leads to an uncertainty in $|\vec{p}_\nu^{\,cor}|$, which is determined from the corrected hadronic energy, so causing a systematic shift in the current direction as illustrated by Fig 4.2. Since however the lepton plane is well defined due to accurate knowledge of the neutrino direction and good muon momentum measurements (see chapter 3.2.1), the current axis is well known relative to this plane. It is only within the lepton plane ($\phi = 0$ line in Fig 4.1) that the current axis direction is not well defined, and results based on Monte Carlo data |appendix 1| suggests an uncertainty in the angle θ given by: $\langle\Delta\theta\rangle \sim 1.5^\circ$. The hadronic axis (ii), can clearly be displaced in any direction relative to the true current direction due to smearing caused by missing neutrals. The Monte Carlo suggests that this axis gives an uncertainty in the angle θ given by: $\langle\Delta\theta\rangle \sim 1.9^\circ$ which is similar to the current

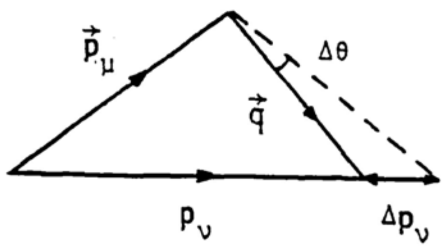

Fig 4.2

axis. In case (iii) the problem is the same as in (i) except at large E_ν, where $\Delta E_\nu/E_\nu$ becomes small (∿ 8% see chapter 2.2). These are neutrinos from kaon decay.

The systematic effects on sine and cosine functions of ϕ, caused by uncertainties $\Delta\theta$ in the current direction can be understood from Fig 4.3. Effects in cos 2ϕ and sin 2ϕ will be of 2nd order

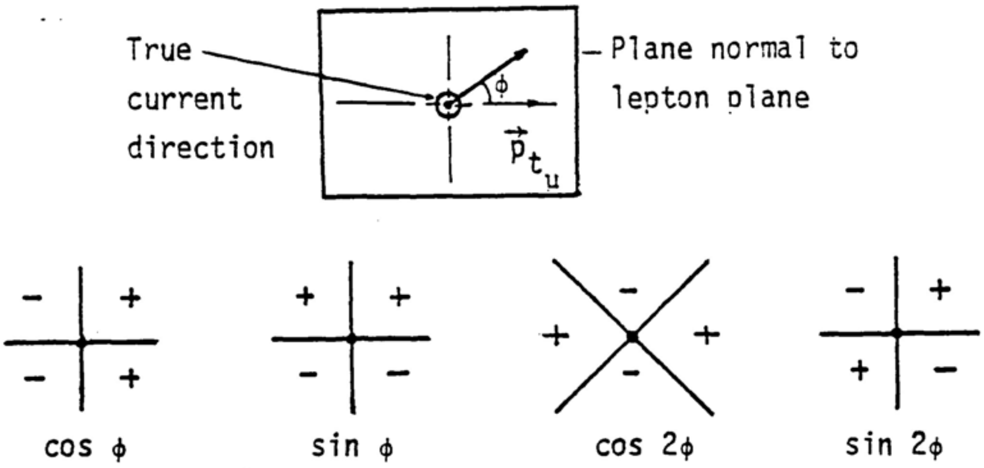

Fig 4.3

compared to those in cos ϕ and sin ϕ. The current axis will tend to induce a systematic effect in cos ϕ only, since it is well confined to the lepton plane; whilst the hadronic axis will potentially induce an effect in both cos ϕ and sin ϕ since it can be displaced in any direction relative to the true current direction.

An approximate estimate of the systematics involved can be obtained from the results based on the Monte Carlo data, given in table 4.1. This suggests that the hadronic axis induces very small systematic effects ($< 2\%$) in the mean values of the sine and cosine functions of ϕ. The current axis gives similar effects in all functions except cos ϕ where systematic effects $\sim 10\%$ are induced.[†] These results can be understood from the fact that the hadronic axis tends to average out the missing neutrals whereas the current axis does not. The hadronic axis will thus be used for analysis of the experimental data. (The axis defined in case (iii) above reduces the data sample, since only ν_k events can be used, without significantly affecting the results presented below).

4.2.2 Definition of Current Jet

The hadrons from fragmentation of the struck quark are assigned to be those produced forward in the cm system of the current and target nucleon. Such a criterion is supported by the change of the cm rapidity Y_{cm} in the region $Y_{cm} = o$, provided w is sufficiently large, as shown in Fig 4.4a for incident neutrino data, and Fig 4.4b for antineutrino data, in qualitative agreement with the quark parton model. The distinction between forward and backward jet is not clear at low w (< 6).

[†] The sign of $\langle \cos \phi \rangle$ suggests that the neutrino energy is underestimated on average.

$< Q^2 >$	$<\cos\phi>$	$<\sin\phi>$	$<\cos 2\phi>$	$<\sin 2\phi>$
2.9	1.15 ± 1.29	- 1.7 ± 1.3	- 0.9 ± 1.3	- 1.1 ± 1.0
18.7	- 1.21 ± 0.71	- 1.0 ± 0.6	0.3 ± 0.7	- 0.1 ± 0.7
73.5	- 1.35 ± 1.49	- 0.7 ± 1.2	1.4 ± 1.5	+ 1.8 ± 1.5

Hadronic Axis

$< Q^2 >$	$<\cos\phi>$	$<\sin\phi>$	$<\cos 2\phi>$	$<\sin 2\phi>$
2.9	9.9 ± 1.3	- 0.7 ± 1.3	- 0.8 ± 1.3	0.6 ± 1.3
18.7	7.3 ± 0.7	- 1.3 ± 0.7	0.4 ± 0.7	- 0.2 ± 0.7
73.5	8.2 ± 1.5	- 2.3 ± 1.5	3.1 ± 1.5	2.3 ± 1.5

Current Axis

Table 4.1 Monte Carlo results on systematic effects in ϕ, measured relative to the hadronic axis, and the current axis. (Values $\times 10^{-2}$).

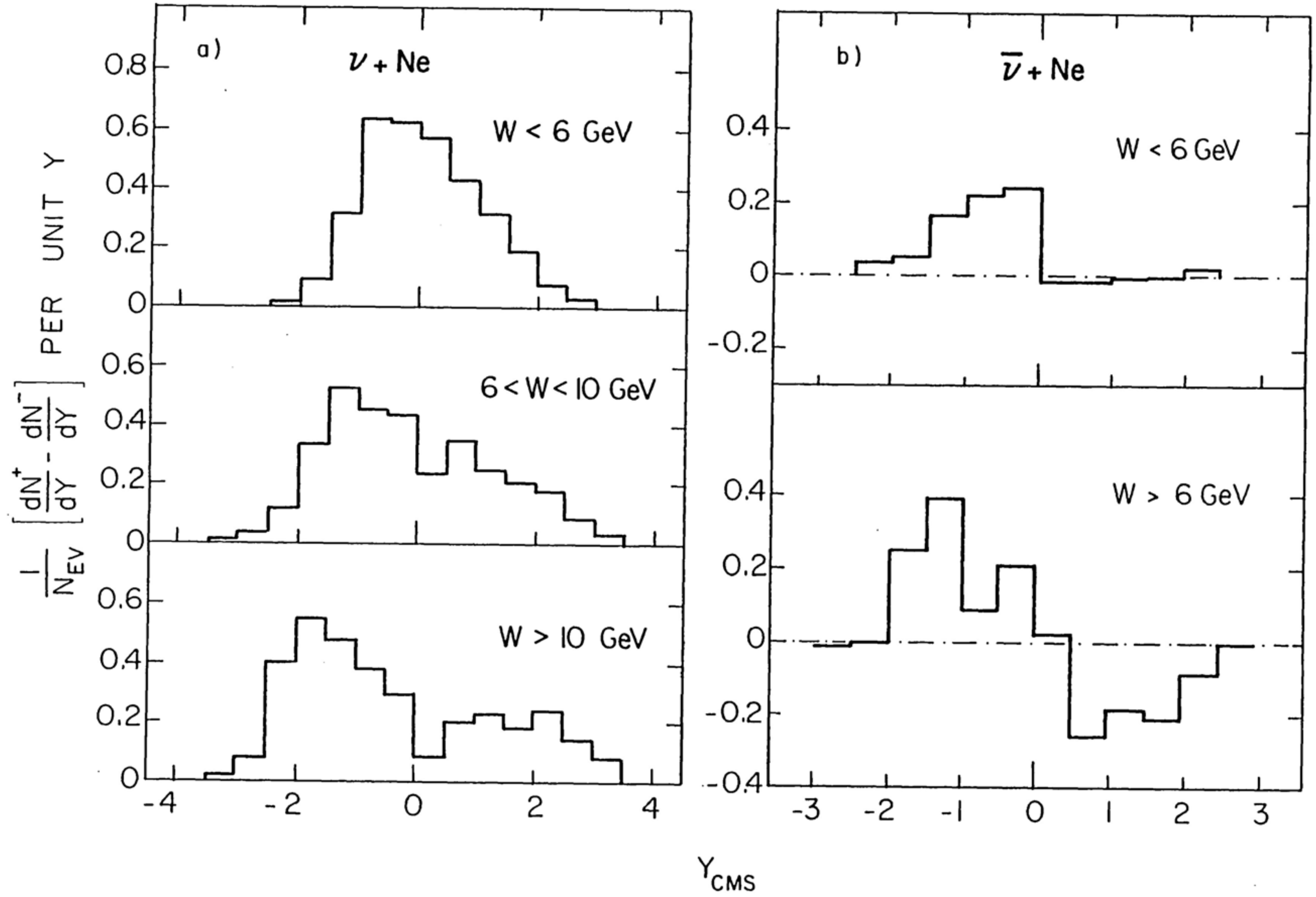

Fig 4.4 Distributions of centre of mass rapidity.

4.2.3 Results on Azimuthal Correlations

The $<\cos\phi>$ and $<\cos 2\phi>$ distributions are shown in Fig 4.5a for neutrino and Fig 4.5b for anti-neutrino data as a function of q^2. Also shown are the QCD predictions assuming |2|:

$$\eta = \frac{\text{Probability of gluon fragmentation}}{\text{Probability of quark fragmentation}}$$

$$= 1 \text{ (dotted line)}$$

$$0 \text{ (solid line)}$$

evaluated at $<E_\nu> = 100$ Gev. The z and y dependence of $<\cos\phi>$ and $<\cos 2\phi>$ are shown in Fig 4.5c and 4.5d respectively. It is evident that although $<\cos 2\phi>$ is consistent with the small predicted effect, except at low q^2 where the QCD calculations is not very reliable, $<\cos\phi>$ is inconsistent with the prediction particularly for the anti-neutrino data if (as expected) $\eta \sim 1$. The latter however does not necessarily go against the predictions because of the known sensitivity of $<\cos\phi>$ on the axis as discussed above.

The values of $<\sin\phi>$ and $<\sin 2\phi>$ are predicted to be zero in 1st order QCD. The distribution of $<\sin 2\phi>$ is consistent with this, Fig 4.5f, (which is an indication that the hadronic axis does not induce substantial effects in $\cos 2\phi$ and $\sin 2\phi$ if the prediction is reliable), but $<\sin\phi>$ shows a non-zero value which depends on q^2. The non-zero $<\sin\phi>$ is however again attributable to the effects of the axis.

The mean values of $\cos\phi$ and $\cos 2\phi$ weighted by x.y.z which are expected to be independent of the fragmentation functions of quarks and gluons |2| are shown in Fig 4.5e. Again only the sign of the

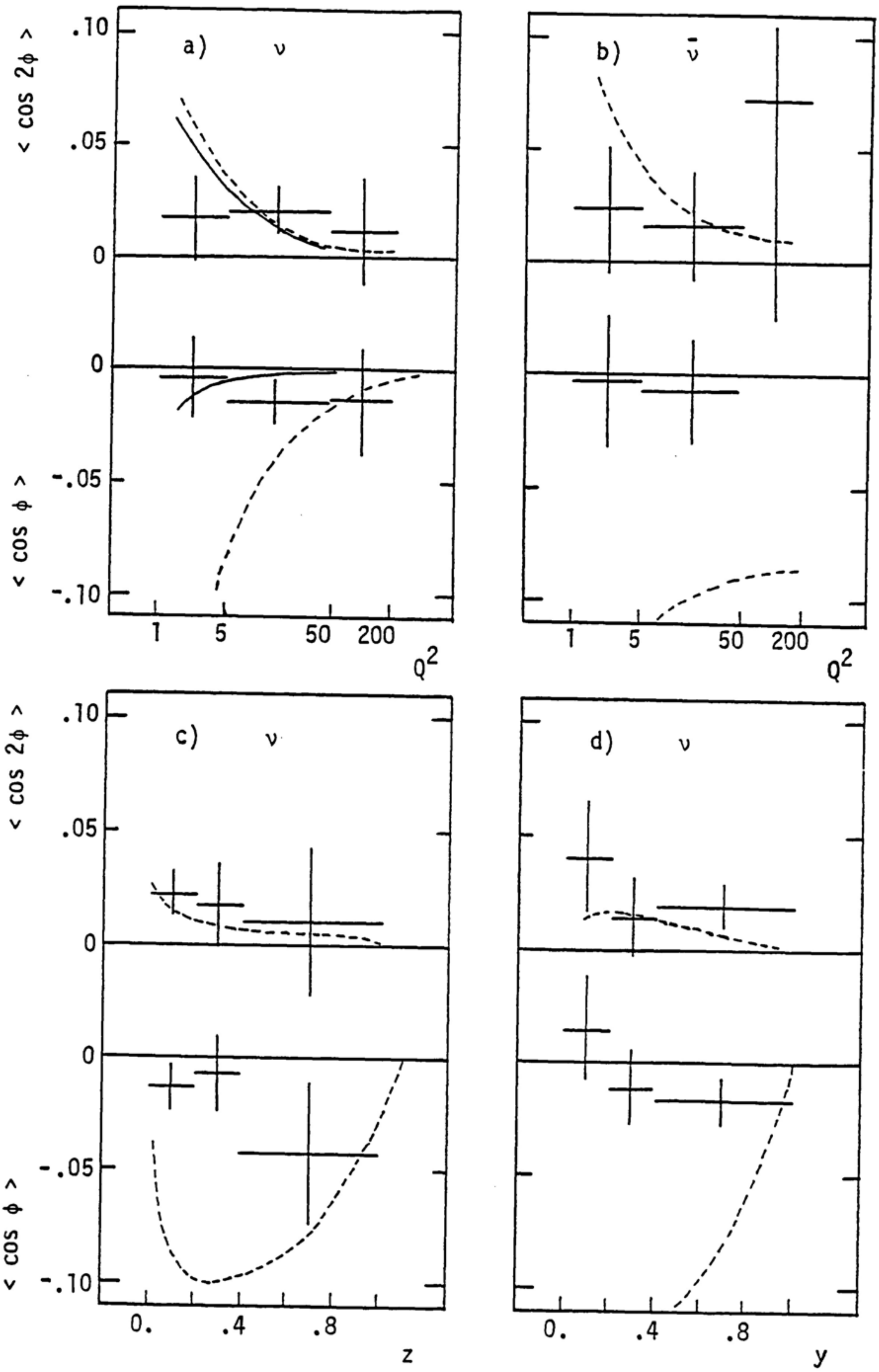

Fig 4.5 (continues on next page)

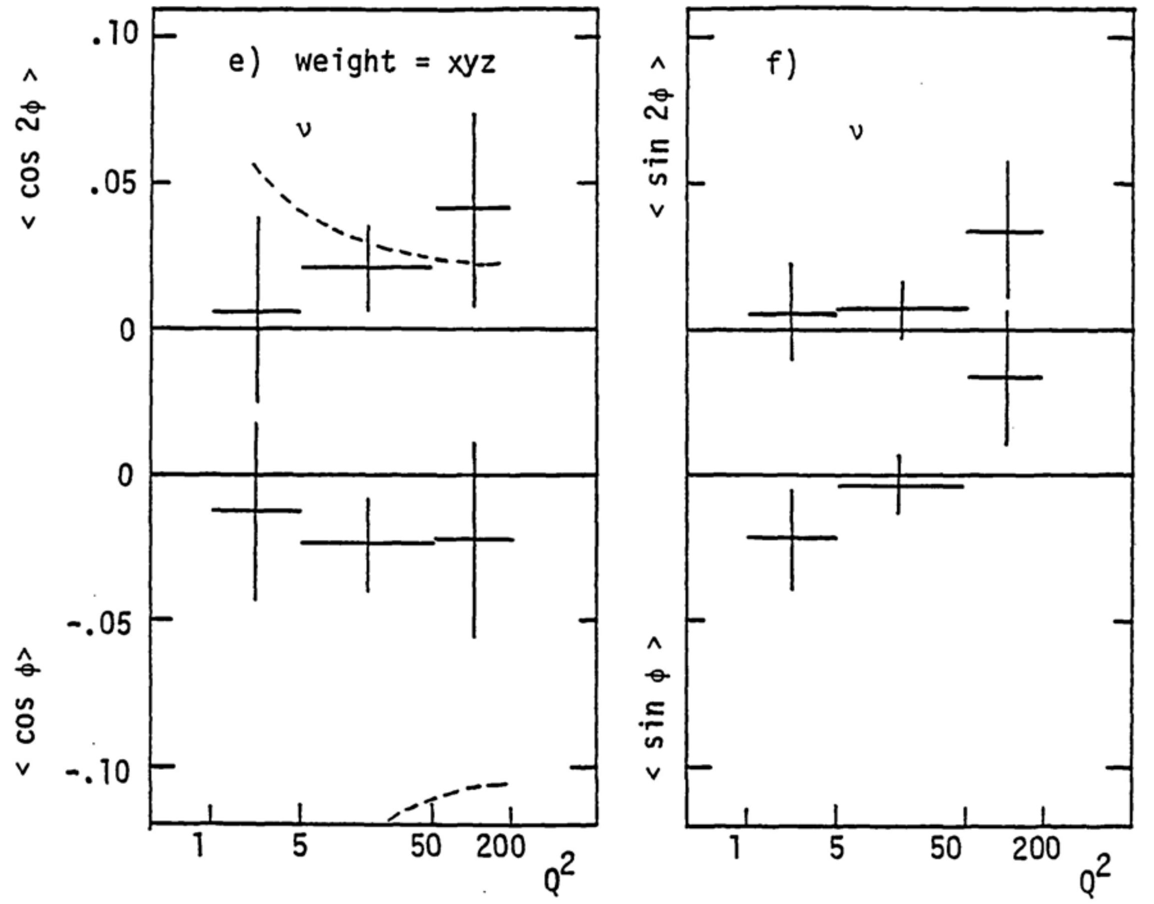

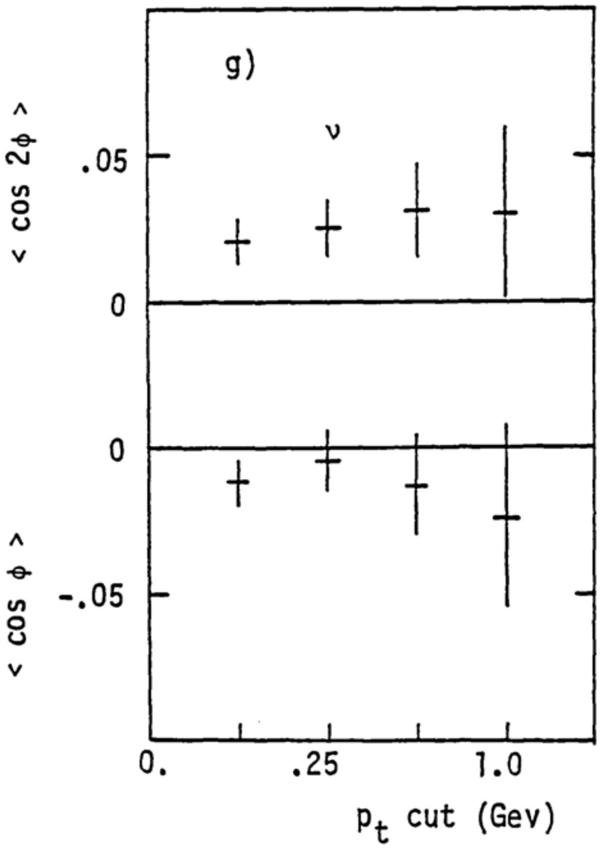

Fig 4.5 Azimuthal distributions relative to the hadronic axis. The lines are QCD predictions assuming $\eta = 1$ (dotted) and $\eta = 0$ (solid).

expected effect is reproduced by the data.

Since QCD processes are expected to contribute to the tail of the p_t distribution due to the hard gluon emission an increase in $<\cos 2\phi>$, is expected (although not necessarily in $<\cos\phi>$ since theoretically this decreases rapidly with z (Fig 4.5c) and the larger p_t values will be associated with a correspondingly larger value of z). The effects on $<\cos\phi>$ and $<\cos 2\phi>$ of various lower p_t cut-off is shown in Fig 4.5g. A slight increase in the magnitude of both variables is observed, but the larger errors do not allow conclusion of a firm trend to be drawn.

4.2.4 Non-Perturbative effects

The comparisons made above were with the perturbative (or calculable) part of QCD. The non-perturbative effects, although not explicitly calculable have been parameterised by introducing 'intrinsic' or 'primordial' transverse momentum (k_t) distributions in the quark density functions and fragmentation functions |3|. The effect of this is to introduce asymmetries which are similar to those due to perturbative QCD:

$$<\cos\phi> \sim \frac{<k_t>c_1}{Q}$$

$$<\cos 2\phi> \sim \frac{<k_t^2>c_2}{Q^2}$$

where $<k_t>$ is the transverse momentum relative to the current direction; and c_1 and c_2 arise due to the phenomenological width (p_t^{fr}) of the 'jet' of hadrons caused by the fragmentation process and lies between o (when $k_t < p_t^{fr}$) and 1 (when $k_t >> p_t^{fr}$). The sign of the asymmetry is the same as that for the perturbative case (ie negative for cos ϕ and positive for cos 2ϕ), but the magnitude falls much more rapidly compared with the perturbative case which is predicted to go as:

$$<\cos\phi>, <\cos 2\phi> \sim \frac{1}{\ln(q^2)}$$

The size of the non-perturbative effect is small for $<k_t> \sim$ 0.3 Gev in $<\cos\phi>$ and negligible for $<\cos 2\phi>$. However for $<k_t> \sim$ 0.6 Gev the effect in both is comparable to the perturbative one. Since present experiments indicate a value $<k_t> \sim$ 0.6 Gev, (section 4.6) the observed effects in $<\cos 2\phi>$, may only be partly due to perturbative QCD.

In conclusion tests of QCD in the azimuthal distribution of final state hadrons requires large statistics in the low q^2 region, where the effects are largest, and a good knowledge of the current direction so that effects in cos ϕ, which are much larger than in cos 2ϕ, can be tested. Separation of non-perturbative from perturbative effects is very difficult, even under these conditions.

Distributions in Transverse Momentum

4.3 Systematic Effects

Smearing effects involved in the determination of the hadronic axis can lead to uncertainties, of $\Delta\theta$, in its direction (see section 4.2.1); which can cause systematic shifts in the measured transverse momenta. The size of these effects is determined in this section using the Monte Carlo data.

Analysis of the Monte Carlo shows that rejection of badly measured tracks ($\Delta p/p \gtrsim 30\%$) is essential in order to reduce systematics, (eg The shift in $<p_t^2>$ at $w^2 \sim 100$ (Gev), due to measurement errors is reduced from ∿100% to ∿10% by this cut). The results presented have been obtained by applying exactly the same procedures to the Monte Carlo data as for the analysis of the data presented below (eg $\Delta p/p$ cuts, event selection criteria and energy loss corrections).

From the results presented in table 4.2 and table 4.3 (where unsmeared refers to the Monte Carlo with no experimental errors or energy losses, and smeared refers to the Monte Carlo with errors, and p_t^{out} is the transverse momentum measured relative to the lepton plane) the following conclusions can be drawn:

i) The systematic shift in $<p_t^2>$ and $<p_t^2>_{out}$ as a function of w^2 is less than ∿10%, as a result of smearing for the hadronic axis. For the current axis the effect is larger, being ∿20% at the highest w.

ii) Systematic shifts are larger for $<p_t^2>_{out}$ than for $<p_t^2>$, (∿10% and ∿5% respectively at the largest w). The low values of the shift in $<p_t^2>$, and the negative sign of the shift at low w, are due to the hadronic axis averaging out the effect of the missing neutrals.

iii) At fixed w the systematic change in $<p_t^2>$ as a function of z^* is less than ∿10% except in the largest z^* bin ($<|z^*|> \sim$

	$<w^2>$	$< p_t^2 >$		%	$< p_t^2 >_{out}$		%
		Unsmeared	Smeared	Shift	Unsmeared	Smeared	Shift
Hadronic Axis	10	108.4 ± 2.5	100.7 ± 2.4	-7.4	51.2 ± 1.7	53.7 ± 1.8	4.9
	24	128.8 ± 2.6	123.4 ± 2.5	-4.2	63.7 ± 1.7	65.9 ± 1.8	3.4
	47	128.3 ± 1.9	127.7 ± 2.0	-0.5	65.5 ± 1.3	68.8 ± 1.5	5.0
	92	127.7 ± 1.8	131.3 ± 2.0	2.8	64.1 ± 1.2	69.7 ± 1.5	8.7
	182	130.6 ± 2.5	136.9 ± 3.1	4.8	65.6 ± 1.6	72.9 ± 2.2	11.3
Current Axis	10	108.4 ± 2.5	113.7 ± 2.7	4.9	as above		
	24	129.8 ± 2.6	135.3 ± 2.8	4.2			
	47	128.3 ± 1.9	139.0 ± 2.3	8.3			
	92	127.7 ± 1.8	145.3 ± 2.6	13.8			
	182	130.6 ± 2.5	157.1 ± 4.7	20.3			

Table 4.2 Systematics in measurement of $< p_t^2 >$ and $< p_t^2 >_{out}$. $(\mathrm{Mev}/c)^2$

	z^*	$< p_t^2 >$		%	$< p_t^2 >_{out}$		%
		Unsmeared	Smeared	Shift	Unsmeared	Smeared	Shift
$1 < W^2 < 6$	-0.89	143.8 ± 10.4	151.2 ± 11.0	5.2	67.8 ± 6.8	80.4 ± 7.4	18.6
	-0.70	169.9 ± 10.3	176.7 ± 10.8	4.0	92.3 ± 7.9	93.2 ± 7.7	1.0
	-0.50	239.2 ± 13.1	220.1 ± 11.6	-8.0	110.7 ± 9.1	115.7 ± 8.4	4.5
	-0.28	167.2 ± 5.1	161.2 ± 48.9	-3.6	83.4 ± 3.7	85.4 ± 3.7	3.0
	-0.13	41.7 ± 1.2	40.4 ± 1.1	-3.1	21.1 ± 0.9	20.2 ± 0.8	-4.3
	0.13	42.0 ± 1.1	44.1 ± 1.1	-3.8	20.5 ± 0.8	21.5 ± 0.7	4.9
	0.29	143.3 ± 3.3	138.3 ± 3.1	-3.5	71.6 ± 2.4	71.2 ± 2.3	-0.6
	0.48	213.6 ± 8.2	208.1 ± 7.4	-2.6	108.2 ± 5.7	119.9 ± 6.6	10.8
	0.69	175.9 ± 12.7	154.0 ± 10.4	-12.5	80.0 ± 7.9	92.3 ± 9.2	15.4
	0.86	86.7 ± 18.5	98.9 ± 20.8	14.0	39.6 ± 10.7	52.3 ± 14.9	32.1
$8 < W^2 < 20$	0.78	145.3 ± 10.1	149.2 ± 11.3	2.3	75.7 ± 4.7	82.5 ± 8.5	7.7
	-0.50	211.2 ± 11.2	225.3 ± 12.6	6.7	94.1 ± 6.8	105.1 ± 8.7	11.7
	-0.28	196.1 ± 6.4	213.4 ± 8.1	8.8	98.3 ± 4.3	109.2 ± 5.5	11.1
	-0.10	88.2 ± 2.1	91.5 ± 2.3	3.7	43.9 ± 1.3	46.6 ± 1.6	6.2
	0.11	86.3 ± 1.7	83.3 ± 1.8	-3.5	44.5 ± 1.2	44.6 ± 1.4	0.2
	0.28	187.4 ± 4.3	191.4 ± 5.0	2.1	91.8 ± 3.0	101.3 ± 3.8	10.4
	0.48	219.8 ± 8.0	225.3 ± 10.5	2.5	114.0 ± 5.8	123.9 ± 7.5	8.7
	0.77	165.0 ± 15.6	193.2 ± 22.7	18.6	85.9 ± 9.8	128.7 ± 22.8	48.2

Table 4.3 Systematics in the Forward/Backward asymmetry using hadronic axis, p_t in Mev/c

0.75). At large z^* for $p_{t\,out}^2$ a shift of ∿20% at low w, (1 < w < 6 Gev), and ∿ 40% for high w, (8 < w < 20 Gev) is observed. For $<p_t^2>$ a shift of ∿2% at low w, and ∿20% at high w is observed. The effect of these systematics on the ratio of forward to backward transverse momentum is large only at the largest z^*, as shown by fig 4.10.

These observations suggest that use of the hadronic axis to measure p_t and the lepton plane to measure p_t^{out} does not introduce large systematics, except at large z^*. When integrated over z^* the effects are small because the data is dominated by the low $|z^*|$ region where such effects are small. The results of experimental data analysis are now presented relative to these.

4.4.1 Dependence on q^2, w^2 and x [4]

The average values of p_t^2 relative to the hadronic axis are shown for charged hadrons forwards in the centre of mass system in fig 4.6 as a function of q^2 and w^2. A significant rise in $<p_t^2>$ with w^2 is observed in both the neutrino and anti-neutrino data. The increase in the region $w^2 \lesssim 25$ Gev^2 may be attributed to the increase in phase space |5|. For larger w^2 the data suggests a linear dependence of $<p_t^2>$ on w^2 and a linear least squares fit for w > 4 Gev, and for w > 4, z > 0.2 gives the slopes shown in table 4.4

Gradient $\times 10^4$	Neutrino data	Anti-neutrino data
w > 4	3.7 ± 0.8	5.4 ± 1.9
w > 4, z > 0.2	8.1 ± 2.4	——

Table 4.4

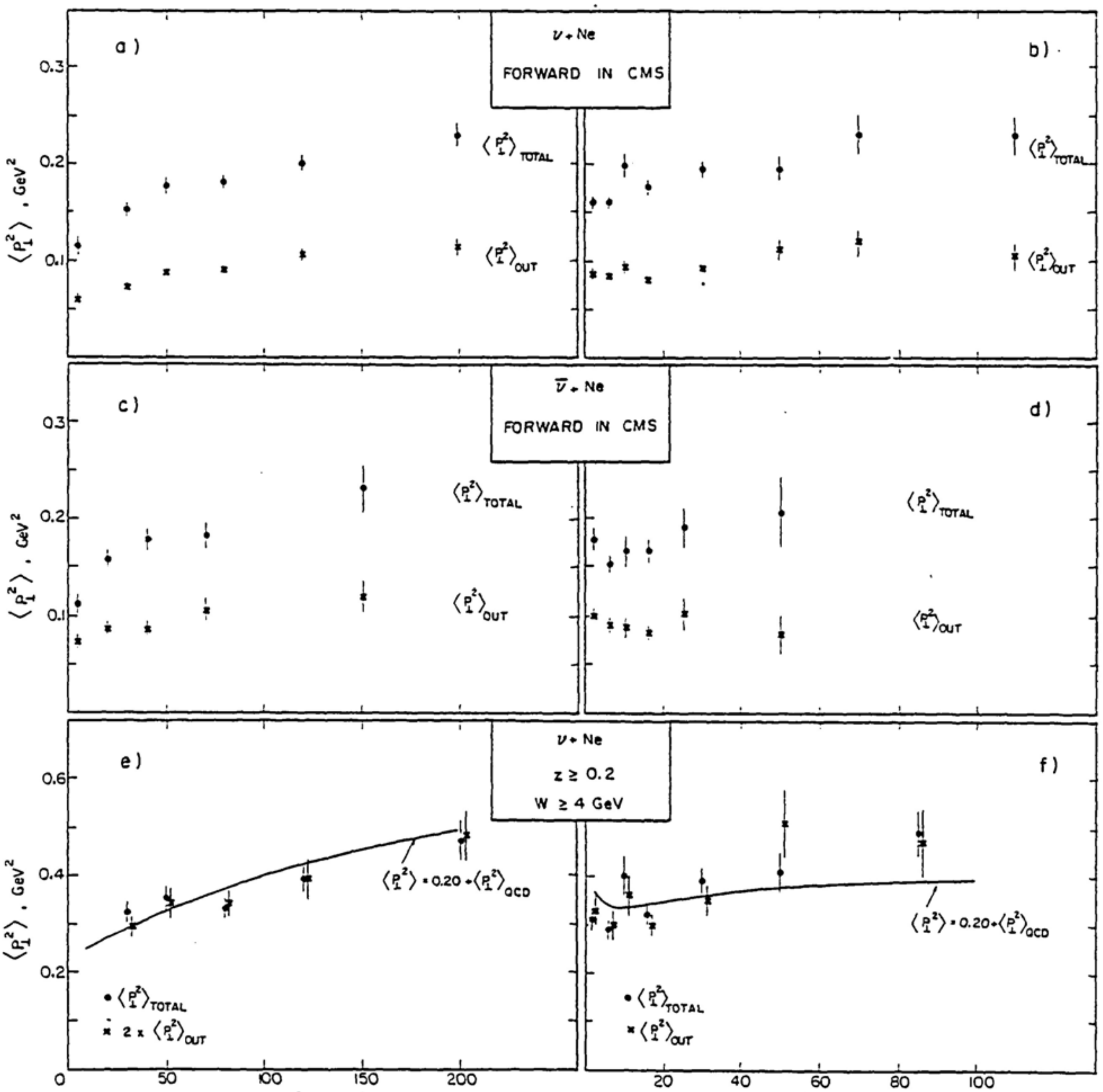

Fig 4.6 Q^2 and W^2 dependence of transverse momentum for Neutrino and Anti-Neutrino data. The solid lines are from a QCD calculation from ref. 9.

The slopes are significantly different from zero and the neutrino and anti-neutrino data are in quantitative agreement with each other. An increase in $<p_t^2>_{out}$, which is the transverse momentum component measured out of the lepton plane is also observed with a similar behaviour to $<p_t^2>$.

In the neutrino data, the $<p_t^2>$ also shows a dependence on q^2 (fig 4.6b and d), but within the large errors no such dependence is observed in the anti-neutrino data. This however can be explained by kinematics. The phase space available for high p_t particles depends on $w^2 = M^2 - q^2 + 2ME_\nu Y$. A given q^2 range will, by this formula, result in a lower range of w^2 in the anti-neutrino data compared to that in the neutrino data because of the softer spectrum in anti-neutrino interactions. This is confirmed by a cut on the anti-neutrino energy $E_{\bar{\nu}}$: for $E_{\bar{\nu}} < 100$ Gev, which gives a restricted w range a slight decrease in $<p_t^2>$ with q^2 is obtained whereas for $E_{\bar{\nu}} > 100$ Gev, where the w range is more extensive, an increase in $<p_t^2>$ with q^2 is obtained.

The $<p_t>$ calculated for positive and negative hadrons separately is given in table 4.5. In the forward region the positive and negative tracks give $<p_t>$ values which are consistent with each other for $w \gtrsim 6$ Gev. For $w \lesssim 6$ Gev the positive tracks give larger values than the negative tracks. In the backward regions the positive tracks give substantially higher values over the whole range of w. Comparison of the forward and backward regions shows that for positive tracks the $<p_t>$ for the backward region gives larger values than for the forward region, except at large w, whereas for negative tracks the forward tracks give larger values than the backward tracks. The different w^2 dependence of $<p_t^2>$ for negative tracks in the forward

$\langle p_t \rangle$ (Mev/c) / $\langle w \rangle$ (Gev)	Positive hadrons		Negative hadrons	
	$x_F > 0$	$x_F < 0$	$x_F > 0$	$x_F < 0$
2.7	300 ± 19	322 ± 15	202 ± 22	244 ± 23
4.8	326 ± 7	354 ± 6	300 ± 9	285 ± 8
7.0	333 ± 7	349 ± 7	327 ± 8	294 ± 9
8.9	343 ± 8	379 ± 8	348 ± 9	296 ± 9
12.3	382 ± 8	355 ± 7	376 ± 9	314 ± 11

Table 4.5 Comparison of the average transverse momentum relative to the hadronic axis for positive and negative hadrons in the current and target fragmentation regions.

and backward regions is shown in fig 4.7b.

Since average transverse momentum is expected to increase with increasing mass of particle |6|, these observations imply that there is substantial baryon contamination in the backward region, and in the forward region at small values of w at which the current fragments are not well defined. The fact that the positive and negative hadrons give similar values of transverse momentum in the current fragmentation region goes against the naive expectations of QCD. According to QCD if $\alpha_s < 1$, so that a hard gluon is not emitted in every neutrino event, then:

$$<p_t>^{h^-} > <p_t>^{h^+}$$

because the fragmentating quark is a flavour u, so producing more positive than negative hadrons, and the gluon is flavourless giving equal numbers of each. Thus the proportion of large p_t tracks, from the fragmentation of a gluon, is larger for negative tracks than for positive tracks.

In the Breit frame the outgoing parton in the first order QCD process, (fig 1.4 in chapter 1), can have a transverse momentum relative to the current direction, whereas in the quark-parton model diagram it cannot. The differential cross-section for the outgoing parton in the first order process is given by |7|:

$$\frac{d\sigma}{dp_t^2} \sim \frac{1}{p_t^2}$$

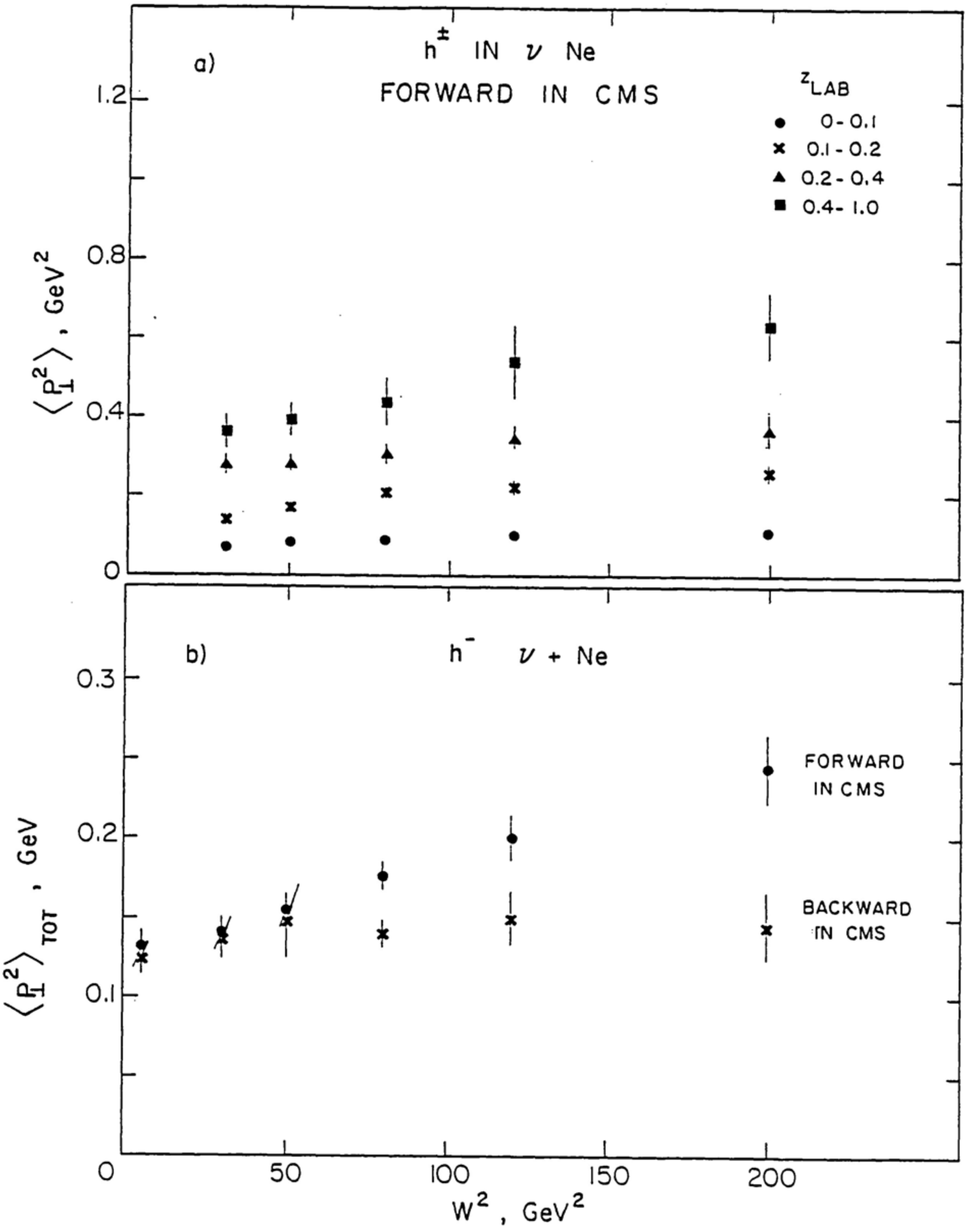

Fig 4.7 a) W^2 dependence of transverse momentum at fixed z, and

b) Comparison of transverse momentum of negative hadrons in the current and target fragmentation regions.

so that:
$$\langle p_t^2 \rangle_{\text{parton}} \sim \alpha_s (q^2) \int^q p_t^2 \frac{d\sigma}{dp_t^2} dp_t^2$$
$$\sim q^2 \alpha_s (q^2) + \text{constant.}$$

A more detailed analysis |8| shows that:

$$\langle p_t^2 \rangle_{\text{parton}} \sim q^2 \alpha_s f(x,y)$$
$$\simeq \frac{w^2 \alpha_s}{20} \qquad (2)$$

where the function f(x,y) is almost independent of y and is expected to depend on x in such a way that the variation with w^2 is in fact close to linear. The QCD calculation of reference 9 for the p_t^2 distribution of hadrons, based on the prediction of equation 2, for $z > 0.2$ and $w > 4$, and using a value of the QCD parameter $\Lambda = 0.74$ is compared to the neutrino data in fig 4.6e and f. The non-perturbative contribution consisting of the p_t, (∿ 300 Mev), from the parton fragmentation process and the primordial k_t (∿ 600 Mev), of the struck quark in the nucleon, has been assumed independent of w^2 and q^2. The QCD curves of fig 4.6e and f have been obtained by putting this contribution to 0.2 Gev^2, ie:

$$\langle p_t^2 \rangle = 0.2 + \langle p_t^2 \rangle_{\text{QCD}}$$

The w^2 dependence of the data is reproduced reasonably well, but the data exhibits a stronger q^2 dependence than predicted by this QCD calculation. It is also observed that the equality:

$$\langle p_t^2\rangle_{out} = \frac{1}{2}\langle p_t^2\rangle$$

which is expected in the case of azimuthal symmetry of hadron distributions about the current holds true to within about 10%, so lending support to the Monte Carlo prediction that systematic effects in the measurement of $\langle p_t^2\rangle$ and $\langle p_t^2\rangle_{out}$ are small.

The increase in $\langle p_t^2\rangle$ as a function of w^2 is a result of a slow rate of increase in $\langle p_t^2\rangle$ with w^2 at low z, and a relatively fast rate of increase with w^2 at high z as shown by fig 4.7a. The fact that $\langle p_t^2\rangle$ for negative hadrons increases with w^2 in the current fragmentation region but shows practically no dependence on w^2 in the target fragmentation region, fig 4.7b, is in qualitative agreement with the prediction of QCD which suggests that in a neutrino interaction the excited quark struck by a vector boson is likely to radiate a hard gluon more readily, and give an increase in $\langle p_t^2\rangle$ according to equation (2), than the target region di-quark system.

The x dependence of the average transverse momentum is shown in fig 4.8 for various regions of q^2 and w. At fixed w no x dependence is observed, (fig 4.8b). However at fixed q^2 an x dependence is observed, at low q^2. This is not due to phase space effects as shown by the fact that within errors no change in the x dependence is observed in the region w < 4 Gev, which is the region of restricted phase space (open circles in fig 4.8a). The observed dependence on x shows that the fragmentation functions in p_t do not factorise at fixed values of q^2 (at least in the region $q^2 \lesssim 10\ (\text{Gev}/c)^2$), but they are compatible with the hypothesis of factorisation at fixed w. (A more detailed analysis of factorisation is presented in chapter 6).

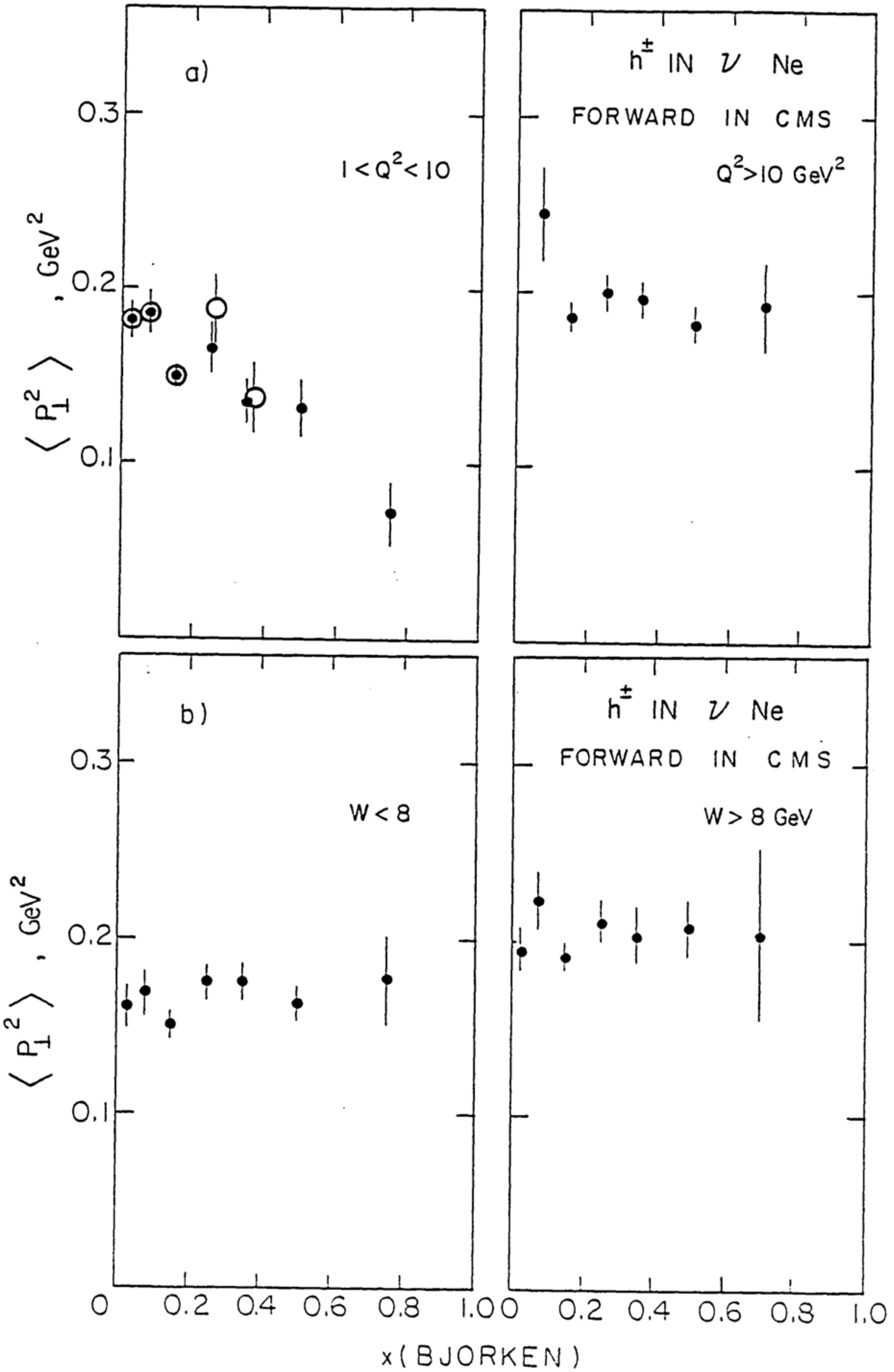

Fig 4.8 Tests of factorisation based on transverse momentum of hadrons. The open circles in a) are for the region w < 4 Gev.

4.4.2 Backward/Forward Asymmetries

The observation made from fig 4.7b, namely that the increase in $<p_t^2>$ with w^2 in the region $x_F > 0$ is much larger than in the region $x_F < 0$, is studied in more detail in this section in order to determine the difference between the current and target fragmentation regions and make a comparison with the predictions of QCD. This is done by looking at the z^*, ($z^* = 2E_h/w$ with z^* carrying the sign of x_F), dependence of $<p_t^2>$ and $<p_t^2>_{out}$ in regions of fixed low w ($<w> \sim 5$ Gev), and fixed high w ($<w> \sim 11$ Gev). For this analysis both positive and negative hadrons have been used, despite the nuclear proton contamination mainly in the backward region, in order to obtain sufficient statistics especially at large z. Since the effect of the contamination is to increase the $<p_t>$ in the backward region, an observed effect of a larger $<p_t>$ in the forward region compared to the backward region can only be enhanced by removal of this contamination, if it were possible.

Both $<p_t^2>$ and $<p_t^2>_{out}$, which is not sensitive to the determination of the axis, show an approximate symmetry between the forward and backward region at low w, (fig 4.9). This is not surprising since there is substantial mixing between current and target fragments at such low w. However at large w the forward region gives substantially larger values of transverse momentum compared to the backward region at fixed values of $|z^*|$. Such an effect may be caused by the larger errors on momentum of the forward track due to their larger average lab momentum, as indicated by the Monte Carlo for large values of z^* (section 4.3). The overall effect predicted by the Monte Carlo of this source of systematics is shown in Fig 4.10 where the ratio:-

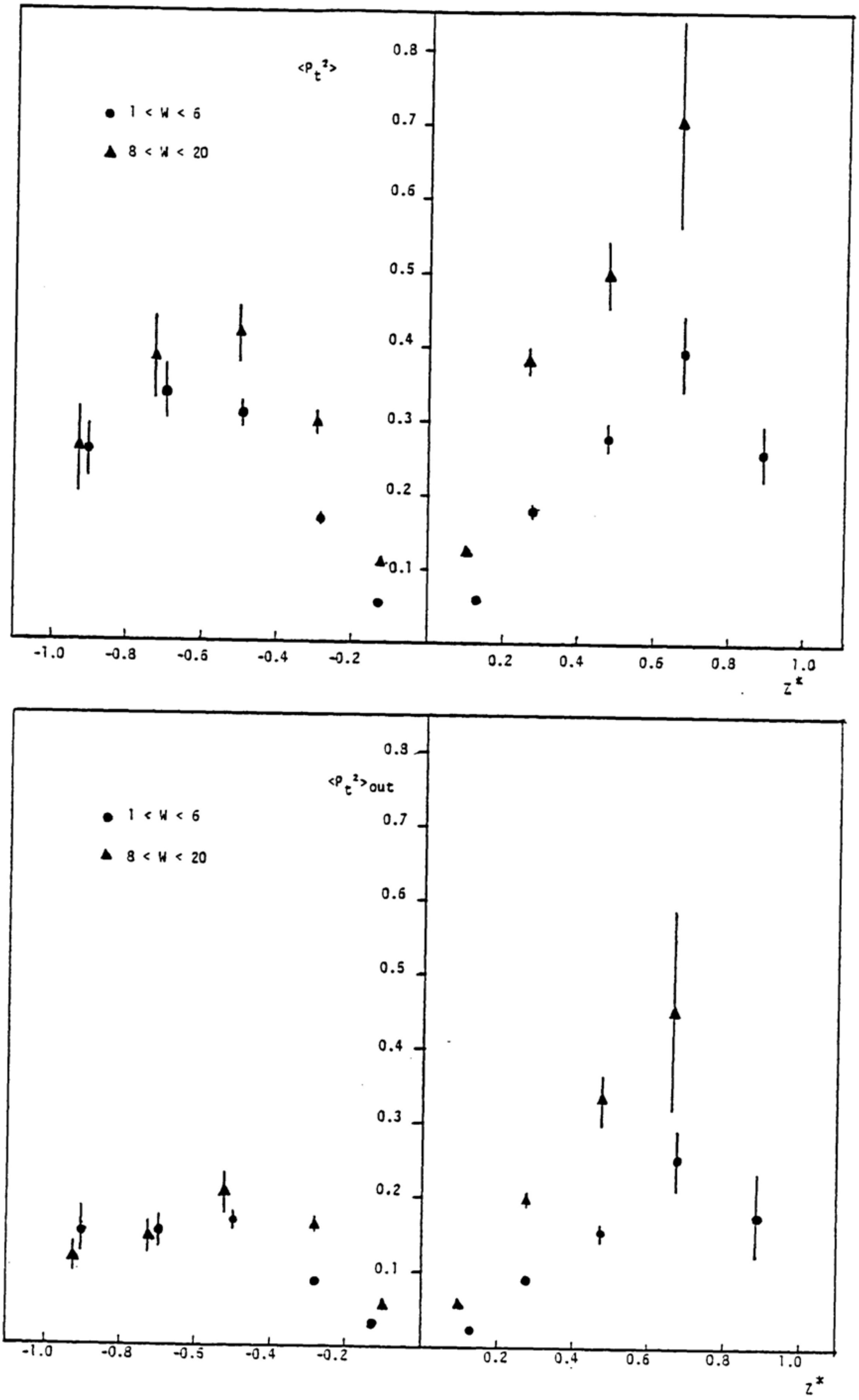

Fig 4.9 Transverse momentum of current (positive z^*) and target (negative z^*) fragments.

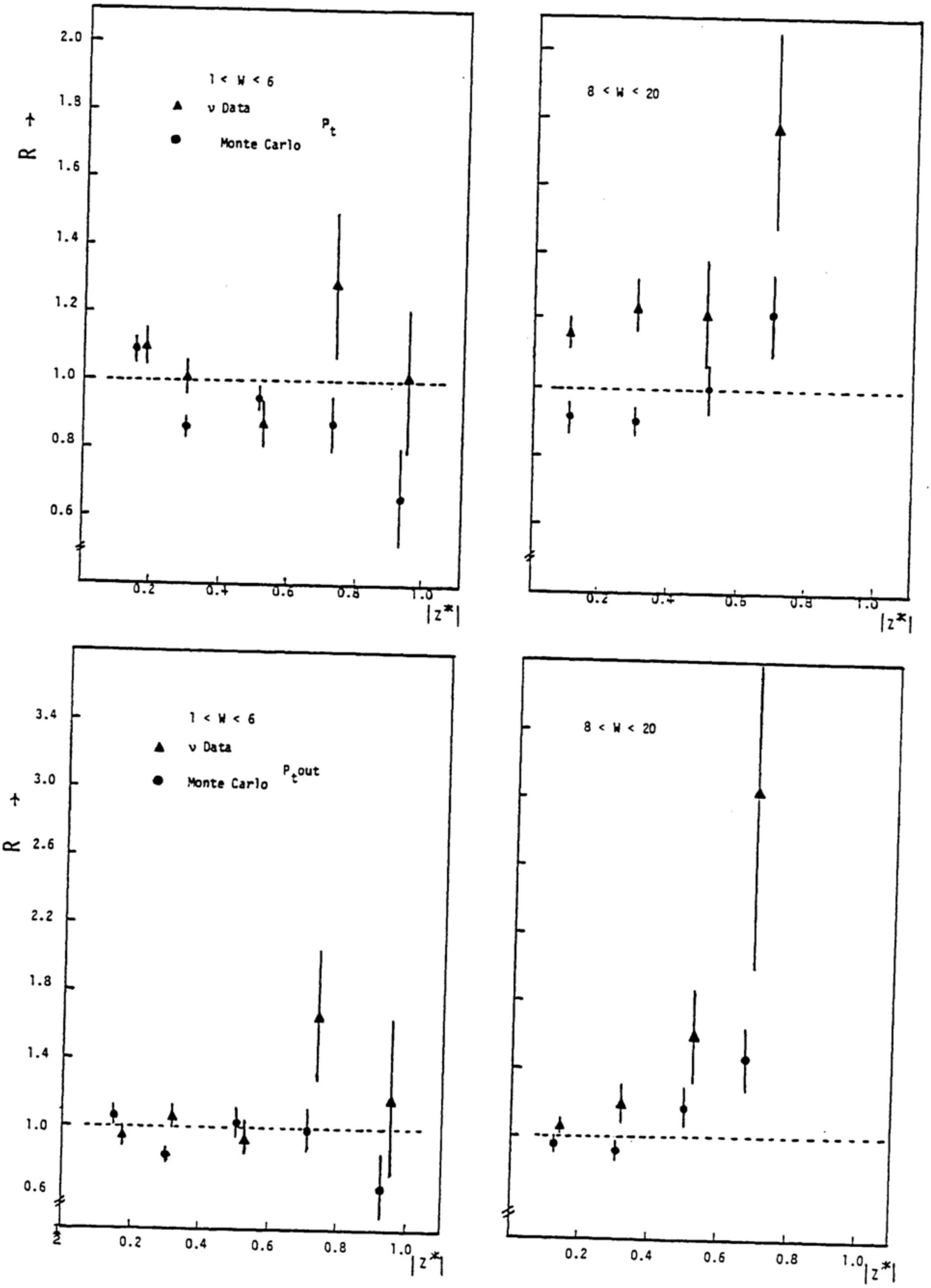

Fig 4.10 Z dependence of the ratio of forward/backward transverse momenta.

$$R = \frac{\langle p_t^2 \rangle_{\text{forward}}}{\langle p_t^2 \rangle_{\text{backward}}}$$

is plotted as a function of $|z^*|$. The ratio R is approximately one, and almost independent of $|z^*|$ at low w for $\langle p_t^2 \rangle_{out}$, but falls below one for the $\langle p_t^2 \rangle$ variable at large $|z^*|$. This fall is attributable to the correlation between the hadronic axis and hadrons with large z, which also tend to carry large transverse momentum as observed earlier. This suggests that the value of R is underestimated for $\langle p_t^2 \rangle$ at the largest values of z^*. Since there is little data in this region, and since $\langle p_t^2 \rangle_{out}$ is independent of this effect,no corrections have been applied. At large w the ratio is essentially flat with a value of about one for $|z^*| < 0.5$ and rises above one for $|z^*| > 0.5$, so that systematic effects are important only in this region of z^*.

The ratio R for the experimental data, also shown in fig 4.10, shows no uniform dependence on $|z^*|$ at low w, but at high w the value of R rises significantly above one, (and the Monte Carlo points), and continues to increase as a function of $|z^*|$ for both $\langle p_t^2 \rangle$ and $\langle p_t^2 \rangle_{out}$. Thus the experimental measurement errors do not describe the observed effects. However such an effect is expected in QCD due to the hard gluon Bremsstrahlung such that (see section 4.6),

$$\langle p_t^2 \rangle = \langle z^2 \rangle \langle p_t^2 \rangle_{\text{perturbative}} + \langle p_t^2 \rangle_{\text{non-perturbative}} \qquad (3)$$

If the non-perturbative part is assumed to be forward/backward symmetric, then the difference given by :

$$\Delta = \langle p_t^2 \rangle_{\text{forward}} - \langle p_t^2 \rangle_{\text{backward}}$$

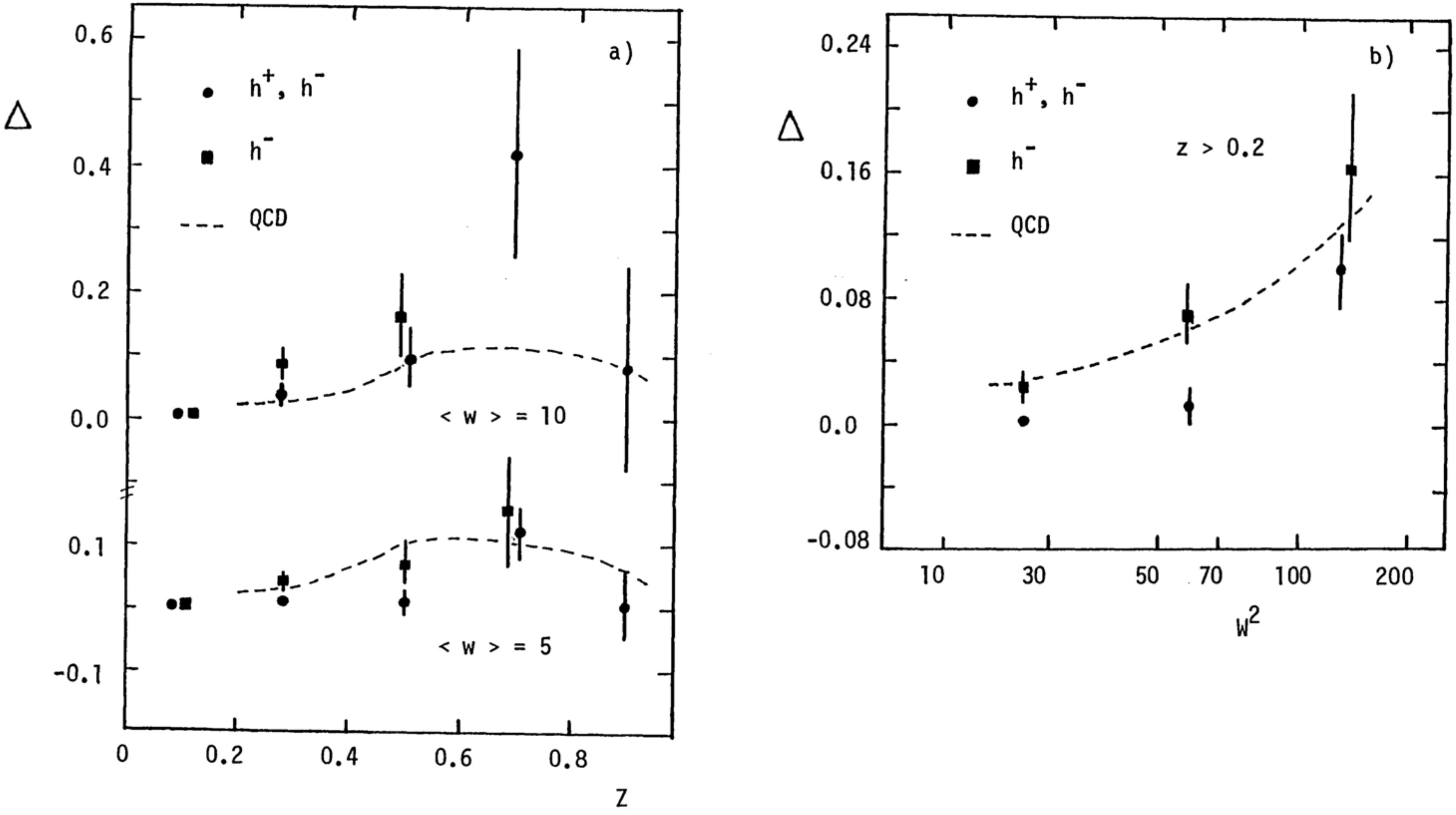

Fig 4.11 Difference in the $< p_t^2 >_{out}$ for forward (current) and backward (target) fragments compared with the prediction of QCD.

measures the perturbative part under the assumption that no perturbative effects occur in the region $x_F < 0$. The value of Δ is shown in fig 4.11b as a function of w for z > 0.2, compared to the theoretical prediction |10|, and as a function of z for two regions of high and low w in fig 4.11a. In the case of charged hadrons the predicted w^2 dependence is observed with a smaller magnitude, and $\Delta \sim 0$ at low w. However using negative hadrons only reproduces the size of the predicted effect and indicates that the discrepancy with the theory using all charged hadrons may be due to contamination by nuclear protons in the backward region, and low z forward region at low w, the occurrence of which was indicated earlier. The distinction between current and target fragmentation is also not clear at low w. The theoretical prediction describes the z dependence well at low w, but within the poor statistics, appear to underestimate the effect at large w, in the intermediate z range where data is available.

4.5 Comparison with other Processes

A direct comparison with final state hadrons from $e^+ e^-$ annihilations cannot be made because in νNe interactions the current and target fragmentation regions correspond to a quark and a di-quark fragmentation whereas in $e^+ e^-$ these correspond to fragmentation of a $q\bar{q}$ system. Thus only the current fragmentation region in ν interactions is directly comparable. In ν interactions a natural axis exists (the current direction), whereas in $e^+ e^-$ a maximization procedure is required to find the jet direction defined by the thrust axis (see chapter5 for definitions). This procedure is difficult to simulate in ν interactions because of the different physics involved in the target regions, and technically because a boost to the centre

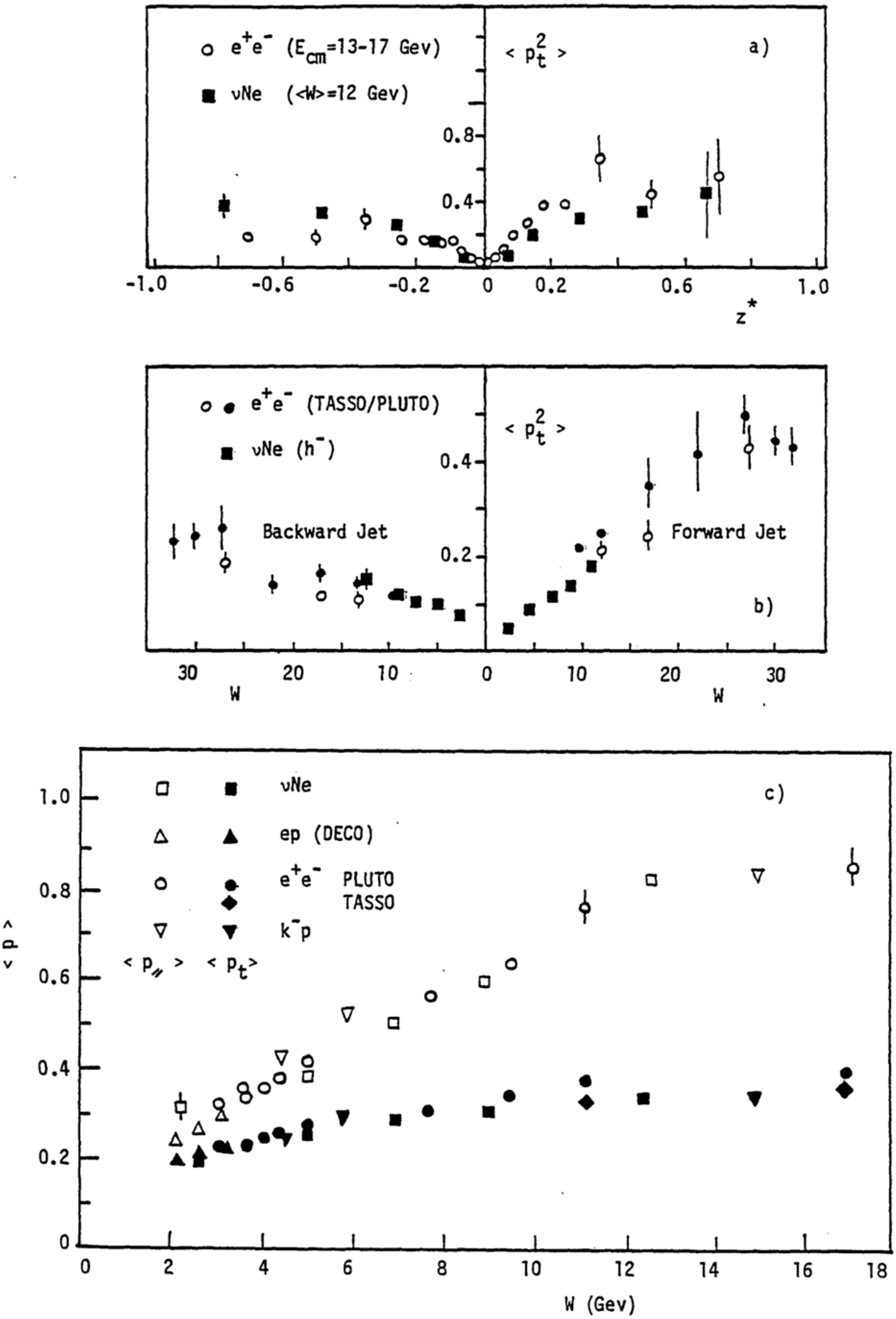

Fig 4.12 Comparison of the transverse and longitudinal momentum in Neutrino interactions with that in hadronic interactions, e^+e^- annihilations, and other leptonic interactions.

of mass system of the current-target is required and this tends to give a non-zero p_t between the forward and backward jet due to inaccuracies in the energy correction of the ν energy and neutral particle loss. In order to avoid these problems, separate thrust axes for the hadrons labelled as forward or backward, relative to the current direction, and defined from the vector sum of the forward or backward hadrons respectively, have been used. This method has been found to minimize p_t as well as the minimization procedure used in $e^+ e^-$ for large multiplicity events, and works better for low multiplicity events.

The dependence on z^* of the forward and backward (relative to the current direction) jets in ν interactions, and fat and thin jets in $e^+ e^-$ (defined as those with the largest and smallest $<p_t^2>$ relative to the jet axis respectively) is shown in Fig 4.12a. The ν points are lower than the $e^+ e^-$ points in the forward region |11|. This could be due partially to the choice of the jet with the largest $<p_t^2>$ as the forward jet, and partially to the higher $< w >$ for the $e^+ e^-$ data. The former could also explain the difference observed in the backward region, where the $e^+ e^-$ points are lower, although some differences in the di-quark fragmentation may also contribute to this discrepancy.

The w dependence of the forward and backward jets is shown in Fig4.12b for negative hadrons in order to avoid nuclear contamination. The ν data continues the trend of the higher energy TASSO data, but is lower that the PLUTO data in the forward region.

A comparison of $<p_t>$ and $<p_{/\!/}>$ with deep inelastic (ep), hadronic interaction (k^-p), and annihilation process ($e^+ e^-$) data is made in Fig 4.12c. There is good agreement between all these processes in the current fragmentation region. This would imply that the hadronisation process which converts the quarks/partons into observed hadrons must be similar in these cases.

4.6 Primordial k_t of quarks

In the framework of the quark parton model and QCD the transverse momentum of observed hadrons has contributions from three source:

i) Fragmentation process which converts quarks into observed hadrons (p_t^{fr})

ii) The primordial transverse momentum of the struck quark relative to the current (k_t).

iii) Recoil of quark against hard gluon Bremsstrahlung (p_t^{parton}).

The non-perturbative contributions, p_t^{fr} and k_t are as yet uncalculable. From the diagram:

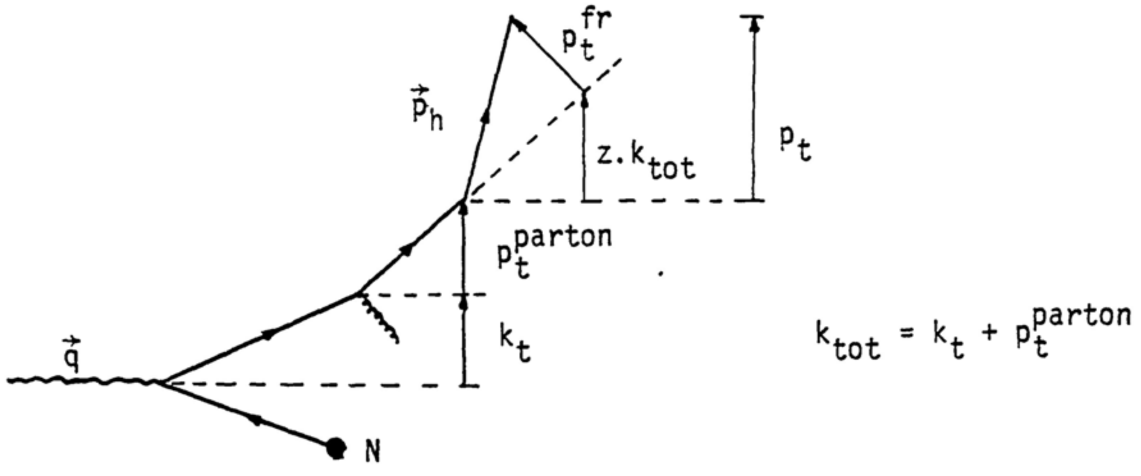

Fig 4.13

where the current interacts with a quark carrying a transverse momentum component k_t, and the observed hadron carries off a fraction z of the outgoing parton momentum, the transverse momentum of the hadron is given by:

$$\vec{p}_{t_h} = z\,(\vec{k}_t + \vec{p}_t^{\,parton}) + \vec{p}_t^{\,fr}$$

so that: $$p_{t_h}^2 = z^2(k_t^2 + p_t^{2\ parton}) + p_t^{2\ fr}$$

ie: $$<p_t^2>_h = <z^2><k_t^2> + <p_t^2>_{QCD} + <p_t^2>_{fr} \qquad (4)$$

where the azimuthal angles have been integrated over and small terms neglected |2|.

An estimate of p_t^{fr} and k_t^2 can be obtained from a linear fit to the observed p_t^2,with the QCD contribution substracted ($p_{t_{sub}}^2$), as a function of z^2. $p_t^{2\ fr}$ is then given by the constant term and k_t^2 by the gradient. However in obtaining $< p_t^2 >$ relative to the hadronic axis as a function of z^2 correlation between the fastest tracks and the hadronic axis, especially at low multiplicities, have to be accounted for. The effect of the correlations is illustrated by Fig 4.14a where a cut on the observed multiplicity ($n \lesssim 6$) has been made. The linear z^2 dependence observed for large multiplicity events, is affected by the axis determination at low multiplicities. In order to avoid this problem only events where the hadronic axis subtends an angle of less than 1^o with the current axis have been used. Since however much of the weight in the fit comes from points at $z^2 < 0.2$ and this selection affects mainly the points at $z^2 > 0.2$, the parameters of the fit are not changed very much (∿ 20%). The data (shown in Fig 4.14b) gives the results shown in table 4.6.for the parameters of the fit.

The QCD prediction is from reference |9| where it is given as a function of z^2 in bins of w. Since however no systematic w dependence was observed in the parameters of the fit, within large errors, the w dependence has been averaged over. The QCD calculation is expected to be reliable only for $z > 0.2$ and $w > 4$ Gev.

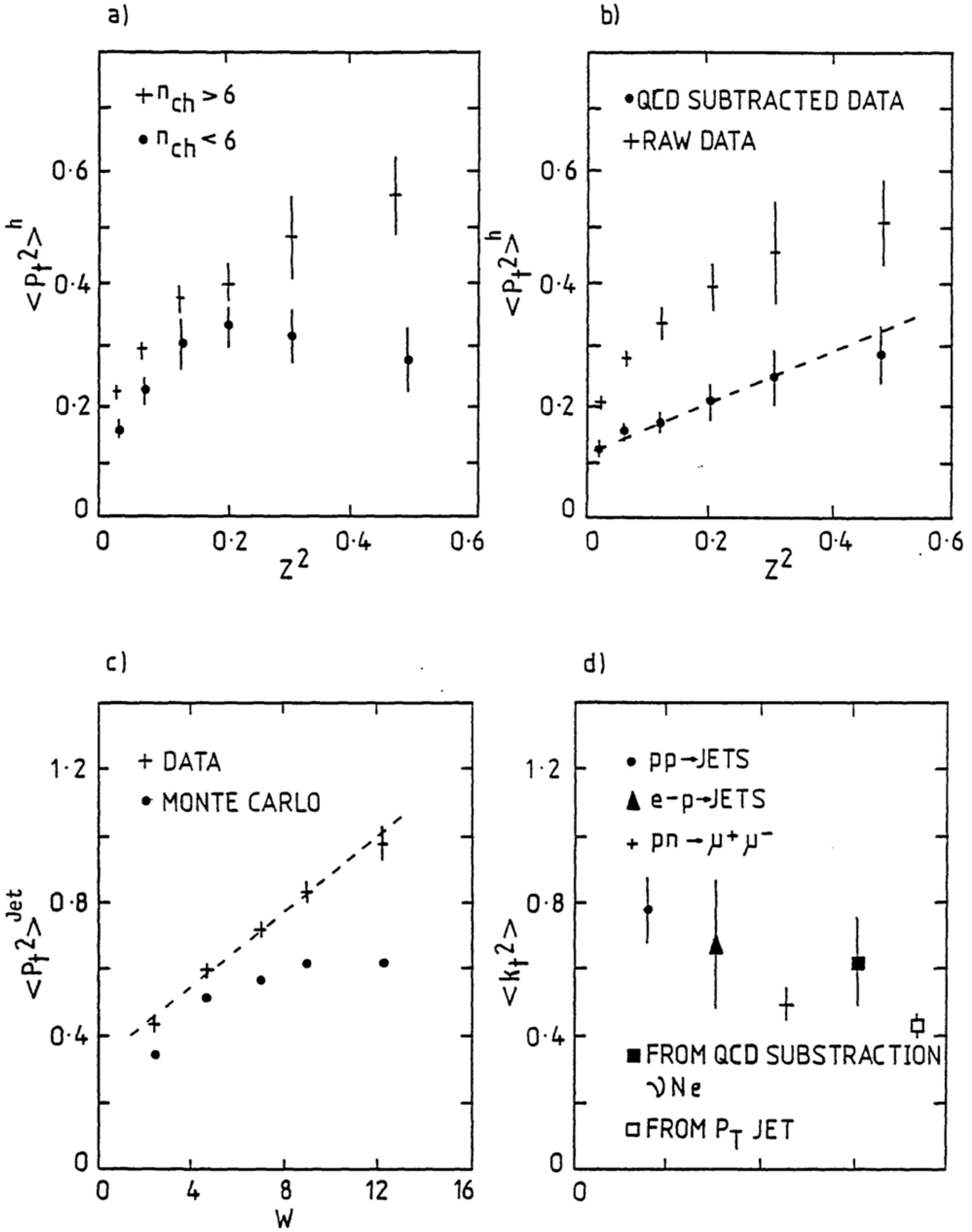

Fig 4.14 a), b) z^2 dependence of transverse momentun of hadrons and, c) energy dependence of transverse momentum of current jet; d) shows the values of primodial transverse momentum obtained from the two methods discussed.

$<z^2>$	$<p_t^2>$	$p^2_{t\ QCD}$	Fit to $y = mx + c$
0.02	0.199 ± 0.007	0.082	
0.06	0.274 ± 0.012	0.128	$z > 0.2$ $w > 4$
0.12	0.335 ± 0.027	0.172	$m = 0.385 \pm 0.174$
0.20	0.397 ± 0.041	0.199	$c = 0.121 \pm 0.022$
0.30	0.456 ± 0.087	0.217	
0.47	0.509 ± 0.227	0.227	

Table 4.6

The parameters from the fit imply rms values of primordial transverse momentum and a fragmentation transverse momentum (statistical errors):

$$k_t^{rms} = 620 \pm 140 \text{ Mev}$$
$$p_t^{fr} = 350 \pm 30 \text{ Mev}$$

The value of k_t is in good agreement with that obtained from other processes as shown in fig 4.14d, and the value of p_t^{fr} is in good agreement with the value 380 Mev measured in $e^+ e^-$ annihilations at $E_{cm} = 13$ and 17 Gev.

The value of k_t, rather than its rms value, can potentially be determined as follows. The transverse momentum of the forward hadron jet is given by:

$$p_{t\ jet} = \sum_{x_F > 0} \vec{p}_h \quad \sin\theta$$

where θ is the angle between the hadronic axis and hadron of momentum p_h. A non-zero value of $p_{t\ jet}$ can arise if the struck quark has primordial k_t. The fragmentation p_t will make a vanishing contribution as w tends to zero so at w = 0, any residual $p_{t\ jet}$ can be interpreted as being due to the k_t of the struck quark, (in the absence of systematics).

The $<p_t>_{jet}$ is shown in fig 4.14c as a function of w together with the values obtained from the Monte Carlo program. The Monte Carlo shows a rapid rise from zero (kinematically $<p_t>_{jet}$ must equal zero at w = 0) and flattens off at large w. The data however show a linear rise in $<p_t>_{jet}$ over the whole range of w. A straight line fit to the data points givesa value of $<k_t> \sim 300$ Mev (intercept). This value is however found to vary with a lower cut on the event multiplicity (eg if a charged multiplicity cut $n_{ch} > 3$ is used the value $<k_t> \sim 400$ Mev is obtained), due to the problems associated with the hadronic axis which tends to reduce the $p_{t\ jet}$ compared to the value relative to the true current. Thus $<k_t>$ is expected to be greater than $\sim$300 Mev. If however $<p_t^2>_{jet}$ is obtained as a function of w^2 (so that the intercept now gives $<k_t^2>$ so providing a check on the value of $<k_t^2>$ obtained by the QCD subtraction method) the sensitivity of the intercept on the event multiplicity becomes negligible. This is because events with large $p_{t\ jet}$ are given more weight, and these tend to have larger multiplicities. The values of $<p_t^2>_{jet}$ as a function of w^2 together with the results of a straighter line fit are shown in table 4.7.

The value of the intercept thus implies $k_t^{rms} = 440 \pm 20$ Mev, where the errors are statistical only. This value is slightly smaller, but not in disagreement with the value obtained from the method based on subtraction of QCD effects. A comparison of the values of k_t^{rms} obtained from other processes is made in fig 4.14d. There is good agreement between the various estimates.

$<w^2>$ Gev^2	$<p_t^2>_{jet}$	Fit to $y = m\,w^2 + c$
10	0.296 ± 0.017	m = 0.012 ± 0.001
24	0.565 ± 0.042	c = 0.195 ± 0.014
47	0.722 ± 0.042	$= k_t^2$
92	0.201 ± 0.141	
180	3.259 ± 1.196	

Table 4.7

4.7 Determination of α_s (q^2)

The increase in hadron transverse momentum due to the QCD Bremsstrahlung process is given by the second term appearing in equation (4). Substituting for the transverse momentum square of the parton from equation (2) this yields:

$$<p_t^2>_h^{QCD} \simeq \frac{\alpha_s(q^2)}{20} <z^2><w^2>$$

The other terms appearing in equation (4) are independent of w^2 so that if the increase in hadron transverse momentum is attributed to QCD, the gradient of a plot of $<p_t^2>_h$ against $<z^2>$ $<w^2>$ gives an estimate of α_s. The values of α_s obtained from such a plot are given in table 4.8 for various q values, using the variable z^* (results using z_{lab} agree within errors). Since at low z^* phase space leads to an increase in transverse momentum (seagull effect), results are also given for $z^* > 0.2$ in order to reduce such effects, assuming that equation (5) is still valid. The two sets of results agree within errors.

$\langle q^2\rangle$ \ α_s	$x_F > 0$	$z^* > 0.2$, $x_F > 0$	Theory
2.8	0.42 ± 0.06	0.51 ± 0.08	0.62
9.3	0.42 ± 0.03	0.38 ± 0.03	0.42
19.4	0.23 ± 0.02	0.29 ± 0.06	0.35
48.9	0.29 ± 0.03	0.20 ± 0.05	0.28

Table 4.8

There is evidence of a decrease in the value of α_s at high q^2 compared to its value at low q^2, and for $z^* > 0.2$ shows agreement within errors with the theoretical prediction obtained from:

$$\alpha_s = \frac{12\pi}{(33-2m)\ln(q^2/\Lambda^2)} \qquad \text{where } m = \text{number of quark flavours}$$

assuming $\Lambda = 0.5$ and four quark flavours.

Summary

i) Asymmetries in the azimuthal distribution of hadrons have been observed in $\langle \cos 2\phi \rangle$. However statistics do not make the effect statistically very significant. The size of the asymmetry is in approximate agreement with perturbative QCD, but non-perturbative QCD predicts similar effects.

ii) The distributions of p_t^2 of hadrons agree well with model calculations based on QCD. A difference between the forward and backward jets has been observed which cannot be explained by experimental bias, and is in approximate agreement with QCD.

iii) The primordial k_t of the target quark has been measured and found to agree with the value obtained from other processes. The coupling constant α_s has been estimated and found to show reasonable agreement with theoretical predictions.

References

1 H Georgi and H Politzer, Phys. Lett. 40, 3 (1978)

2 G Kopp, R Maciejko, P M Zerwas, Nucl. Phys. B144, 123 (1978)
J Cleymans, Phys. Rev. D18, 954 (1978)
A Mendez, Nucl. Phys. B145, 199 (1978)
A Mendez, A Raychaudhuri, and V J Stenger, Nucl. Phys. B148, 123 (1978)
Topical Conference on Neutrino Physics at Accelerator Energies (Oxford) 1978

3 R N Cahn, University of Michigan preprint, UM-HE 78-22 (1978)

4 P C Bosetti et al, ABCDLOS Collaboration, CERN/EP 80, Submitted to Nucl. Phys. B

5 P C Bosetti et al, ABCLOS Collaboration, Nucl. Phys. B149 (1979) 13-28

6 P Bossetti et al, Nucl. Phys. B60 (1973) 307-314

7 Editor J T T Van, Recontre de Moriond XIII Vol. 2 (1978) 395

8 G Altarelli and G Martinelli, Phys. Lett. 76B no. 1 (1978)
It has been pointed out by G Saitta (private communication) that the factor 1/32 appearing in the Altarelli and Martinelli version of equation 2 is incorrect, and integration of a formula due to A Mendez, reference 2, gives a factor 1/20.

9 P Mazzanti, R Oderico, V Roberto, Phys. Lett. 81B no. 2 (1979)
R Oderico, Private communication

10 R Oderico,private communication

11 Ch Berger et al, PLOTO Collaboration, Phys. Lett. 81B (1979) 410
Ch Berger et al, PLUTO Collaboration, Phys. Lett. 86b (1979) 418
R Brandelik et al, TASSO Collaboration, Phys. Lett. 83B (1979) 261
R Brandelik et al, TASSO Collaboration, Phys. Lett. 86B (1979) 243
The discrepancy between the PLUTO and TASSO data on transverse momentum is due to different corrections for the measuring efficiencies being applied in the two cases. PLUTO measures more of the neutral energy (used in the axis determination) whereas TASSO measures charged tracks with smaller measurement errors.

CHAPTER 5

Hadron Structure in Momentum Space

5.1 Introduction

In this section the hadrons resulting from neutrino interactions are studied using variables which describe the event shape in momentum space and in terms of momentum flow. By using a selected range of variables which can be calculated in perturbative QCD, checks are made on the applicability of QCD prediction in these variables in the energy regime of the data. A comparison is also presented of the momentum space structure of hadrons produced in e^+e^- and in purely hadronic interactions.

5.2 Determination of the Jet direction

Experimental measurements of the jet structure of hadrons in e^+e^- annihilations were first obtained relative to the sphericity axis |1|, whereas currently results and theoretical predictions are generally presented relative to the thrust axis. The definitions of these measurements of the jet direction of hadrons are presented below followed by a discussion of the accuracy of these jet measurements in estimating the true direction of the fragmenting quark.

5.2.1 Sphericity Axis

The sphericity axis is the axis relative to which the sum of the transverse momenta square of the individual hadrons is minimised. This axis is found by diagonalising the tensor given by |1|:

$$I_{\alpha\beta} = \sum_{i=1}^{n} (p_i^2 \delta_{\alpha\beta} - p_{i\alpha} p_{i\beta}) \qquad (1)$$

where n = event multiplicity

α, β = particle three momenta indices,

which is constructed by analogy with the tensor of inertia. The eigenvectors of the tensor which correspond to the eigenvalues λ_1, λ_2, λ_3, define an ellipsoid in momentum space and so give information about the three-dimensional structure of the event. The sphericity axis corresponds to the smallest eigenvalue λ_1, where $\lambda_3 > \lambda_2 > \lambda_1$. Each of the three eigenvalues give the transverse momentum of the hadrons relative to the three axes.

Since the transverse momentum enters the tensor quadratically, the sphericity axis weighs single particles with large p_t much more than many particles with the same p_t.

5.2.2 Thrust Axis

The thrust axis is the axis relative to which the longitudinal momentum of the hadrons is maximised. This axis cannot be found from an analytic equation as in the case of the sphericity axis and a method of numerical maximisation which has to be used can lead to false results due to the existence of local maxima |2|. An alternative method has been proposed in reference 2, whereby the thrust axis direction is determined from the combination of particle momenta which gives the largest vector sum of three momenta in the centre of mass system of the hadrons.

Thus in order to determine this axis, $(2^{n-1} - 1)$ particle combinations have to be performed, so that in practice the method can be applied only to relatively low (< 15) multiplicity events unless low energy tracks are treated separately. Alternatively, in neutrino interactions, the thrust axis can be estimated by making use of the known current direction: the three momenta sum of hadrons travelling forwards in the cm system of hadrons represents a first approximation to the thrust direction (t_1). This can then be used to find a better approximation to the thrust axis by taking the three momenta sum of hadrons travelling forwards relative to t_1. In practice this iterative procedure has been found unnecessary since the axis t_1 changes very little.

Monte Carlo studies carried out show that the axis t_1 agrees well with that determined using the combinatorial method of reference 2 (t_c), with an average angle between the two axes:

$$< \theta >_{t_c \cdot t_1} = 3.75^{\circ}$$

and 83% events subtending an angle less than 1° between them. The axis t_1 will thus be used in any reference to the thrust axis.

5.2.3 Thrust Axis vs Sphericity Axis for jet measurements

The distribution, obtained from the Monte Carlo data of the angle $\theta_{jet.s}$, between the true jet direction and sphericity axis, versus the angle $\theta_{jet.t}$, between the true jet direction and the thrust axis is shown in the two dimensional plot of Fig 5.1a. There is evidence of a correlation between the two axes. The distribution of events in $\theta_{jet.s}$ and $\theta_{jet.t}$ shown in Fig 5.1b and c respectively, gives $< \theta >_{jet.s} \sim 9.5^{\circ}$

Fig 5.1 Correlation of the sphericity and thrust axes to the true jet direction (a, b, and c). The effect on the correlation of introducing experimental errors (smearing) and using charged tracks only is shown in d) and e).

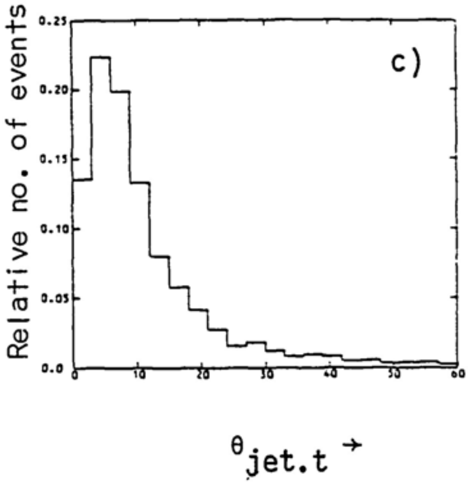

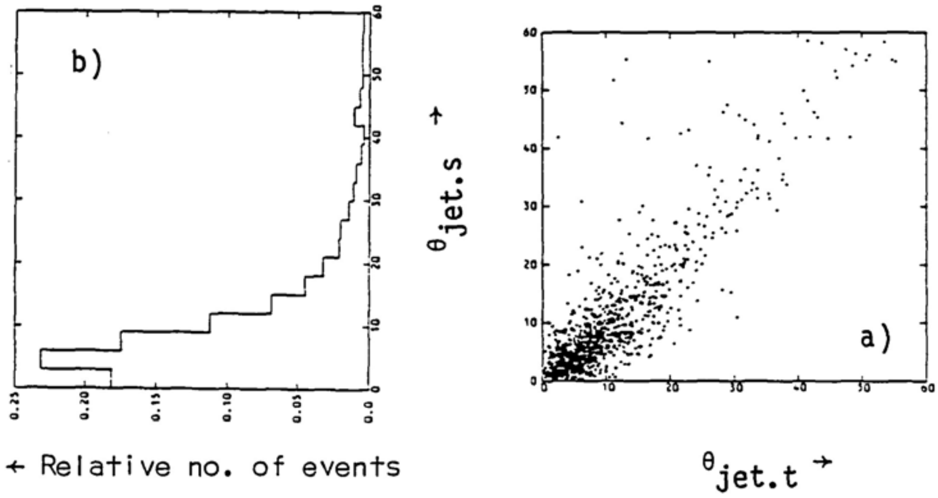

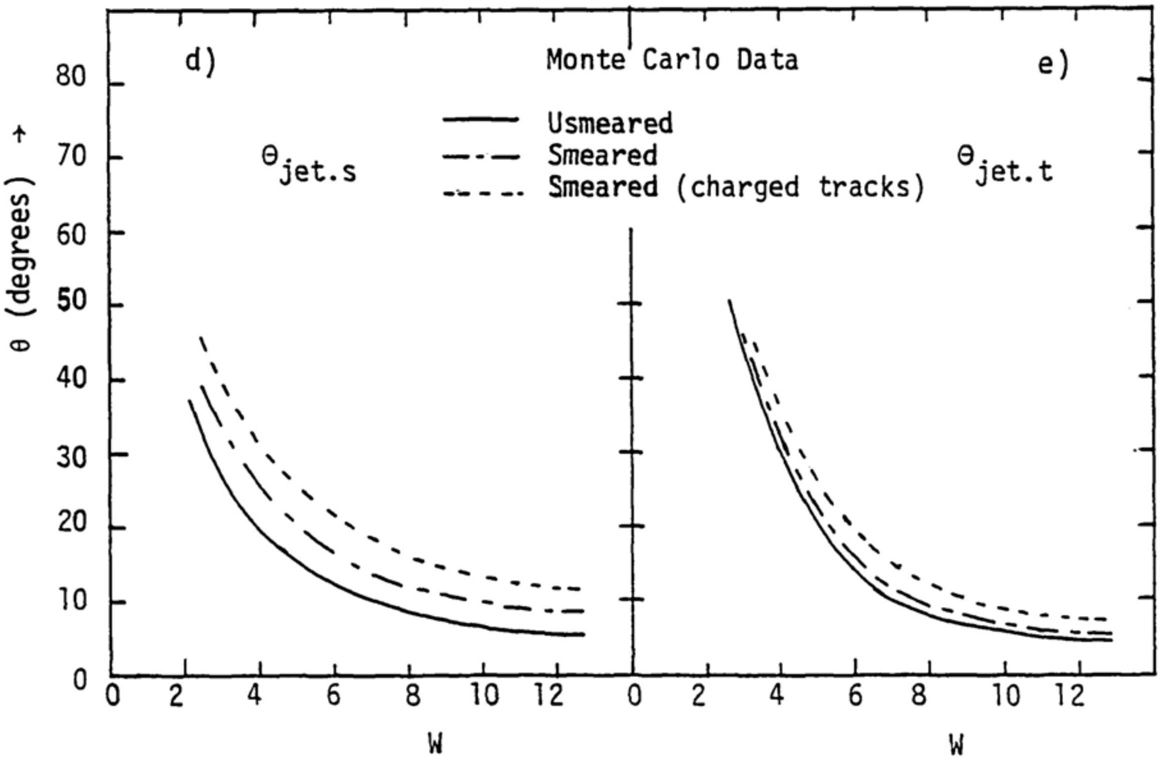

$< \theta >_{jet.t} = 9.8^o$. The w dependence of $\theta_{jet.s}$ (Fig 5.1d) and $\theta_{jet.t}$ (Fig 5.1e) show that the true jet direction is badly determined at low w, where a well defined jet of hadrons does not ex~~s~~ist and events appear quite spherical in momentum space, but fairly well determined at high w, where a better defined jet of hadrons ex~~s~~ists.

The effect of introducing measurement errors and neutral energy losses as in the experimental situation is to make the determination of the jet direction more inaccurate, as indicated by the dot-dash curves of Fig 5.1d and e. These curves give the typical uncertainties expected in estimating the jet direction in the experimental data. The results agree well with the Monte Carlo studies carried out in $e^+ e^-$ |3|, in the region $w > 10$ Gev. For energies $w > 5$ Gev the thrust axis is a slightly better estimator of the jet direction as indicated by the curves of Fig 5.1d and e. Also if only charged hadrons are used the determination of the jet axis becomes more inaccurate despite the smaller measurement errors on the charged tracks compared to the neutral tracks. All measured tracks will thus be used in determining the jet axis for the experimental data.

The distribution of the angle between the thrust and sphericity axes, $\theta_{s.t}$, (Fig 5.2a) shows a strong correlation between the two axis in the experimental data. The correlation improves with increase in the hadron energy w (Fig 5.2c), so leading to a more accurate determination of the jet direction at high energies. The thrust and sphericity axes are also strongly correlated to the track with the largest momentum as shown by the distribution of $\theta_{t.p_f}$ and $\theta_{s.p_f}$ respectively (Fig 5.2b). Again the correlation increases with w (fig 5.2d) and is strongest for the sphericity axis for which the momentum terms appear quadratically in the sphericity tensor.

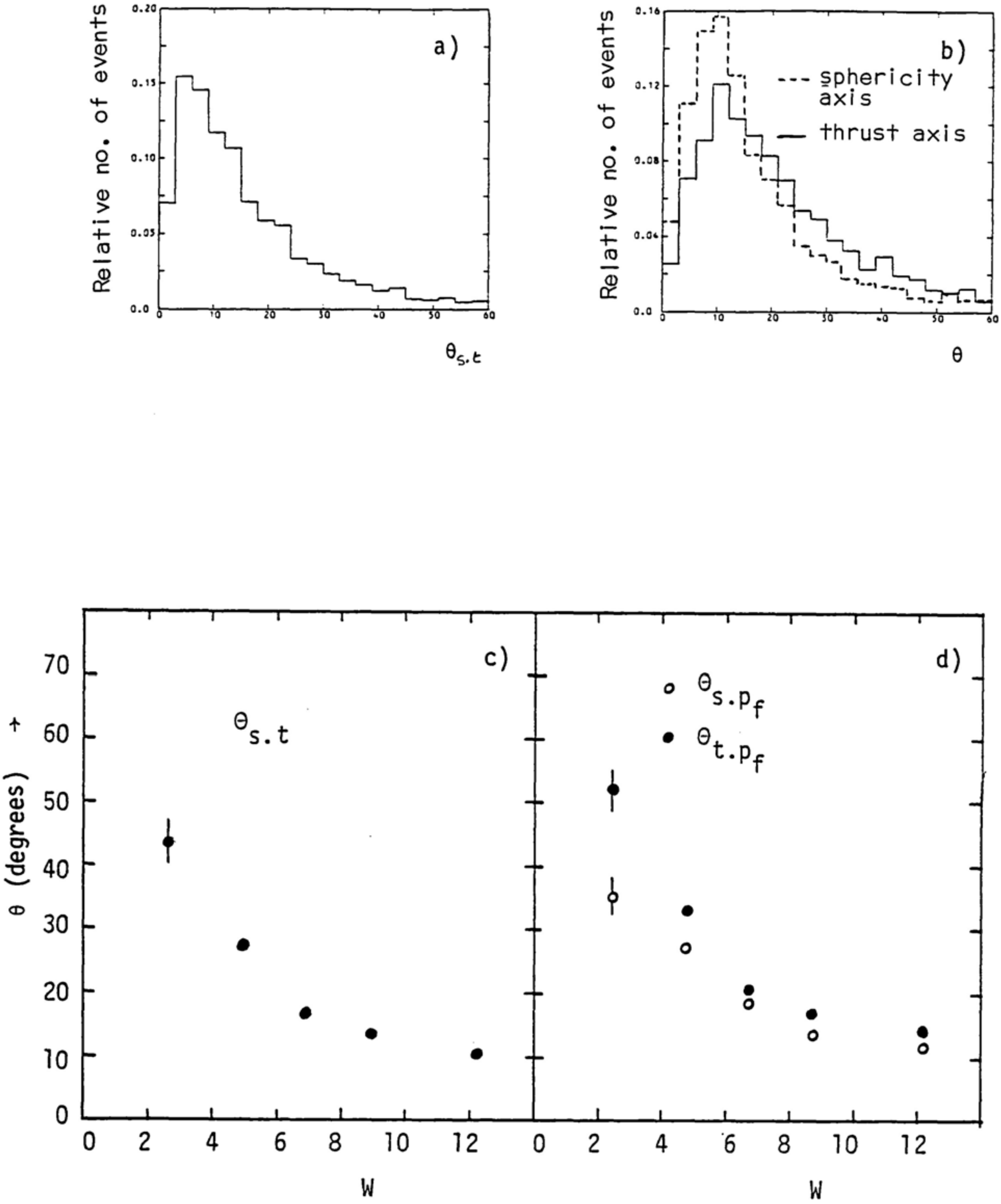

Fig 5.2 Correlation between the sphericity and thrust axis (a and c) and of the sphericity and thrust axis with the particle carrying the largest momentum (b and d) in the experimental data.

5.3 Analysis of the Data

Perturbative QCD predictions are made in terms of inclusive variables which describe the whole hadron structure, and are linear in momentum in order to avoid infrared singularities (chapter 1.5) and so hopefully the confinement problems. In such calculations all final state hadrons, charged and neutral, are summed over in order to make the predictions independent of quark and gluon fragmentation functions which are not QCD calculable. Experimentally the picture of hadron jet structure is not altered very much by the inclusion of neutral particles, mainly gammas, as shown by Fig 5.3 which shows the distribution of charged and neutral energy flow relative to the thrust axis. At large values of thrust, .85 < t <1, (see sect. 5.3.1b for definitions), which corresponds to very 2-jet like behaviour, charged energy is more peaked along the jet direction ($\theta = 0^o$) than the neutral energy, but at lower values of thrust the energy flow is very similar. In the following analysis neutral particles have been included. Results of the data analysis in terms of linear variables are first presented, followed by results obtained with variables which are not linear in momentum (and so not QCD calculable).

5.3.1a Energy Flow

As discussed in chapter 1, 'QCD jets' are defined by replacing the elementary fields of perturbative QCD (quark and gluons) by jets of hadrons. Since the non-perturbative fragmentation process causes spreading of the observed hadrons relative to the parent parton ($< p_t > \sim 300$ Mev/c) an association between the observed hadrons and the parent parton can only be made on a statistical basis.

A 2-jet event can be defined |4| by the fractional energy flow $(1 - \varepsilon)$

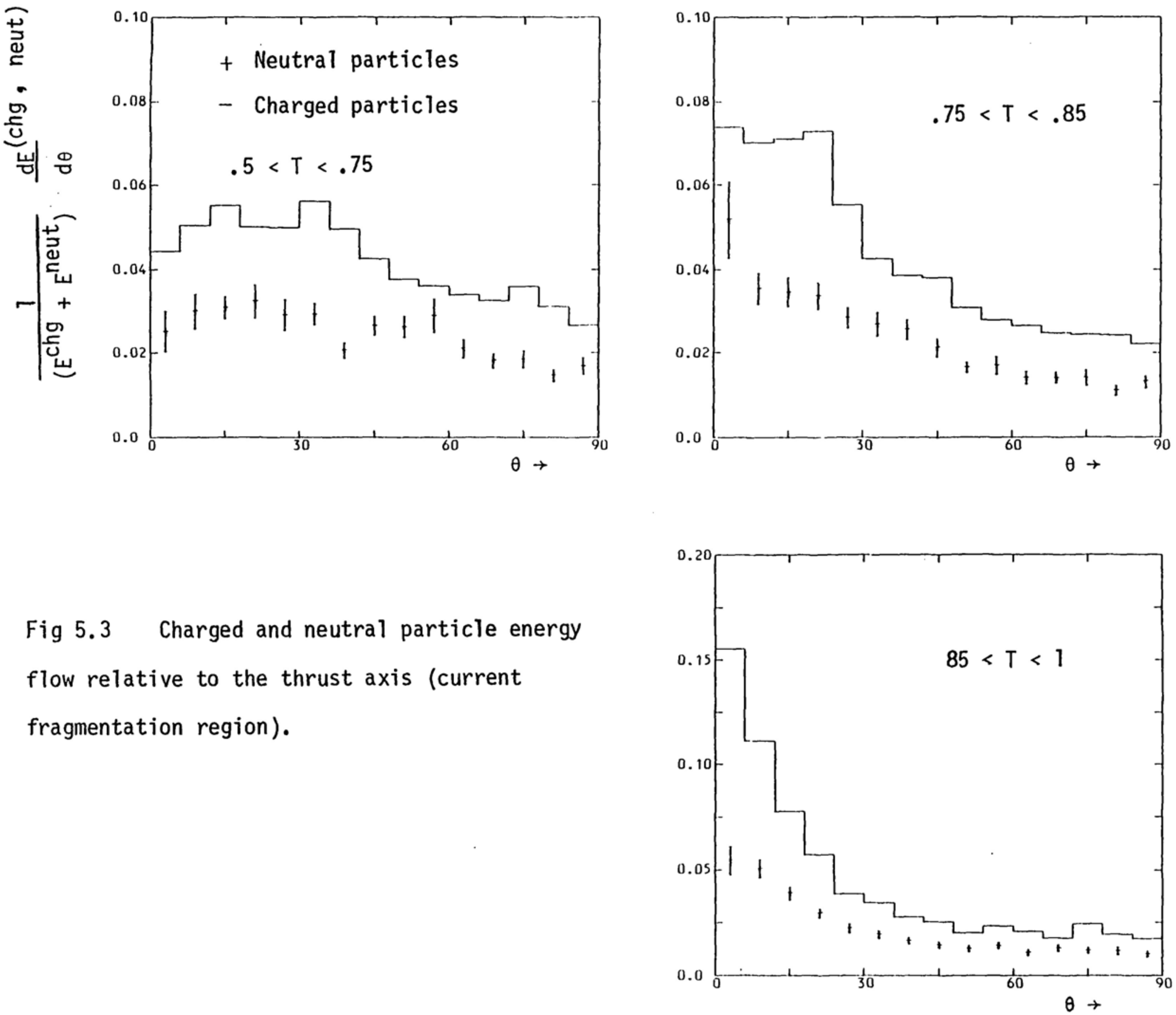

Fig 5.3 Charged and neutral particle energy flow relative to the thrust axis (current fragmentation region).

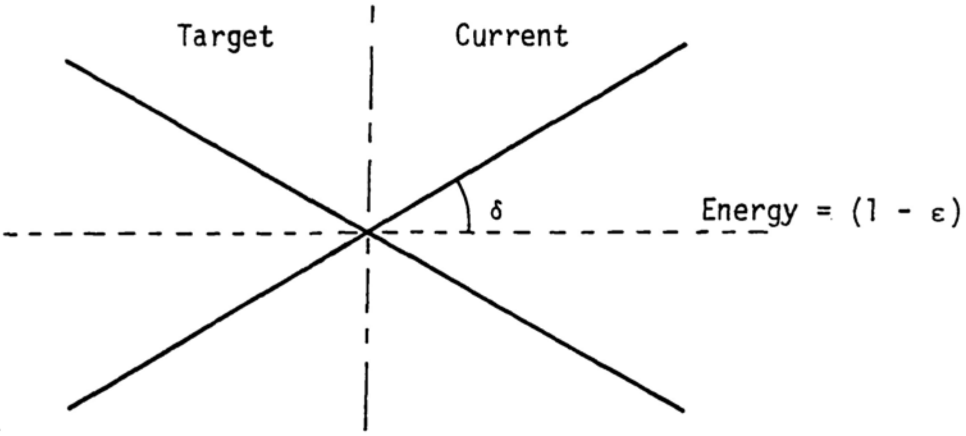

within a jet cone of half angle δ. The values of $< \varepsilon >$ as a function of the jet angle δ is shown in comparison with $e^+ e^-$ data |5| in Fig 5.3.1. The values of ε ~~is~~ are determined from the current fragments only in order to compare more directly with $e^+ e^-$, and results are shown for both the sphericity and thrust axes since the main source of error comes from determination of the axis. The neutrino data is shown for $w > 6$ Gev ($< E_{cm} > \sim 9.5$ Gev) where a well defined jet axis does exist. The results are particularly sensitive to the axis determination at small values of δ, and indicate that events are more 2-jet like in neutrino interactions than in $e^+ e^-$ annihilations.

If the fraction of 2-jet events are defined by $F(\varepsilon, \delta)$, and all other events, $(1 - F)$, are assumed to be of the 3-jet type, the fraction of 3-jet events is given by |4|:

$$1 - F(\varepsilon, \delta) = 2\alpha_s Q(\varepsilon, \delta)$$

ie

$$\frac{1}{1 - F} \sim Q'(\varepsilon, \delta) \; \ln(q^2/\Lambda^2) \tag{1}$$

where Q and Q' are constants dependent only on ε and δ. Thus equation (1) predicts that the inverse fraction of 3-jet events increases logarithmically with Q^2. The formula is expected to hold for relatively small values of δ ($\lesssim 30^\circ$) and ε ($\lesssim 0.3$).

The data shows that there is no Q^2 dependence for $\delta \lesssim 20^\circ$, Fig 5.4a b, and c. For values of $\delta \gtrsim 30^\circ$, a Q^2 dependence is observed only for $Q^2 \gtrsim 10$ (Gev/c)^2, and shows some evidence that it is stronger than the log Q^2 dependence predicted as seen from a comparison with the lines obtained from a least squares fit to the data for $Q^2 > 2$ (Gev/c)^2. The fact that no Q^2 dpendence is observed up to $Q^2 \sim 10$ (Gev/c)^2 implies that non-perturbative effects may dominate up to this energy |6|. Since no Q^2 dependence is observed at small values of δ($\lesssim 20^\circ$), even at the largest Q^2, the majority of the events must be of the 2-jet type due to the non-perturbative process.

The contribution from 3-jet (or strictly non 2-jet) events giving the observed Q^2 dependence is not explicable by the first order formula given by equation (1). This suggests that higher order terms are important, and/or that the simple picture whereby the quarks and gluons are treated as jets of hadrons is not valid at these energies, so indicating the importance of non-perturbative effects.

5.3.1b Thrust and Sphericity Distributions

The variables thrust (t) and sphericity(s) both of which are linear in momentum, are defined in the cm system of the hadrons as follows:

$$T = \frac{\max \sum_i P_{/\!/}}{\sum_i P} \qquad 0.5 < T < 1$$

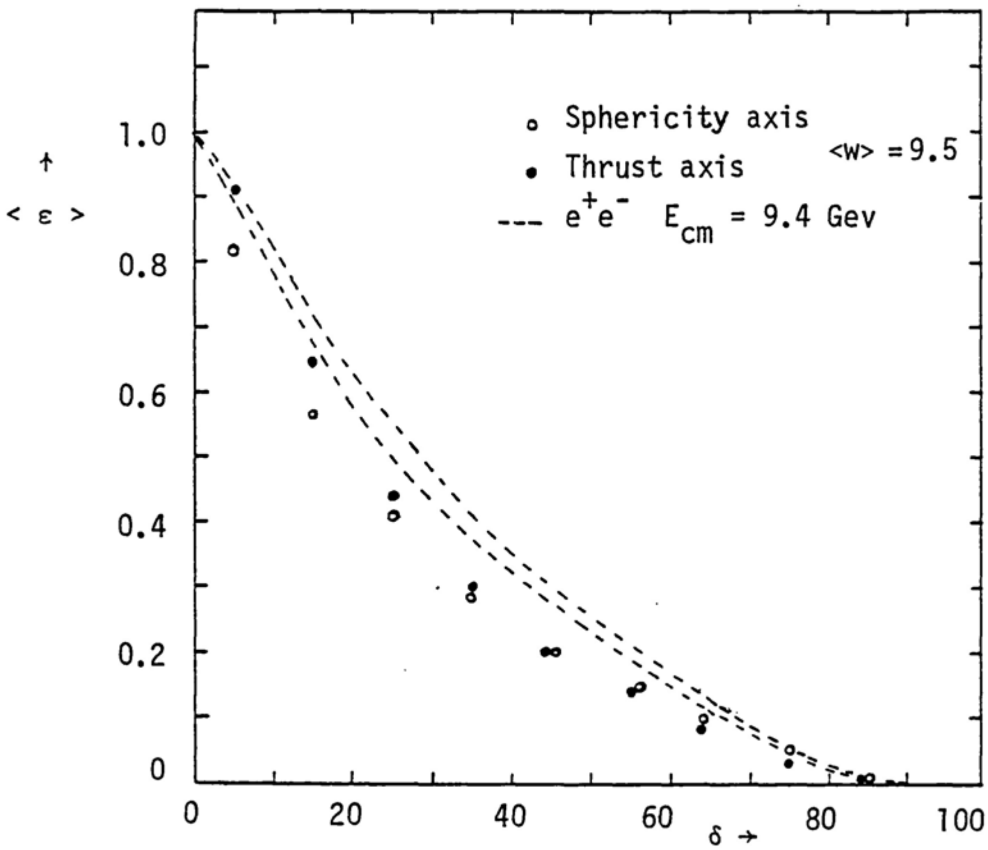

Fig 5.3.1 Mean energy outside jet cone of half angle δ.

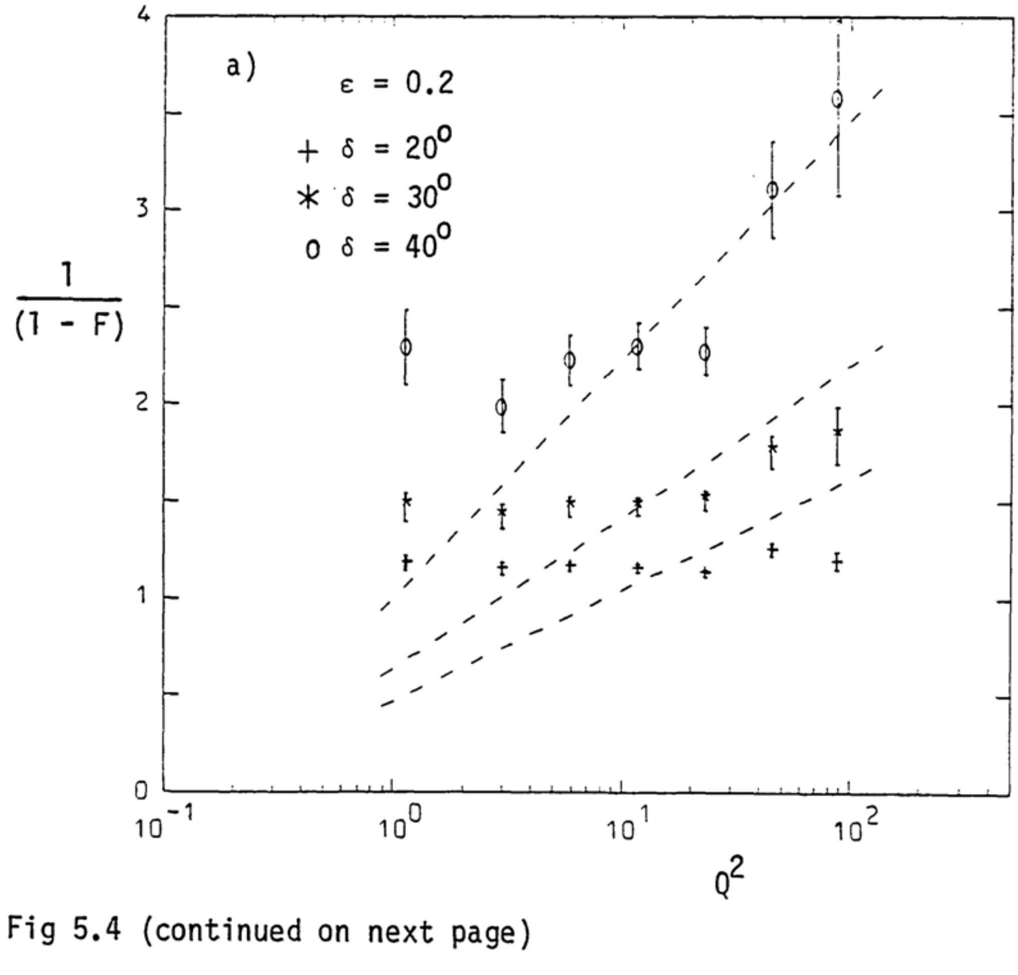

Fig 5.4 (continued on next page)

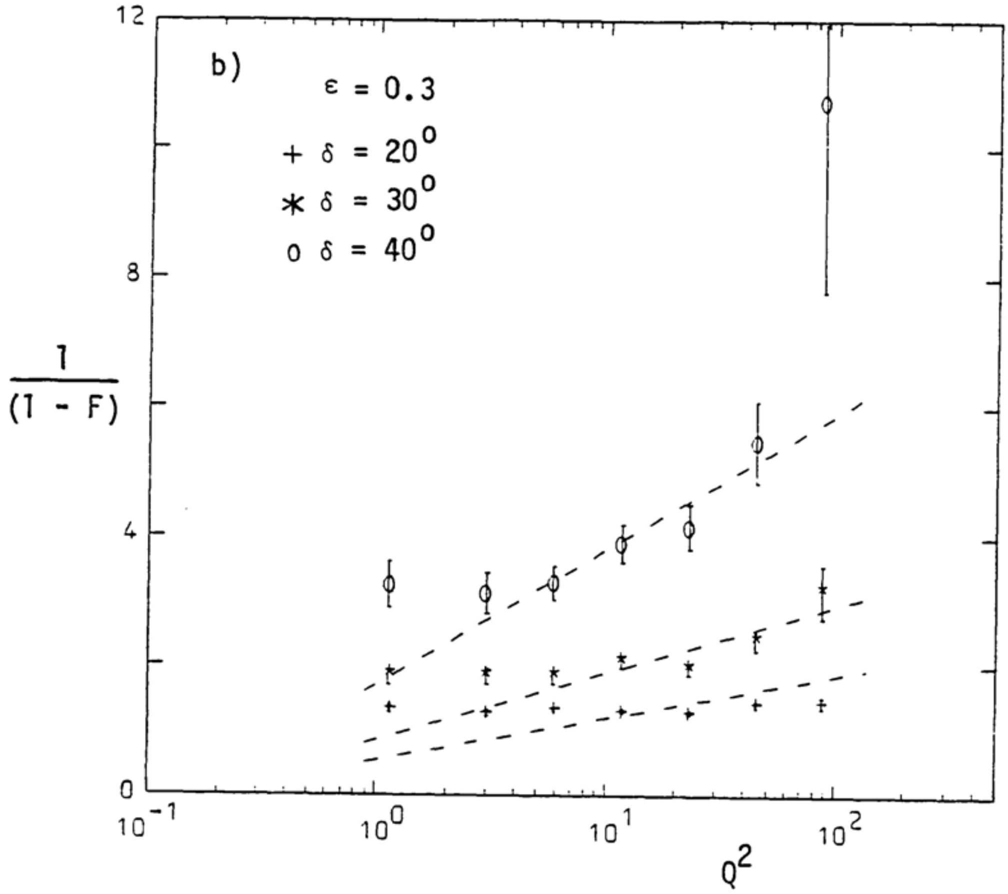

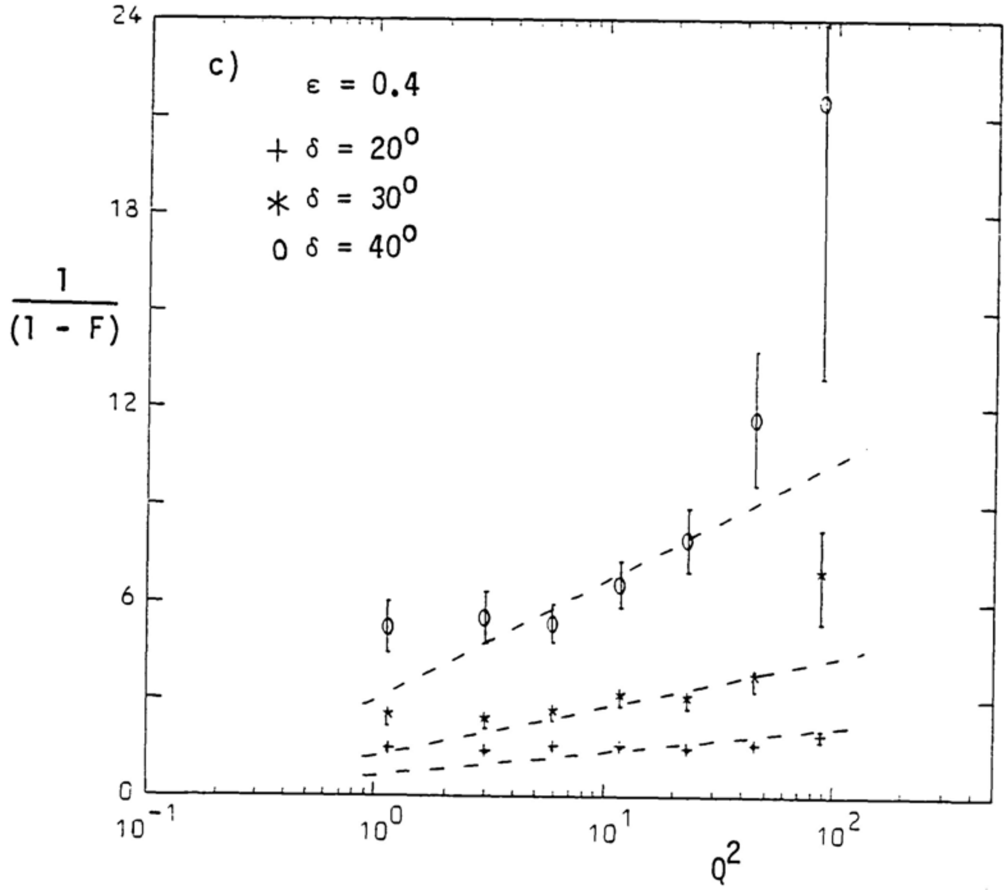

Fig 5.4 Q^2 dependence of the fraction (F) of 2-jet events.

and $$S_0 = \left(\frac{4}{\pi}\right)^2 \left(\frac{\sum_i P_t}{\sum_i P}\right)^2_{min} \qquad 0 < S_0 < 1$$

where the summation is over all particles forward in the cm system. The momentum components are measured relative to the thrust axis.

The energy dependence of $\langle S_0 \rangle$ is shown in Fig 5.5 and of $\langle 1 - T \rangle$ in Fig 5.6. Both variables give similar information about the final state hadrons, showing the increase in 2-jet behaviour as the energy increases and general similarity between the neutrino and anti-neutrino data (Fig 5.5). The distribution of $\langle S_0 \rangle$ also shows a dependence on charged multiplicity, showing a more 2-jet behaviour for lower multiplicity events compared to higher multiplicity events, at a given energy. (The $\langle 1 - T \rangle$ distribution gives a similar dependence on multiplicity). The $e^+ e^-$ annihilations data |9, 10|, excluding the $\psi\psi^*$ and Υ resonance regions, shows good agreement at low w, but indicates that events tend to be more 2-jet like in neutrino interactions at high w, especially in comparison with the results from reference 10. The 10 and 16 Gev/c K^- P data appears more 2-jet like, compared to both the neutrino and $e^+ e^-$ data. However, firm conclusions cannot be drawn from this since at such low energies the determination of the jet axis involves large errors. The 110 Gev/c K^- P data is consistent with the neutrino data.

It is clear from Fig 5.5 and 5.6 that the QCD predictions completely fail to describe the data. This, coupled to the multiplicity dependence of the variables, indicates the dominance of non-perturbative effects at these energies. The agreement with the 110 Gev/c K^- P data, which is presumably dominated by non-perturbative effects, also suggests the

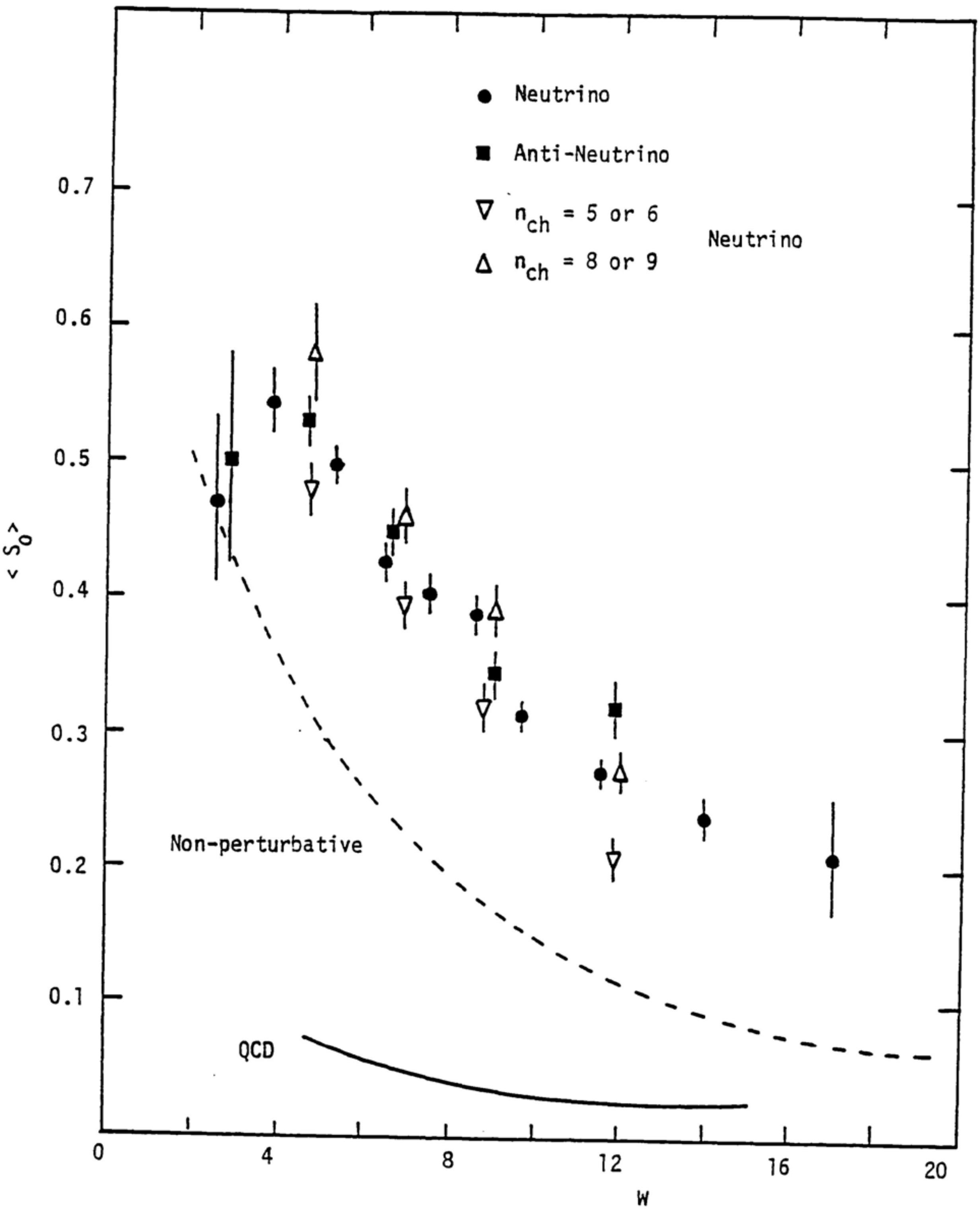

Fig 5.5 Energy dependence of the mean spherocity compared to the prediction of QCD and non-perturbative estimates.

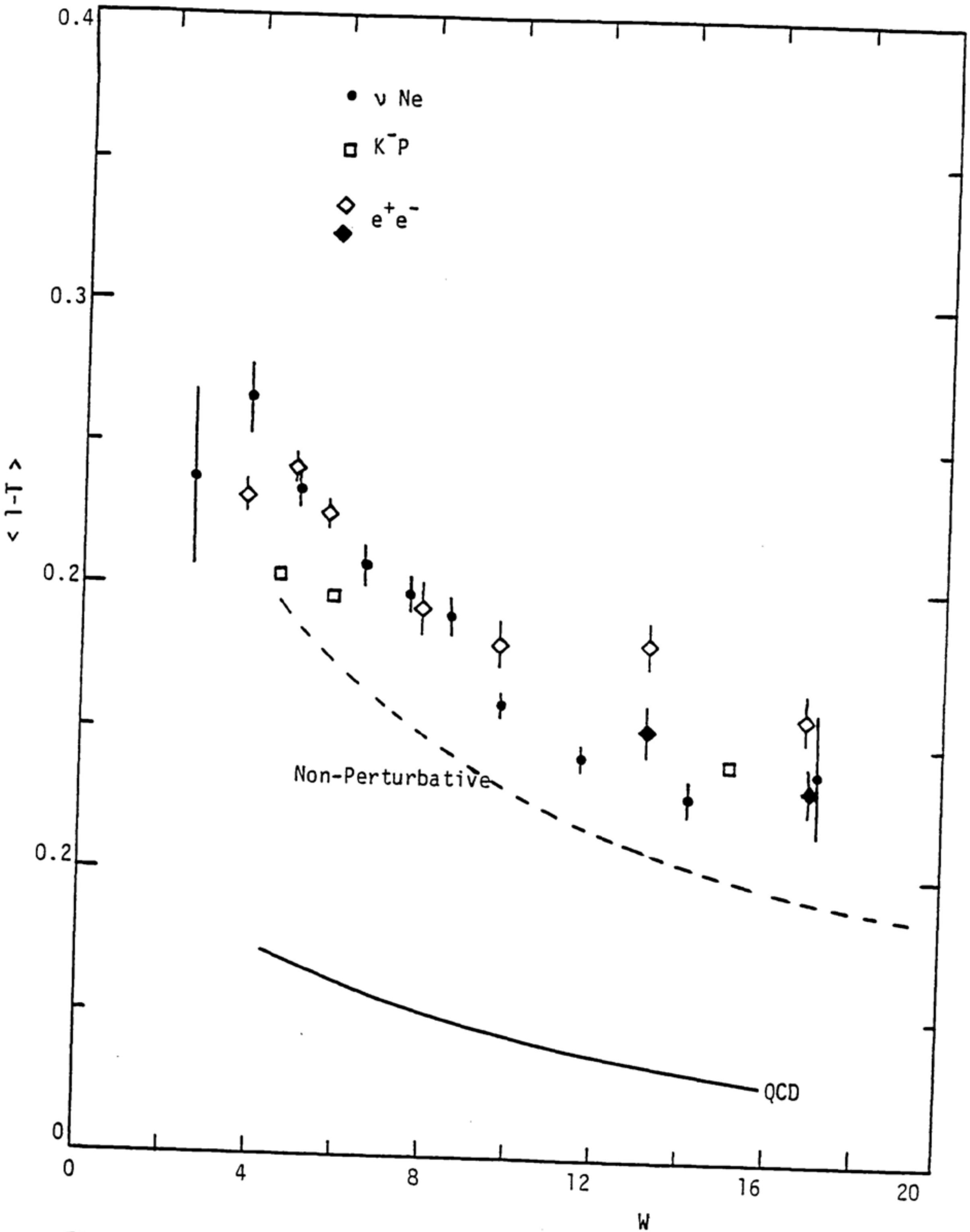

Fig 5.6 Comparison of thrust distributions in neutrino interactions with those in hadronic interactions and in annihilation processes.

dominance of non-perturbative effects. The non-perturbative estimates shown in Fig 5.5 and 5.6 illustrate the relative magnitudes of the perturbative and non-perturbative contributions to the plotted variables. The estimates are based on smearing, in transverse momentum, of the two jet perturbative results, so simulating the parton fragmentation process |7|.

The fact that perturbative QCD fails to describe the data does not necessarily imply the failure of calculations based on perturbative expansions. This is because part of the problem appears to be due to the fact that present calculations are based on 1st order expansions. The plot of fig 5.7, which shows the thrust distributions in comparison with the theoretical predictions helps to illustrate this point. The 1st order prediction fails to describe the data even after non-perturbative smearing of the perturbative results. However, summing the 'leading logs' in the QCD expansions of the thrust distributions |11| improves the agreement with the data quite substantially. The inadequacy of the 1st order calculations is also illustrated by the fact that the QCD predictions in thrust and spherocity distributions for $e^+ e^-$ are practically twice as large as the corresponding predictions for neutrino interactions. In the calculation where leading logs are also summed however the predictions are the same for both processes, as may be expected on the basis of the similarity of the experimental distributions in the energy range of the predictions ($w \sim 12$ Gev).

5.3.2 Distributions in Quadratic Variables

The normalised eigenvalues of the sphericity tensor (section 5.2) can be represented on a Dalitz plot as shown in Fig 5.8a. The event distribution, which is bounded by the inner triangle, is shown in Fig 5.8b.

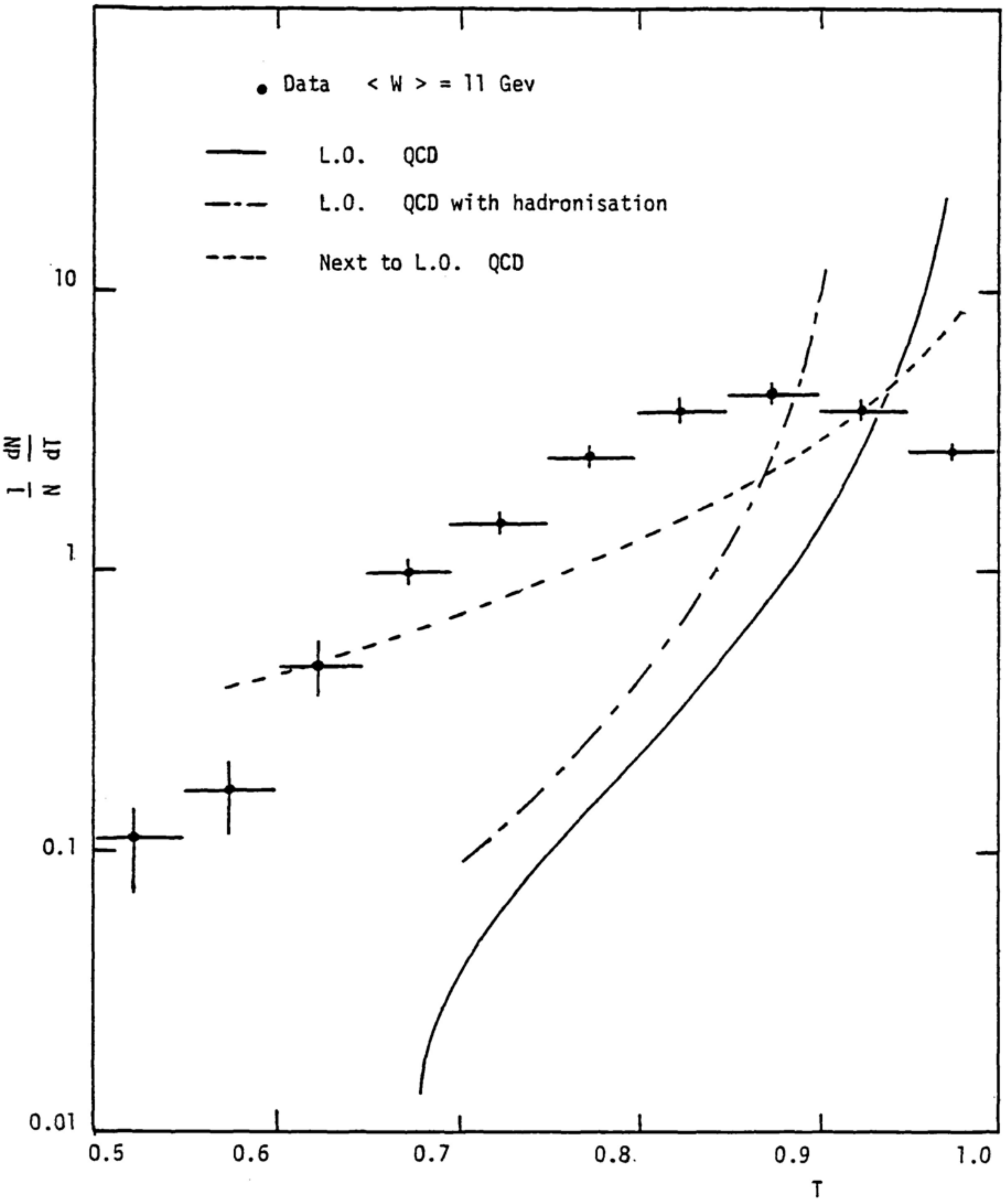

Fig 5.7 Comparison of the thrust distribution with that predicted by QCD. (L.O. is the lowest order, leading log, calculation. In the Next to L.O. prediction leading logs are summed).

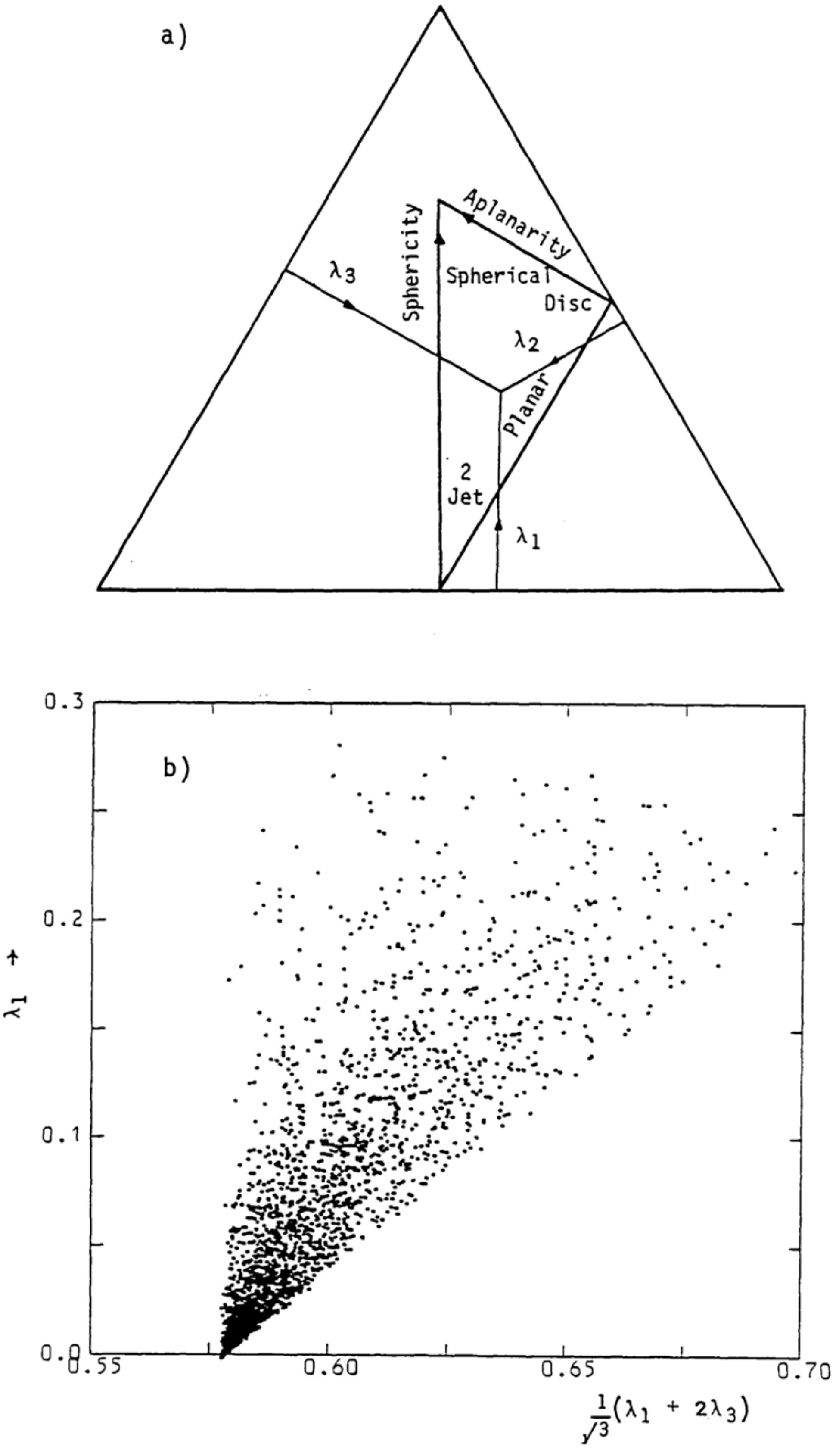

Fig 5.8 a) Dalitz plot showing the regions occupied by various types of (jet) events within the allowed region (inner triangle), and b) the distribution of events in the allowed region.

Using these eigenvalues various variables which describe the momentum structure of the hadrons can be constructed. The sphericity |1| is given by:

$$S = 3\lambda_1$$

$$= \frac{3}{2} \min \frac{\sum_i p_t^2}{\sum_i p^2} \qquad 0 < S < 1$$

and aplanarity by:

$$A = \frac{3}{2}(1 - \lambda_3)$$

$$= \frac{3}{2} \min \frac{\sum_i p^2_{/\!/ \, out}}{\sum_i p^2} \qquad 0 < A < 0.5$$

where $p_{/\!/ out}$ is the hadron momentum out of the minimum p_t^2 plane (event plane) defined by the eigenvectors corresponding to the eigenvalues λ_1 and λ_2. The summation is over all particles.

The value of $S \rightarrow 0$ corresponds to a 2-jet event structure, $S \rightarrow 1$ and A large to spherical events, and $A \rightarrow 0$ and S large to planar or disc like events. The various regions are shown in Fig 5.8a, and the plot of Fig 5.8b indicates that the majority of the events correspond to the 2-jet type with a few of the planar type.

The energy dependence of <A> and <S> is shown in Fig 5.9. Both decrease with w indicating a trend towards more 2-jet like behaviour

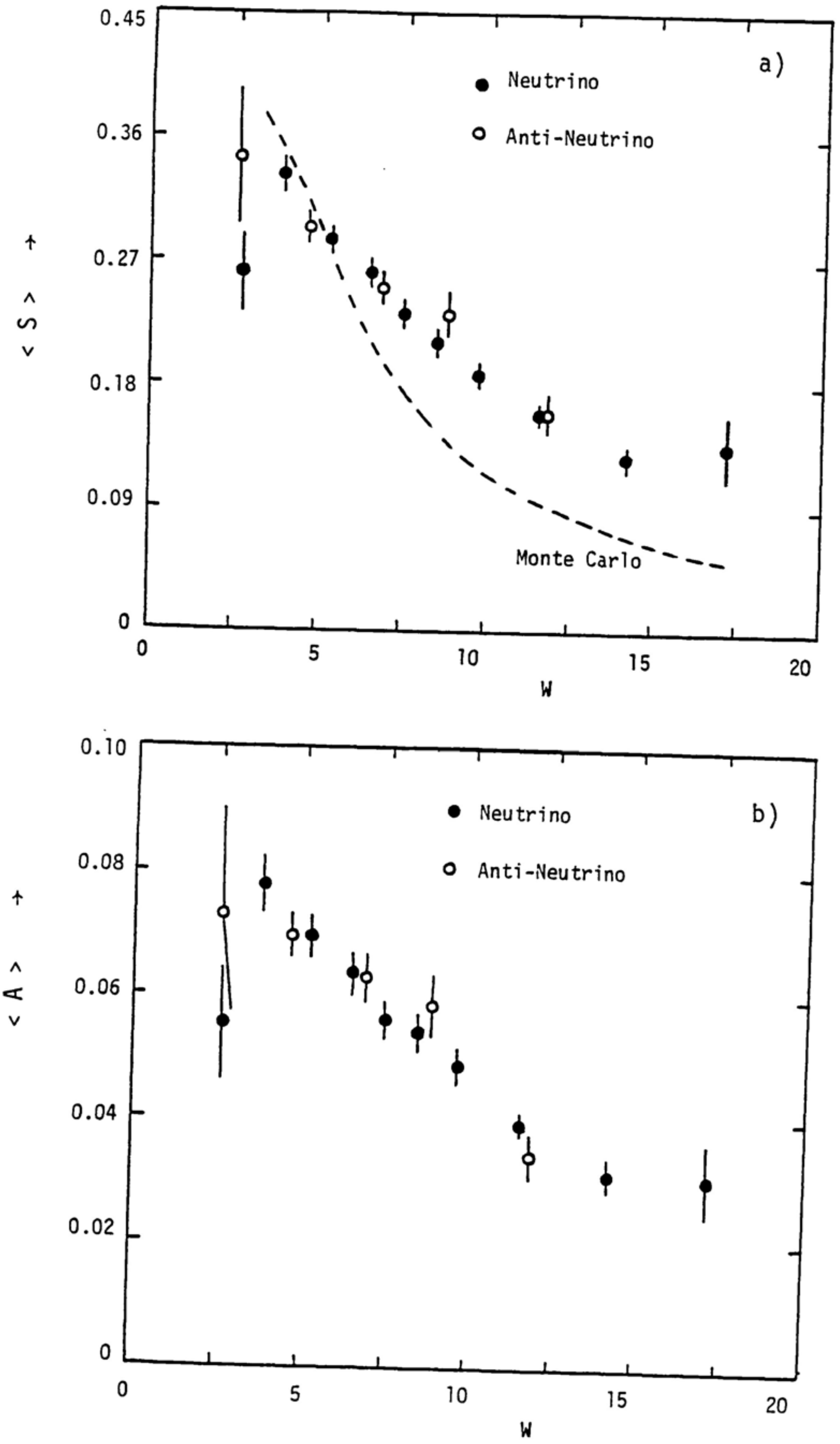

Fig 5.9 Energy dependence of mean sphericity and mean aplanarity.

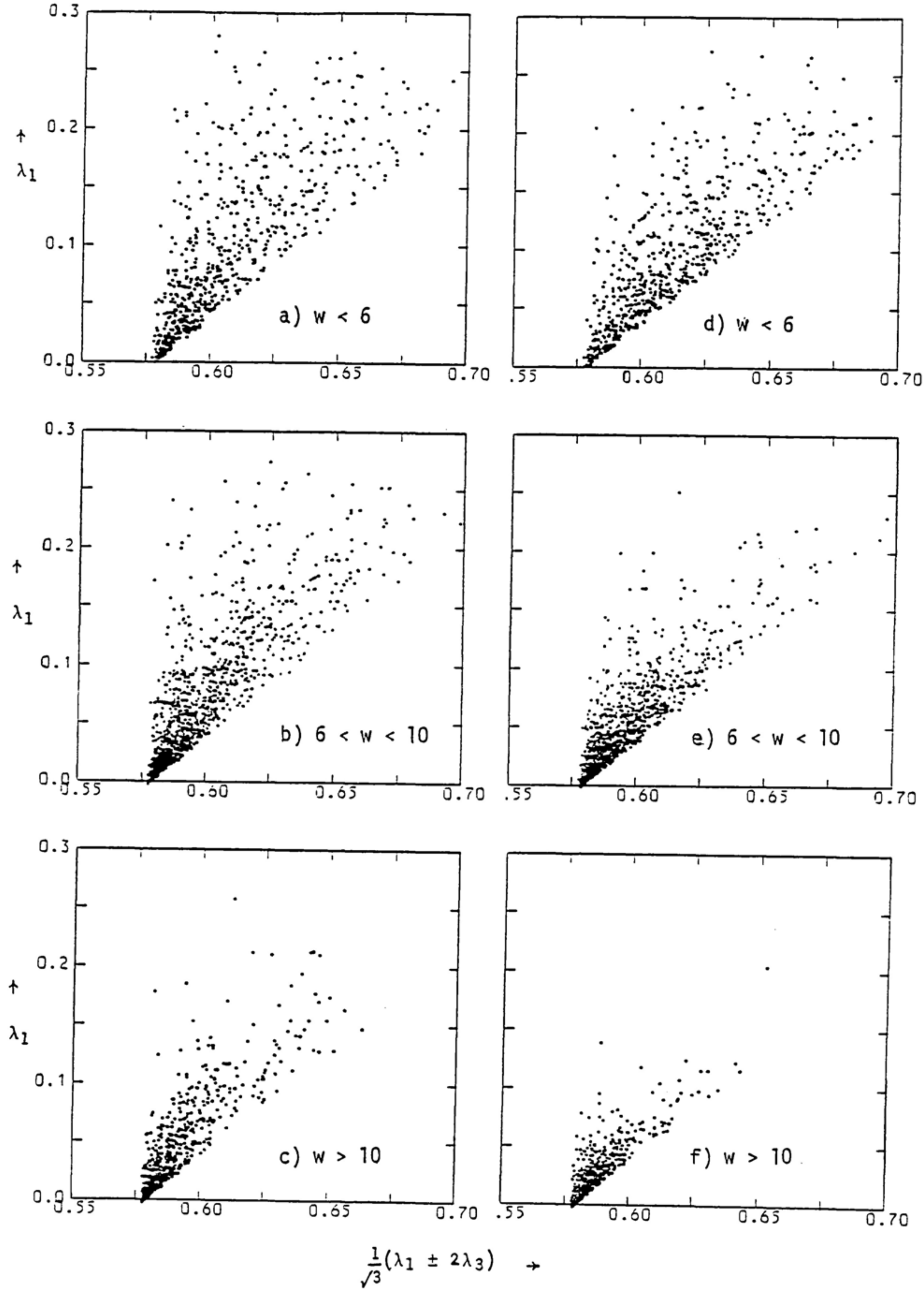

Fig 5.10 Distribution of eigenvalues for the data (a,b,c) and Monte Carlo (d,e,f) at various energies.

with an increasing amount of the hadron momentum being confined to the event plane as the energy increases. Also shown is the anti-neutrino data, which shows a very similar event structure. The results of the Monte Carlo indicate that the data cannot be explained by a 2-jet Monte Carlo with events at high energy giving a higher < s > than predicted by the Monte Carlo.

The distribution of eigenvalues is shown in comparison with the results of the 2-jet Monte Carlo in bins of w in Fig 5.10. The trend towards 2-jet like behaviour as the energy increases, which was shown in Fig 5.9a, is observed to affect the planar region much more in the Monte Carlo data than in the experimental data. Thus the relative proportion of planar events in the data increases in comparison with those in the Monte Carlo.

In order to investigate this trend in detail, the distribution of events in aplanarity and sphericity is given in table 5.2, in various bins of w. Planar events are defined here to be those for which $S > 0.25$ and $A < 0.1$ (the definition $A < 0.04$ has been used in reference 12, however in order to obtain a statistically significant event sample a looser cut on A has been applied here); and 2-jet events as those for which $S < 0.25$. The planar events as a fraction (F) of the sum of planar and 2-jet events obtained from table 5.2 are given in table 5.1.

F W(Gev)	Data	Monte Carlo
<6	0.47 ± 0.023	0.58 ± 0.031
6-10	0.35 ± 0.013	0.27 ± 0.014
>10	0.22 ± 0.018	0.06 ± 0.00

Table 5.1 ($A < 0.1$ and $S > 0.25$)

W < 6

S A	0 - 0.25	0.25 - 0.5	0.5 - 0.75	0.75 - 1.0
0 - 0.1	242 (210)	148 (210)	56 (68)	9 (17)
0.1 - 0.2		31 (32)	68 (48)	26 (16)
0.2 - 0.3			8 (5)	26 (16)
0.3 - 0.4				4 (1)

6 < W < 10

S A	0 - 0.25	0.25 - 0.5	0.5 - 0.75	0.75 - 1.0
0 - 0.1	556 (714)	237 (225)	55 (33)	10 (4)
0.1 - 0.2		56 (25)	69 (16)	16 (6)
0.2 - 0.3			7 (2)	19 (3)
0.3 - 0.4				3 (0)

W > 10

S A	0 - 0.25	0.25 - 0.5	0.5 - 0.75	0.75 - 1.0
0 - 0.1	447 (562)	110 (41)	16 (0)	1 (0)
0.1 - 0.2		16 (4)	11 (1)	4 (1)
0.2 - 0.3			2 (0)	1 (0)
0.3 - 0.4				1 (0)

Table 5.2 Distribution of events in sphericity and aplanarity. Monte Carlo predicted events are given in brackets.

This shows that the fraction of planar events produced in the data is approximately predicted by the Monte Carlo at low values of w, but at large w there are ∿ 4 times the fraction of planar events predicted. An excess of such events has also been observed in $e^+ e^-$ annihilations |12| and interpreted as evidence of hard gluon Bremsstrahlung. The possibility of such an origin for these events has been checked by looking for an enhancement in the $\langle\cos\phi\rangle$ and $\langle\cos 2\phi\rangle$ asymmetry presented in chapter 3.

An asymmetry in these variables would be expected due to corellations of the spin of the gluon and the lepton plane, giving hard gluon emission preferentially in the direction of the outgoing muon. The values $\langle\cos\phi\rangle$ and $\langle\cos 2\phi\rangle$ obtained are given in table 5.3 and show no asymmetry in these variables.

$\langle Q^2\rangle$	$\langle\cos\phi\rangle$	$\langle\cos 2\phi\rangle$
3	.001 ± .037	.020 ± .034
18	.007 ± .021	.021 ± .021
74	.035 ± .074	.006 ± .073

Table 5.3 (A < 0.1 and S > 0.25)

Alternatively the hard gluon emission interpretation has been checked by studying the energy dependence of $\langle p_t^2\rangle_{in}$ and $\langle p_t^2\rangle_{out}$ defined by:

$$p_{t_{in}}^2 = \sum_i (\underline{p} \cdot \underline{k}_2)^2$$

$$p_{t\,\text{out}}^{2} = \sum_i (\underline{p} \cdot \underline{k}_3)^2$$

where k_2 and k_3 are unit vectors in the direction of the axis corresponding to the eigenvalues λ_2 and λ_3.

The data (Fig 5.11a) shows a practically linear rise in $<p_t^2>_{in}$ and $<p_t^2>_{out}$ with w. The rate of increase in $<p_t^2>_{in}$ is in agreement with that in the e^+e^- data from PLUTO |9|, but the rate of increase in $<p_t^2>_{out}$ is faster than in the $e^+ e^-$ data. The ratio,

$$R = \frac{<p_t^2>_{in}}{<p_t^2>_{out}}$$

shows a decrease at low w, (Fig 5.11b) but shows a steady increase for w > 6 Gev. This trend is consistent with that observed in the $e^+ e^-$ data. However the absolute value of R is a bit larger in the neutrino data so that there is a discontinuity in the value of R in making the transition from the neutrino to the $e^+ e^-$ data at w $\sim$ 12 Gev.

For the cuts to isolate planar events, S > 0.25 and A < 0.1, the value is consistant with no dependence on w over its entire range. However if the low w region (w < 6 Gev) is omitted, since at these energies well defined jets of hadrons do not exist (section 5.2), the value of R shows an increase with increasing w. The decrease in R observed at low w is a kinematical feature which is due to the effects of low event multiplicities, and is reproduced by the Monte Carlo.

The absence of any asymmetry in the $<\cos\phi>$ and $<\cos 2\phi>$, and of any strong indication of an increase in $<p_t^2>_{in}/<p_t^2>_{out}$ in the planar event region excludes the possibility of a major contribution from

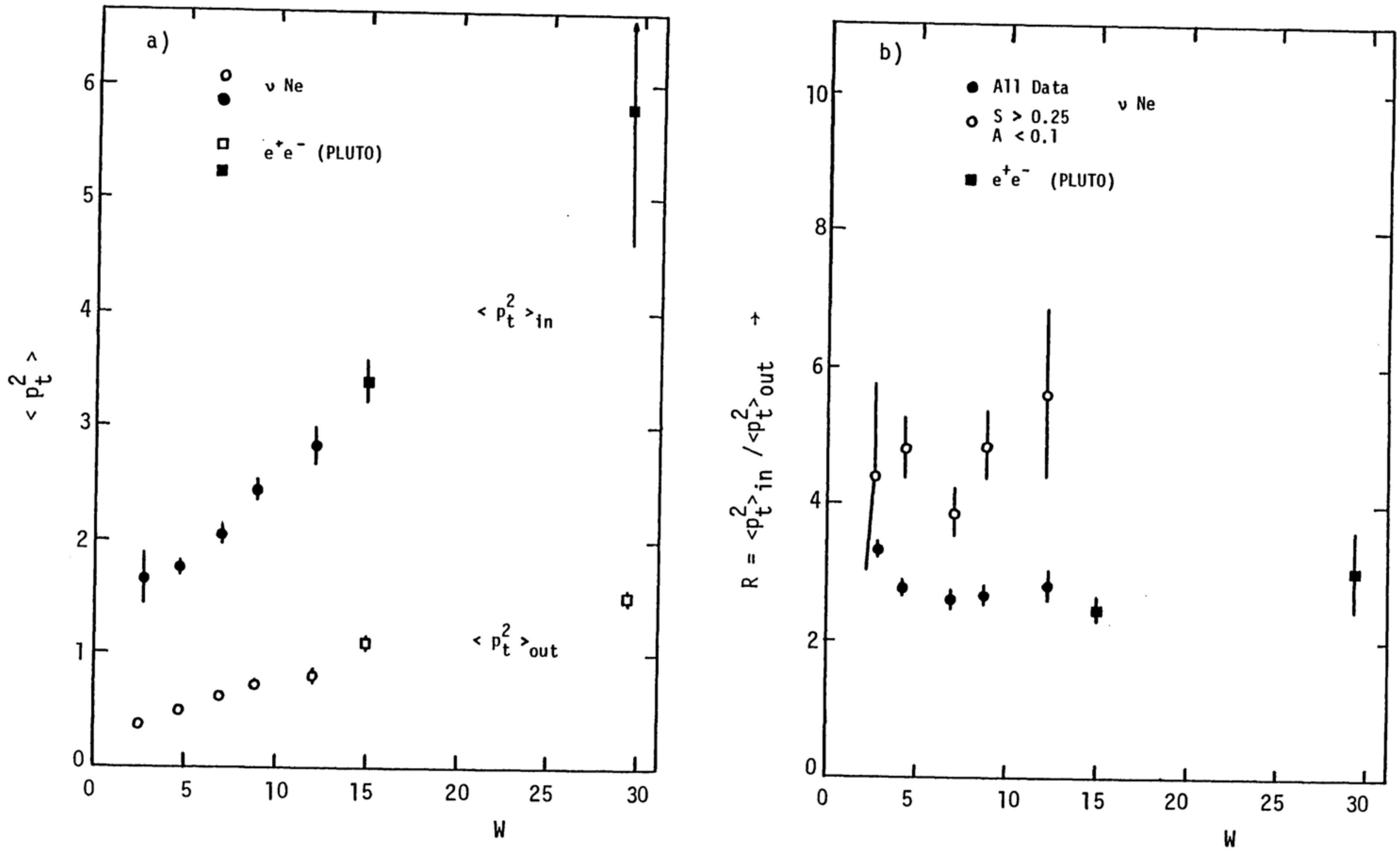

Fig 5.11 a) Energy dependence of the transverse momentum in and out of the event plane, and b) of their ratio

events where a hard, non-collinear, gluon is emitted. However the observed increase in $<p_t^2>_{in}$ and $<p_t^2>_{out}$ with energy could, assuming it is not due to the quark hadronisation process, be explained by soft gluon emission processes.

5.4 Pointing Vector

The quantities, $<s>$, $<1 - t>$, $<s_0>$, studied so far carry minimal information on the nature of the multijet final state hadrons since they are averaged quantities. The 'pointing vector' |10| defined by:

$$p(\phi) = \frac{2}{w} p_i \frac{d\sigma}{d\phi}$$

where ϕ is an azimuthal angle in or out of the event plane (Fig 5.12); in contrast potentially carries much more information. In order to separate the non 2-jet contribution in $e^+ e^-$ events it has been suggested |10| to plot the pointing vector by dividing the event into a forward and backward half by a plane perpendicular to the jet axis; the forward region being chosen as the one with the largest sum of p_t of the hadrons relative to the jet axis. The forward region is then divided into a left and a right quadrant, with the event being rotated such that the quadrant containing the largest momentum always lies on the same side.

Such a procedure has been found, on the basis of Monte Carlo studies, to induce considerable bias. In order to avoid such bias, use has been made of the known current direction in neutrino experiments, and the forward region chosen such that it always lies along the hadronic axis. Evidence of gluon emission should then show up as a dip in the pointing vector in the region $\phi_{in} = 0$ and $\phi_{out} = 0$; and a general broadening in the forward momentum flow.

The pointing vector defined in and out of the event plane

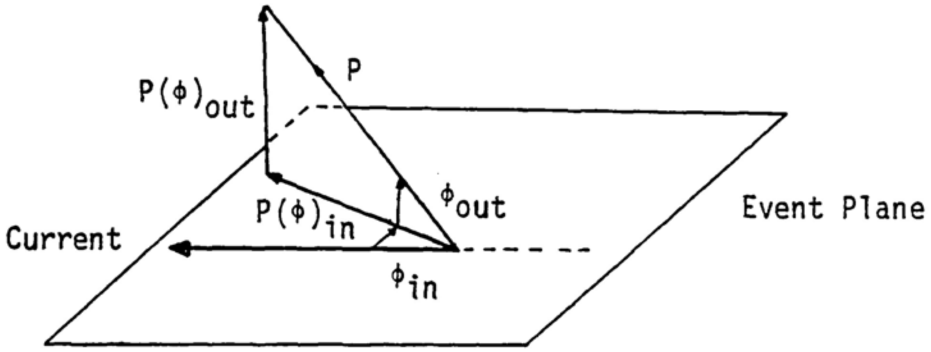

Fig 5.12

by $p(\phi_{in})$ and $p(\phi_{out})$ is shown in Fig 5.13. The very 2-jet like nature of the total data sample, for $w > 6$ Gev, is observed. For the selection $s > .25$, $A < .04$, no large differences are seen between the forward and backward region, with both distributions tending to broaden equally in the event plane as a result of the cuts. This again indicates that contributions to planar events from events containing hard gluon emission is very small, even for the tighter cut on aplanarity ($A < 0.04$) used in reference 12.

Conclusions

The momentum space structure of hadrons produced in neutrino interactions is similar to that of hadrons produced in $e^+ e^-$ annihilations at low energies, but show a trend towards more 2-jet like behaviour at higher energies. There is agreement with 110 Gev/c k^-p interactions data.

Perturbative QCD calculations fail to describe the observed hadron distributions, at the present level of calculation, and there is no evidence of hard gluon emission in the planar events. The observation of an increase in $\langle p_t^2 \rangle_{in}$ and $\langle p_t^2 \rangle_{out}$ with energy is however consistent with emission of soft gluons.

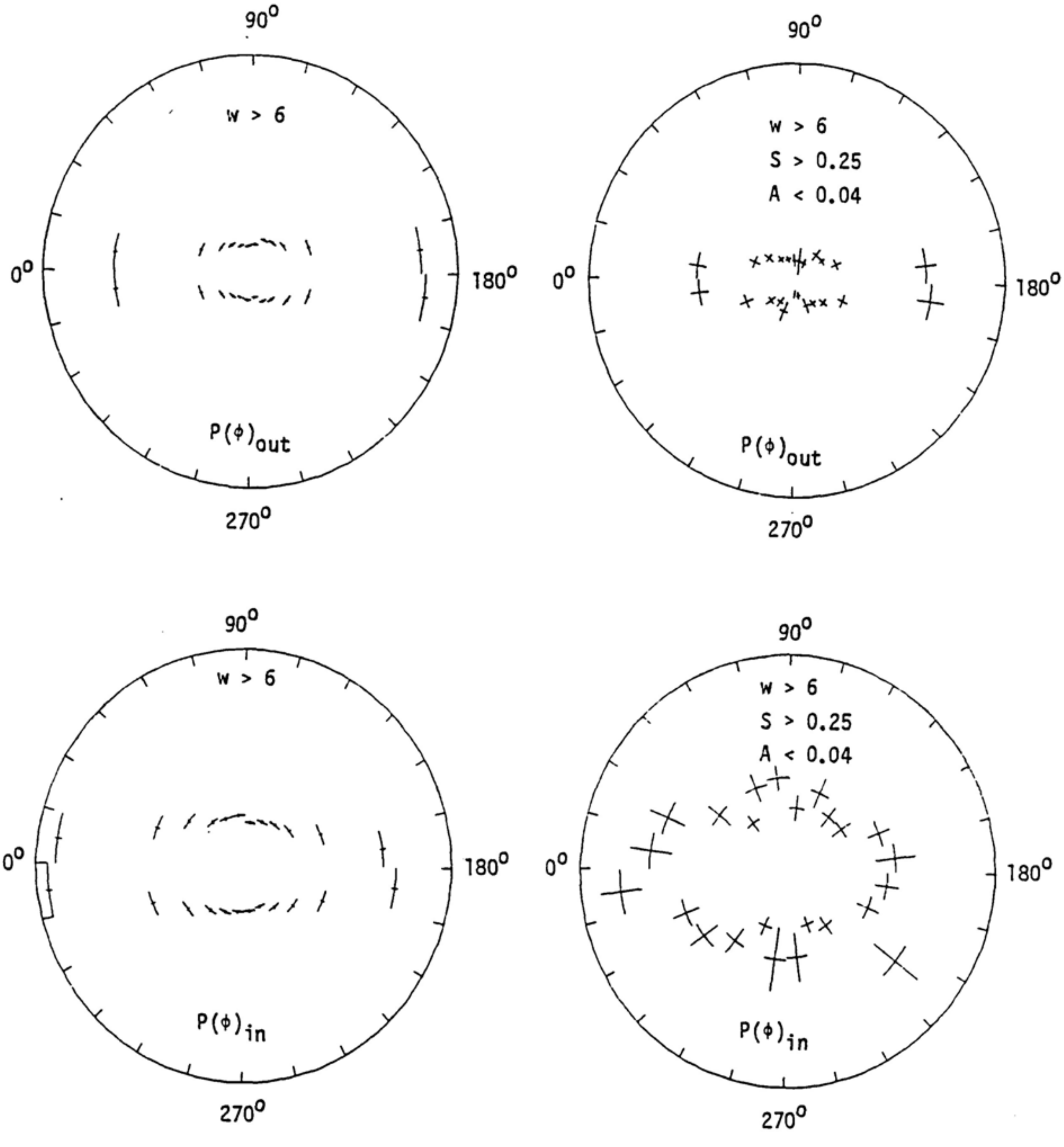

Fig 5.13 Momentum Flow in and out of the event plane for all events ($w > 6$) and for planar events. (The scale radially out from the centre of the plots extends from 0 to 0.075).

References

1 G Hanson et al, Phys. Rev. Lett. Vol. 35 no. 24 (1975) 1609

2 S Brandt and D H Dahman, Particles and Fields 1 (1979) 61-70

3 B H Wiik, Results from PETRA, DESY 79/84

4 G Sterman and S Weinberg, Phys. Rev. Lett. Vol. 39 no. 23
P Binutary and G Girardi, Ref. TH 2617-CERN

5 Ch Berger et al, PLUTO Collaboration at DORIS, Phys. Lett. 78B no. 1

6 H D Politzer, CALT 68-789

7 P Binutary and G Girardi, Ref. TH 2611-CERN

8 K W J Barnham et al, Imperial College Physics Note IC/HENP/79/27, submitted to Nucl. Phys. B

9 Ch Berger et al, PLUTO Collaboration at PETRA, Phys. Lett. 81B (1979) 410

10 R Brandelick et al, TASSO Collaboration, Phys. Rev. Lett. 83B (1979) 261

11 P Binutary and G Girardi, Ref. TH 2807-CERN

12 Ch Berger et al, PLUTO Collaboration, Phys. Lett. Vol. 86B no. 3,4

13 A De Rujula, J Ellis, E G Floratos, and M K Gailliard, Nucl. Phys. B138 (1978) 387

CHAPTER 6

Fragmentation Functions

6.1 Introduction

In this section the fragmentation functions of positive and negative hadrons are studied. The analysis is presented, mainly through the study of the moments of these functions and their non-singlet combination, so that a comparison with the predictions of QCD can be made.

The m'th moment of the fragmentation function $D^h_{q_i}(z,q^2)$, which is the probability distribution for a quark q_i produced at momentum squared, q^2, to decay into a hadron h with a fraction z of the quark momentum is defined by:

$$D_m(q^2) = \int_0^1 z^{m-1} D^h_q (z,q^2)\, dz \tag{1}$$

QCD predicts the q^2 dependence of the m'th moment (appendix 1):

$$D_m(q^2) = \frac{c_m}{[\ln(q^2/\Lambda^2)]^{d_m}} \tag{2}$$

where d_m are the non-singlet anomalous dimensions and the constants c_m are q^2 independent.

Theoretically such predictions of non-scaling were first made for the structure functions, and already inclusive lepton scattering data |1|, show deviations from Bjorken scaling and the moments of the structure functions F_2 and xF_3, for which definite qualitative QCD predictions given by equation (2) exist, seem to be in good agreement with leading order QCD.

The scaling violations observed in the study of structure functions are shown to be observable in the final state hadrons. It is also shown that the single particle inclusive cross-section does not factorise into the simple form predicted by the quark-parton model, and the size of the non-factorizable part compared with the predictions of QCD.

6.2 Factorisation and Scaling

In the naive parton model picture |2|, the production of secondary hadrons is assumed to take place in a two step process (Fig 6.1):

i) Exchange boson interacts with target quark

ii) Scattered quark fragments into observed hadrons (current fragmentation).

and the cross-section has the form:

$$\frac{d\sigma}{dx\, dz} \propto xQ(x)\, D_q^h\,(z) \qquad (3)$$

where x is the Bjorken variable and:

$$z = \frac{2h.q}{q^2}\,, \quad D_q^h(z) = \frac{1}{N_{event}}\,\frac{dN^h}{dz}$$

$xQ(x,q^2)$ describes the distribution of the quark in the target hadron, and the fragmentation function $D_q^h(z)$ describes the distribution of hadrons in the struck quark: it gives the probability of a quark of flavour q to fragment giving a hadron h with fraction z of its momentum.

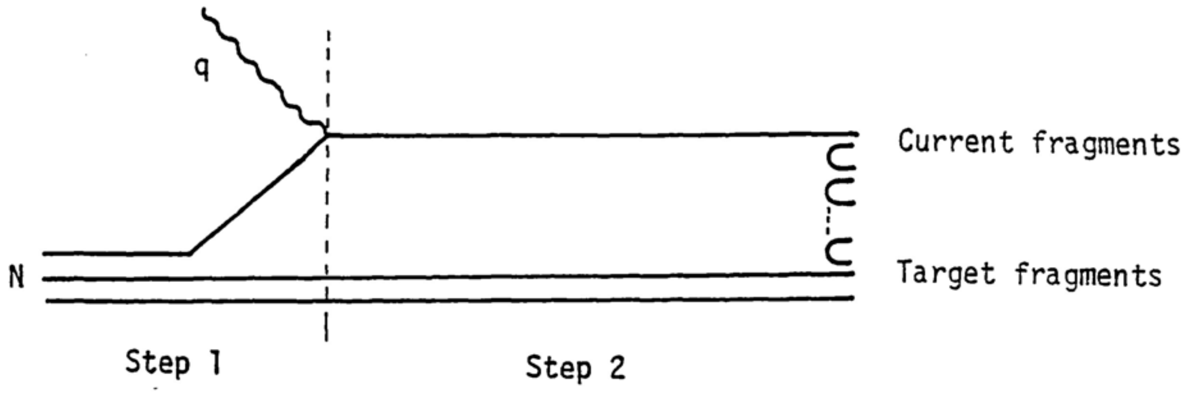

Fig 6.1

Thus in the naive parton model (assuming a single quark flavour is involved in the scattering of the boson, ie neglecting the Cabbibo suppressed sea quark contribution $\bar{u} \rightarrow \bar{s}$ and $s \rightarrow u$), the cross-section is assumed to factorise into a product of a quark distribution function depending only on x and a hadron fragmentation function depending only on z. (The contribution from $\bar{u} \rightarrow \bar{d}$ should not disturb factorisation since most secondary hadrons are pions for which $D_{\bar{d}}^{\pi^{\pm}} = D_{\bar{u}}^{\pi^{\pm}}$).

More generally the quark distribution function and the fragmentation function may also depend on q^2, non-scaling |1|, and the fragmentation function may additionally depend on x, non-factorisation, so that the inclusive cross-section to produce a hadron with energy fraction z is then given by:

$$\frac{d\sigma}{dx\,dz} = \frac{G^2ME}{\pi} F(x,q^2)\, D_q^h\,(z,x,q^2)^{\dagger} \qquad (4)$$

where now $D_q^h = \frac{1}{N_{ev}(q^2)} \frac{dN^h}{dx\,dz\,dq^2}$

Such a q^2 dependence of the functions is predicted in 1st order perturbative QCD, equation (2), due to gluon Bremsstrahlung. Factorisation still holds to leading order QCD, although in the next to leading order violation of factorisation is expected |8|.

6.3 Variables and Frames

In order to study the fragmentation function of a particular type of quark, the hadrons resulting from the fragmentation process need to be separated. The separation can potentially be carried out in the lab frame, $z_{lab} > 0.2$, the centre of mass frame, $x_f > 0$, or the Breit frame, $z_b > 0$. The Breit frame is defined as the system in which zero energy is transferred between the current and target quark, with the transformation from lab to Breit frame being obtained by a boost given by:

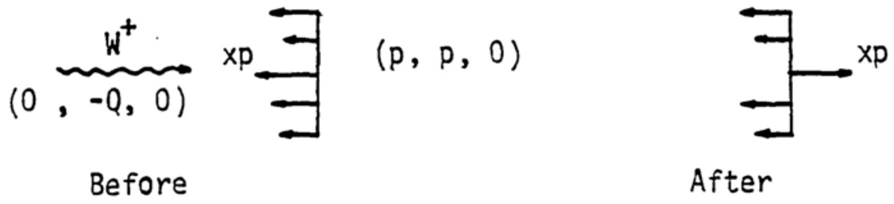

Fig. Collision in the Breit frame

---

† More precisely the cross-section can be written as the sum of three structure functions each multiplied by y-dependent factors (chapter 1). In equation (4) the y-dependence has been integrated over with the simplifying assumption that all three structure functions are equal ($F_2 = 2xF_1 = xF_3$); ie assuming a flat y distribution which is obeyed by the data |1|.

$$\eta = \frac{p}{m} = \frac{-Q}{2pm} \qquad m = \text{nucleon mass}$$

where $2xp = -Q =$ change in parton momentum in the Breit system.

The possibility of using any of these frames leads to several longitudinal variables which may be used to define the fragmentation functions:

i) $$z_{lab} = \frac{E_{lab}}{E^h_{lab}} = \frac{E_{lab}}{\nu + m}$$

or $$z'_{lab} = \frac{p.h}{p.q} = \frac{E_{lab}}{\nu} = \frac{z_{lab}}{\left(1 + \frac{2m^2x}{q^2}\right)} \sim z_{lab} \text{ for } q^2 >> 2m^2x$$

ii) $$z^* = \frac{2E^*}{w}$$

iii) $$\mathfrak{z} = \frac{E^b + p^b_{/\!/}}{q} = \frac{z_b}{2}\left[1 \pm \left(1 + \frac{4m_t^2}{q^2 z_b{}^2}\right)^{\frac{1}{2}}\right]$$

where $$z_b = 2\frac{h.q}{q^2}$$

The labels lab, *, b refer to the lab, centre of mass, and Breit systems respectively: p, q, h are the four momenta of the incident nucleon, current and final state hadron respectively, and m_t the transverse mass given by $m_t{}^2 = m_h^2 + p_t{}^2$, m_h being mass of the hadron.

For q^2, $w^2 >> m^2$ the various definitions of z are nearly equal, and the selection $z_b > 0$ is equivalent to the selection on $x_f > 0$. However in the low q^2 region the two selections give quite different tracks forwards as shown by Fig 6.2, where the charge sum of the tracks forwards in the Breit frame, those forward in the centre of mass system, and those with $z_{lab} > 0.2$ are shown. For a fragmenting u-quark a value of

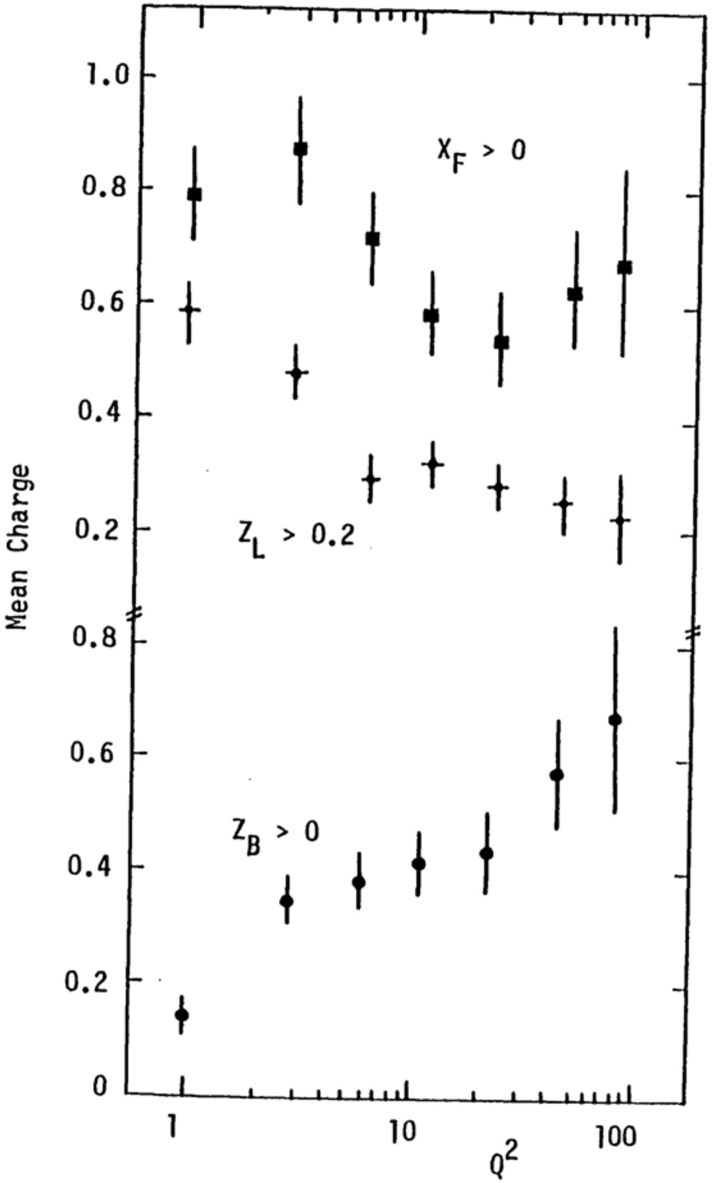

Fig 6.2 Average charge of hadrons in the current region.

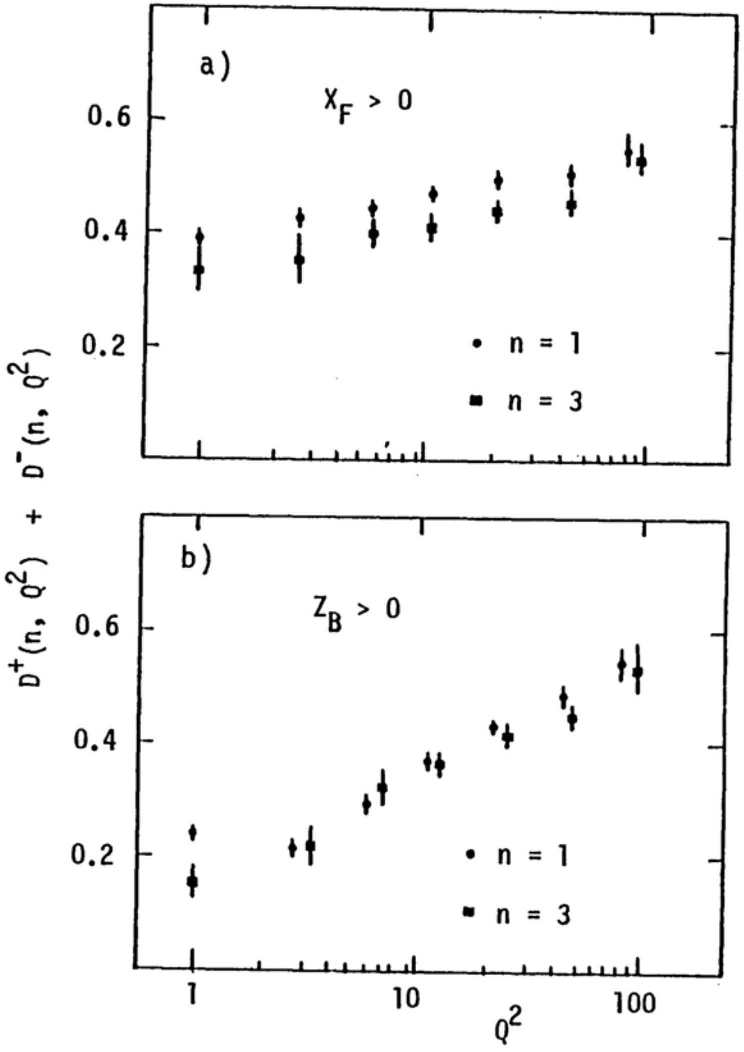

Fig 6.3 Energy-momentum conservation sum for current fragments.

the average charge sum $\sim\frac{2}{3}$ is expected. This is produced by both the selections $z_b > 0$ and $x_f > 0$ at high q^2, but not by $z_{lab} > 0.2$ which tends to cut out a large amount of the current fragments. At low q^2 the centre of mass frame gives a slightly higher value than expected, and the Breit frame a very low value due to very few tracks going forward at low q^2 (by definition there are no tracks in the forward region at $q^2 = 0$).

Since the variable z_{lab} is most directly related to measured quantities, this will be used in the analysis of the fragmentation functions with the selection $x_f > 0$ for the current fragments. However since theoretical predictions are often made in terms of the variable $\mathfrak{z}$, which is expected to give target mass independent results |3|, (ie it avoids contributions to non-factorisation which arise from target mass effects), and in order to check the sensitivity on the longitudinal variable, results on non-factorisation will also be presented in this variable.

A check on the validity of the analysis regarding the choice of longitudinal variables used and the method of track selection can be made by applying energy-momentum conservation which implies:

$$\int_0^1 z \ (D^{h^+} + D^{h^-} + D^{h^o}) \ dz = 1$$

so that, independent of the value of q^2 :

$$D^+ (n, q^2) + D^- (n, q^2) \sim \frac{2}{3} \qquad (5)$$

where:

$$D^{\pm}(n, q^2) = \int_0^1 \int_0^1 x^{n-1}\, z\, D^{\pm}(x, z, q^2)\, dx\, dz$$

The sum given by equation (5) is shown in Fig 6.3a for tracks forward in the centre of mass frame and using z_{lab}, and in Fig 6.3b for tracks forward in the Breit frame and using z_b. In Fig 6.3a the value of the sum shows a q^2 dependence and approaches the expected value only at the highest q^2 for $n = 1$ and shows an even larger deviation from the expected value for $n = 3$. The situation is even worse for the Breit frame, which gives very low values of the sum at low q^2. However, there is little x (ie n) dependence of the sum for the Breit frame definitions.

The low values of the energy-momentum conservation sum for the variable z_{lab} could be due partly to mis-identification of protons and kaons as pions so that they enter the sum with too small a value of z; and partly due to mis-classification of current fragments as target fragments, particularly at low w (chapter 4, section 4.2.2). Much of the effect in the Breit variable is attributable to the definition of forward tracks which gives a diminishing number of tracks forwards as $q^2 \to 0$.

The q^2 dependence of the energy-momentum conservation sum should not imply q^2 dependent effects in the analysis of the non-singlet combination of fragmentation functions (section 6.5 to 6.9) since the q^2 behaviour of both the D^{h^+} and D^{h^-} is similar (section 6.4).

6.4 Simple tests of Factorisation and Scaling

The z dependence of the fragmentation functions $D_q^h(z, x, q^2)$ defined in section 6.3 is shown in Fig 6.4 for positive and negative hadrons at fixed low and high q^2 ranges, for $x \gtrless 0.3$. At low q^2 a substantial x dependence of the positive hadron fragmentation functions, and within the poor statistics, some x dependence of the negative hadron

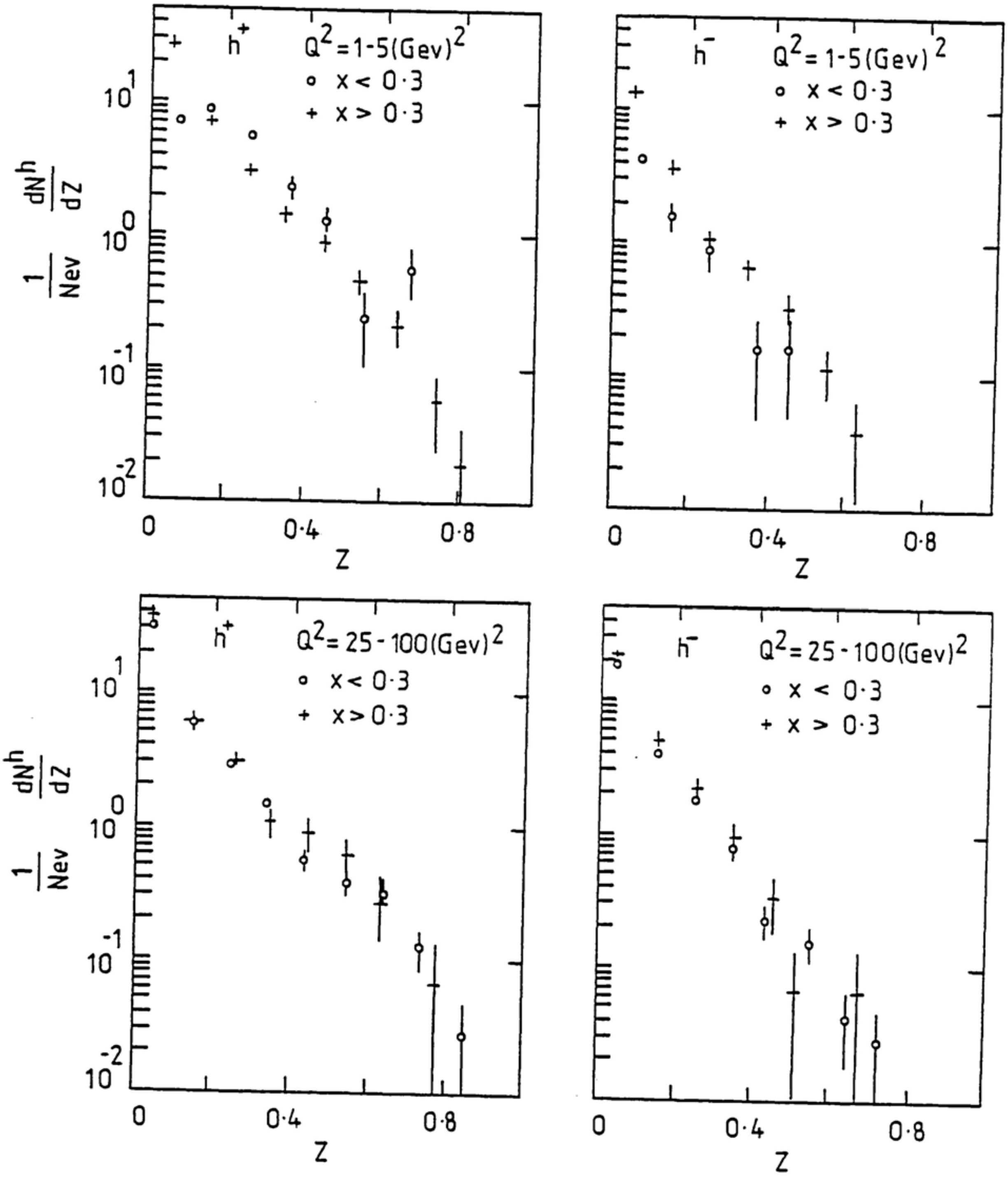

Fig 6.4 Fragmentation functions of positive and negative hadrons at fixed x and q^2.

fragmentation functions is observed. At large q^2 the data is consistant with no x dependence.

The fragmentation functions integrated over z, which improves statistics, are shown in Fig 6.5. In addition to the x-dependence at fixed q^2, corresponding to non-factorisation; there is a considerable q^2 dependence, ie non-scaling, at fixed x (Fig 6.5a and b). Since

$$w^2 = m^2 + q^2 \left(\frac{1}{x} - 1\right) \sim q^2 \left(\frac{1}{x} - 1\right)$$

this implies a dependence of the fragmentation functions on w. In fact the data shows that most of the dependence at fixed q^2 is due to a dependence on w^2 since at fixed w there is little x dependence (Fig 6.5c and d), or q^2 dependence (Fig 6.5e and f) so that there is factorisation in w^2, (such effects have also been observed in the ν/H_2 data of reference 6).

Thus the form of the single particle cross-section given by equation (3) does not hold, and an extra x as well as a q^2 dependence is present in the fragmentation function: $D_q^h\,(z, x, q^2)$ and equation (4) is appropriate. If x and q^2 are replaced by w: $D_q^h\,(z, w^2)$ then factorisation is restored and equation (3) takes the form:

$$\frac{d\sigma}{dx\,dz} \propto F(x, q^2)\ \ D_q^h\,(z, w^2)$$

6.5 Non-Singlet Moments

6.5.1 z Moments

The QCD predictions for the q^2 dependence of the z moments of the fragmentation functions are simplest for the non-singlet combination

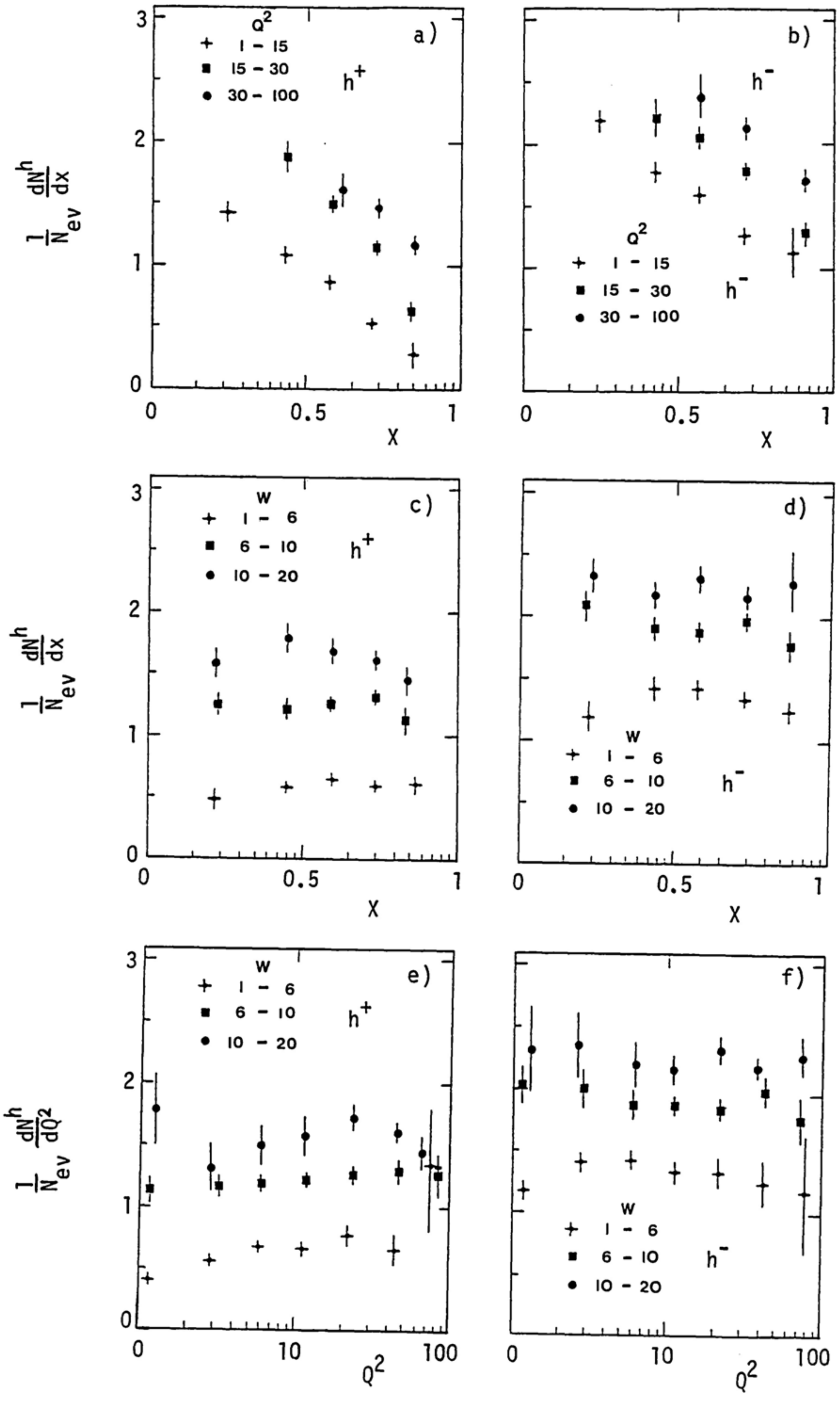

Fig 6.5 Test of variables for factorisation of fragmentation functions.

(Appendix 2) since gluon fragmentation does not contribute. Such a non-singlet can be defined by the charge sum of the observed hadrons:

$$D^{+} - D^{-} = D^{+}_{u_v} + D^{+}_{u_s} - D^{-}_{u_v} - D^{-}_{u_s}$$

where u refers to the fragmenting quark flavour, v(s) to valence (sea) quark and +, - to the charge of the produced hadrons. Then, since most of the produced hadrons are pions, applying charge conjugation (D^{+}_{u} = $D^{-}_{\bar{u}}$) and assuming an exact SU(3) symmetric sea (u_s = d_s) gives:

$$D_{ns} = D^{+} - D^{-}$$

The non-singlet moments given by equation (1) with D^{h}_{q} replaced by the non-singlet fragmentation function combination D_{ns} are shown in Fig 6.6 together with the QCD curves given by equation (2), assuming a value of $\Lambda^2 = 0.25$. There is quantitative agreement with the prediction at small m ($\leqslant 3$), however at larger values of ($m \geqslant 4$) the data shows practically no q^2 dependence. The QCD curves have been fitted for $q^2 > 2$ in order to avoid much of the contribution from elastic events which dominate the low q^2 region, ($q^2 < 2$ (Gev/c)^2 |1|).

6.5.2 p_t Moments

The longitudinal variable z studied above is sensitive to the soft, collinear processes |4|:

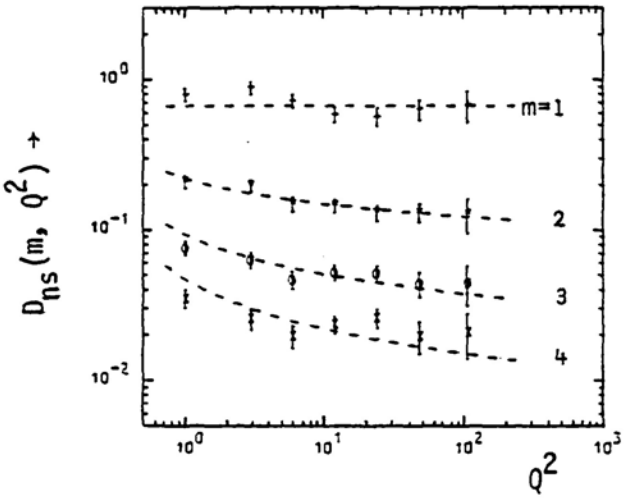

Fig 6.6 Non-singlet z moments.The The index m represents integration over powers of the z distribution.

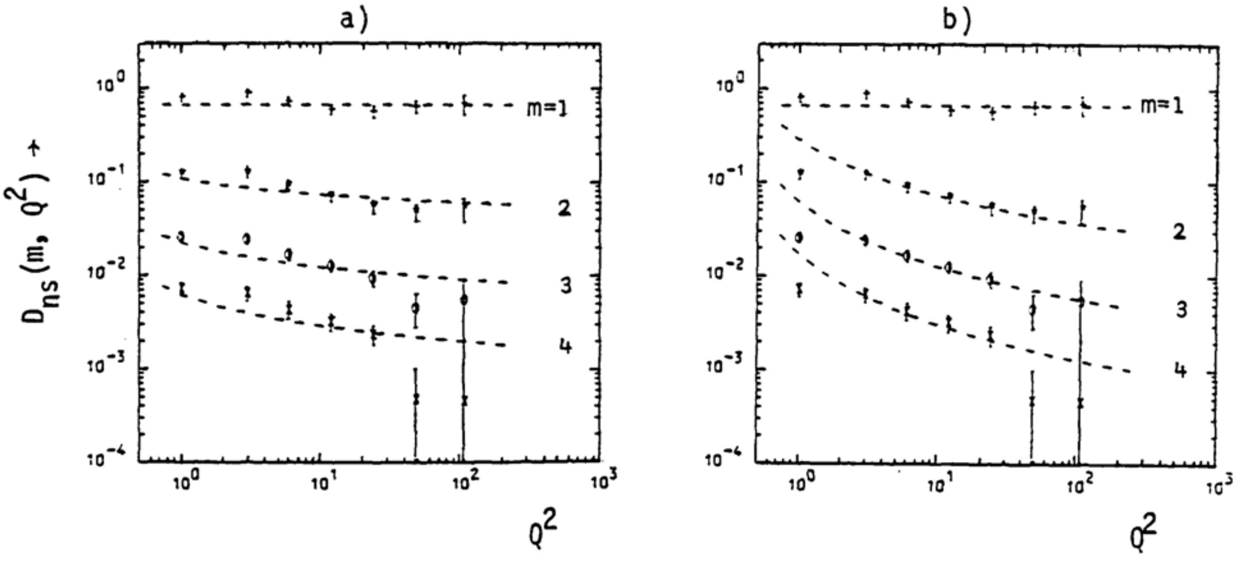

Fig 6.8 Non-singlet (single) moments in x_t assuming, a) d_{ns} and, b) $d_{ns} + 1$ for the anomalous dimensions.

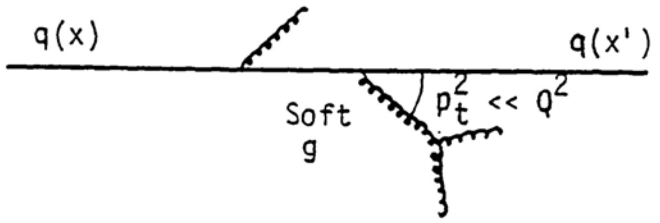

which, in the context of perturbative QCD formulism, are re-absorbed to give the scaling violations predicted by equation (2).

However, QCD predicts also the emission of hard gluons:

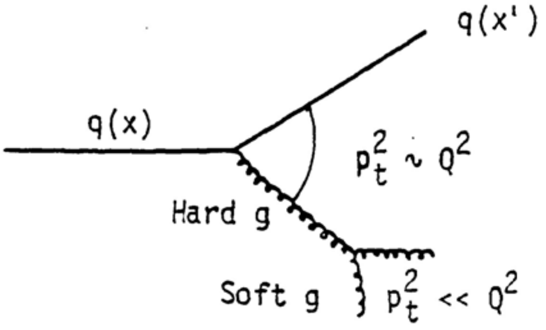

Fig 6.7

Clearly in order to study this process requires a variable sensitive to the transverse momentum. Suitably scaled transverse variables are given by:

$x_t = \frac{2p_t}{W}$ where p_t is measured relative to the hadronic axis

$x_{t_o} = \frac{2p_t^{out}}{W}$ where p_t^{out} is measured relative to the lepton plane

Moments of x_t are shown in Fig 6.8 with the QCD prediction of equation (2). The data shows a much stronger q^2 dependence than predicted. However, if the anomalous dimensions are replaced such that:

$$d^{ns}_{x_t} = d^{ns}_{z} + 1$$

where the extra 1 is expected theoretically due to the extra vertex, Fig 6.7 |4|, there is good agreement with the prediction for $q^2 > 2$ (Gev/c)^2.

6.6 Double Moments Analysis

The fragmentation function moments presented above are effective moments averaged over the x region accessible at a given value of q^2, which is governed by the maximum neutrino beam energy. At low q^2 the moments are averaged over almost the whole x range, whereas at high q^2 the x range is limited. Since at low q^2 factorisation has been observed not to hold (section 6.4), double moments of the x and z distribution, are defined such that they are independent of the beam spectrum |5|.

The cross-section for producing a hadron is given by equation (4):

$$\frac{d^2\sigma}{dx\ dz\ dq^2} = \frac{G^2ME}{\pi}\ \frac{F(x,\ q^2)}{x}\ D^h\ (z,\ x,\ q^2)$$

$$= K\ \frac{dN^h}{dx\ dz\ dq^2} \Big/ \mathrm{FLUX}\ (x,\ q^2)$$

where $\frac{F}{x}(x,\ q^2) = Q(x) = 2\pi K\ \frac{dN_{ev}}{dq^2\ dx} \Big/ \mathrm{FLUX}\ (x,\ q^2)$

$=$ Quark momentum distribution.

$$\mathrm{FLUX}(x,q^2) = \int_{\frac{q^2}{2mx}}^{E_{max}} \phi(E)\ dE.$$

$\phi(E)$ being the incident neutrino flux as a function of the beam energy and E_{max} the maximum neutrino beam energy. The constant K depends on the number of target protons and neutrons and the overall flux normalization.

The double moments of the fragmentation function are then defined by:

$$D(m,\ n,\ q^2) = \frac{\int_{x_{min}}^{1} \int_{0}^{1} z^{m-1}\ x^{n-1}\ Q(x)\ D\ (z,\ x,\ q^2)\ \ dz\ dx}{\int_{x_{min}}^{1} x^{n-1}\ \ Q(x)\ \ dx} \qquad (6)$$

where $x_{min} = \dfrac{Q^2}{2m_p\ E_{max}}$

In equation (6) the m'th moment of the fragmentation function, at a given q^2, is averaged over the n'th moment of the x-distribution, weighted by the neutrino beam spectrum so that the moments are spectrum independent. In the limit of no x dependence equation (6) is equivalent to equation (1) where the x dependence is implicity integrated over.

Since the beam energy is finite ($E_{max} = 200$ Gev), x_{min} does not go to zero so that the x integrations are incomplete. The effect of this will be greater at low n, especially $n = 1$ which samples the structure function like $1/x$. The effect of various cuts on x on the $n = 1$ moments is shown in Fig 6.9 for various q^2 bins. The moments approach a constant value as the lower limit of integration approaches the kinematic limit x_{min}, so that within errors the moments measured down to x_{min} are complete.

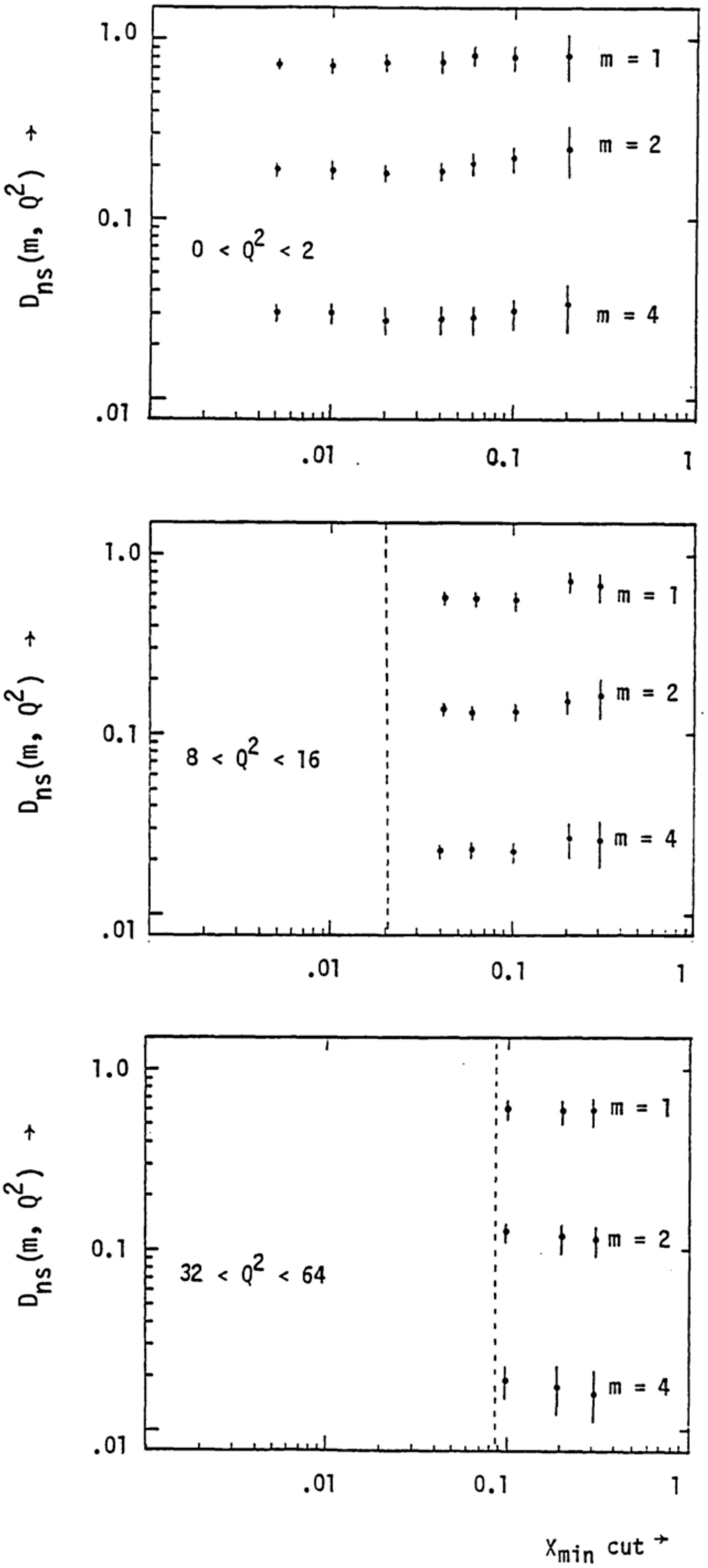

Fig 6.9 Effects on the z moments of fragmentation functions of a lower cut on x. (No data below x values at the dotted lines).

The set of double moments of z_{1ab} and z_b for $n = 1$ to 4, $m = 1$ to 4 are shown in Fig 6.11 and Fig 6.12. The q^2 behaviour of the moments is very similar for the two variables for $n > 2$, for $m > 1$ and $q^2 > 4$ $(\mathrm{Gev}/c)^2$. The upward movement of the data points for $n > 1$ relative to the 1st order curves of equation (1), fitted for the constants c_m to the $n = 1$ moments assuming $\Lambda^2 = 0.25$, shows evidence of an x dependence of the non-singlet combination of the fragmentation functions. The x-dependence is strongest at low q^2 (< 20 Gev/c^2) and qualitatively similar to that of the D^{h^+} and D^{h^-} fragmentation function (section 6.4).

The x_t moments shown in Fig 6.13 produce a similar trend to the z moments for the x-dependence (non-factorisation) of the fragmentation functions. The QCD curves in Fig 6.13 assume $d_{ns} + 1$ for the anomalous dimensions, and $\Lambda^2 = 0.25$. (The x_{t_0} moments (not shown) give very similar q^2 dependence to the x_t moments).

6.7 QCD tests of Factorisation Breaking

In the framework of QCD factorisation breaking can occur due to processes beyong the leading order. Diagrams contributing to the cross-section in next to leading order perturbative QCD are |8|:

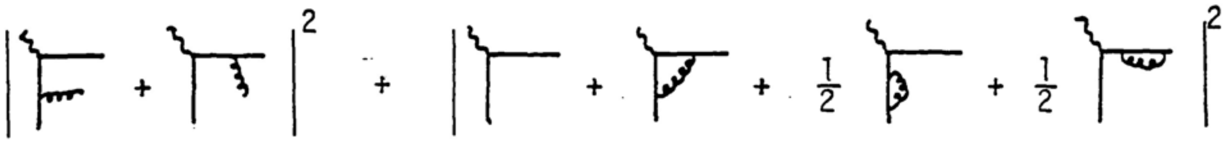

a) W q → q x

Fig 6.10

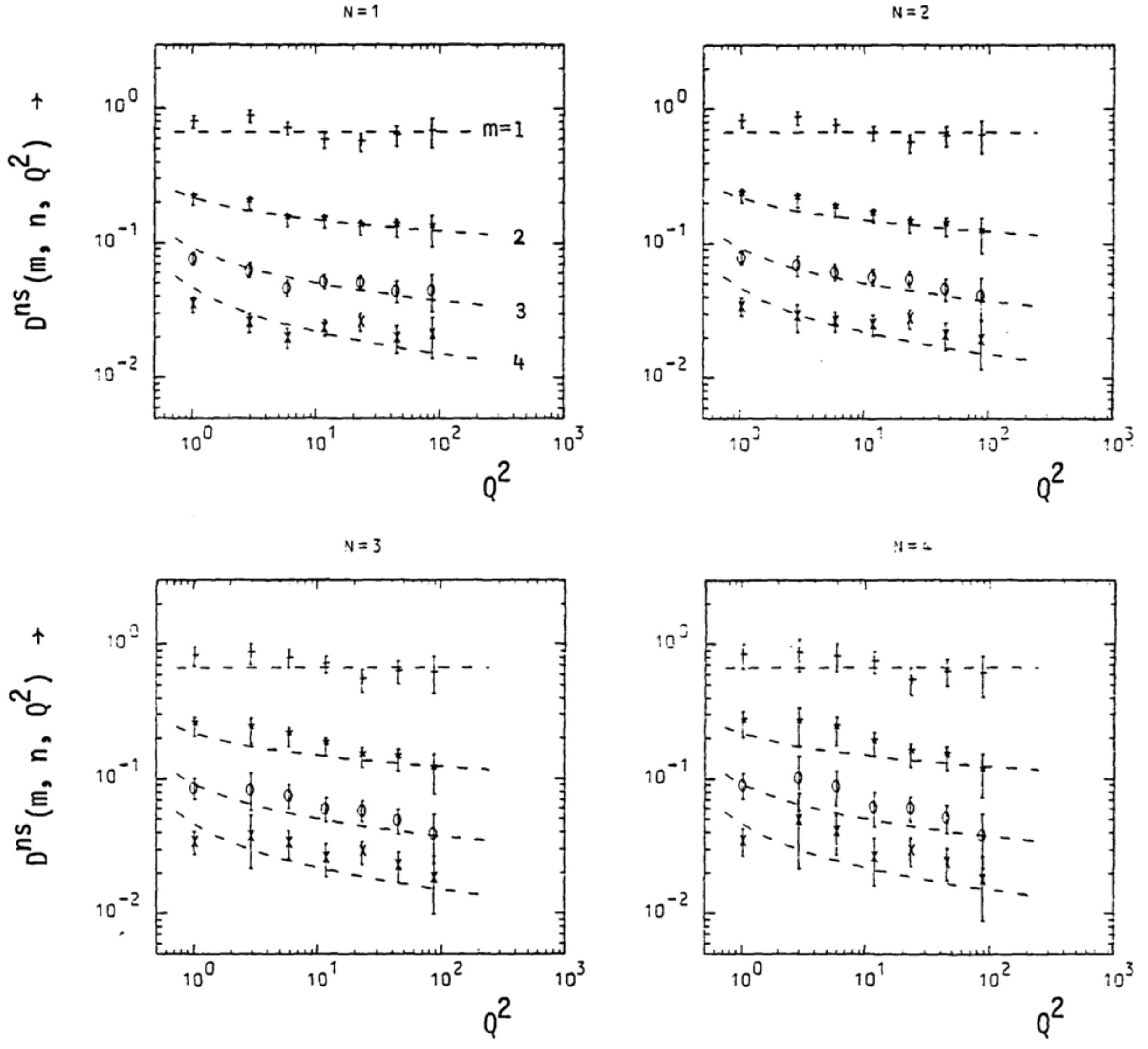

Fig 6.11 Non-singlet double moments in z_{lab}. The index m represents an integration over powers of the z_{lab} distribution, and n over powers of the x distribution. The QCD curves assume $\Lambda^2 = 0.25$.

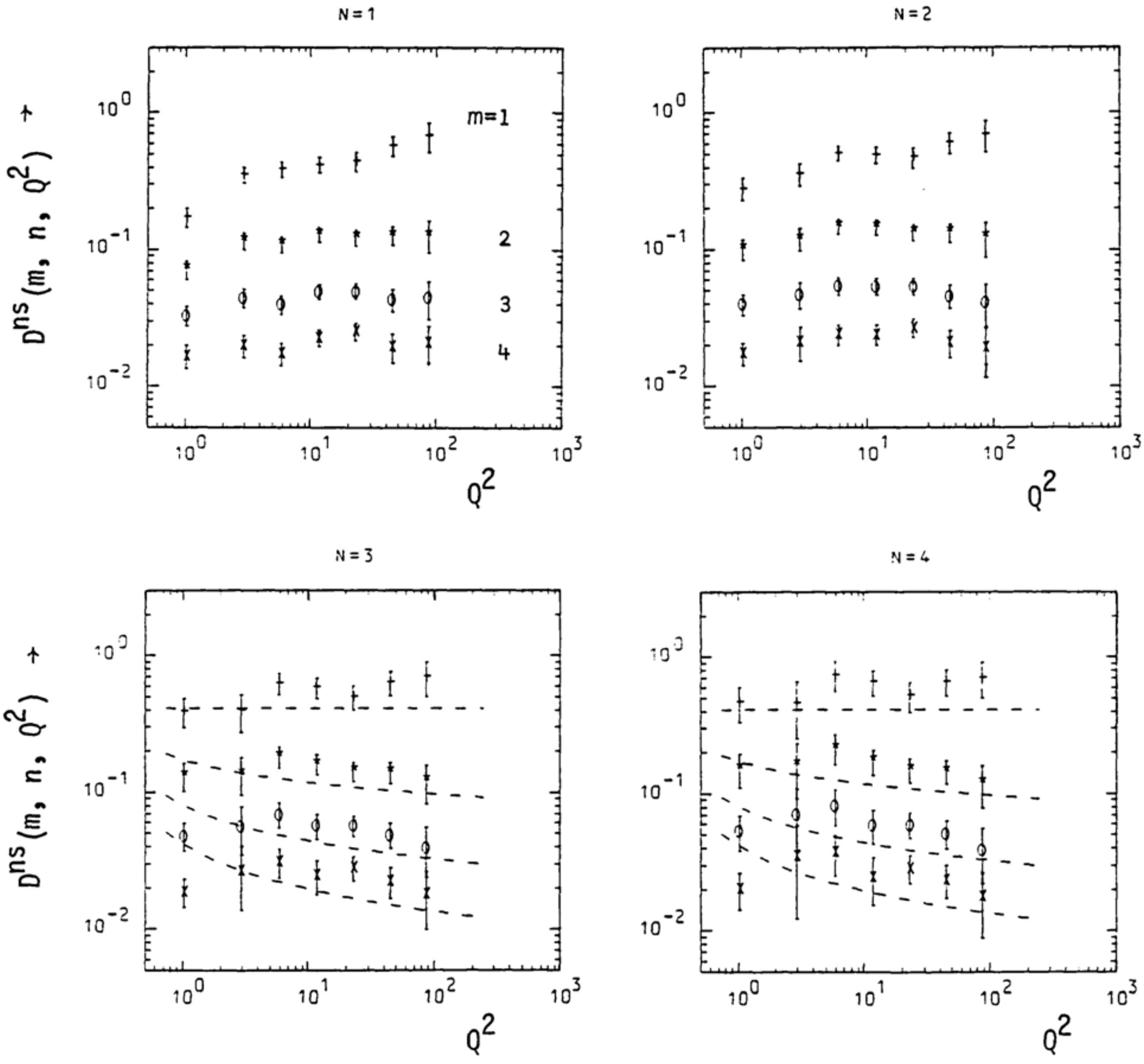

Fig 6.12 Non-singlet double moments in z_b. The QCD curves assume $\Lambda^2 = 0.25$.

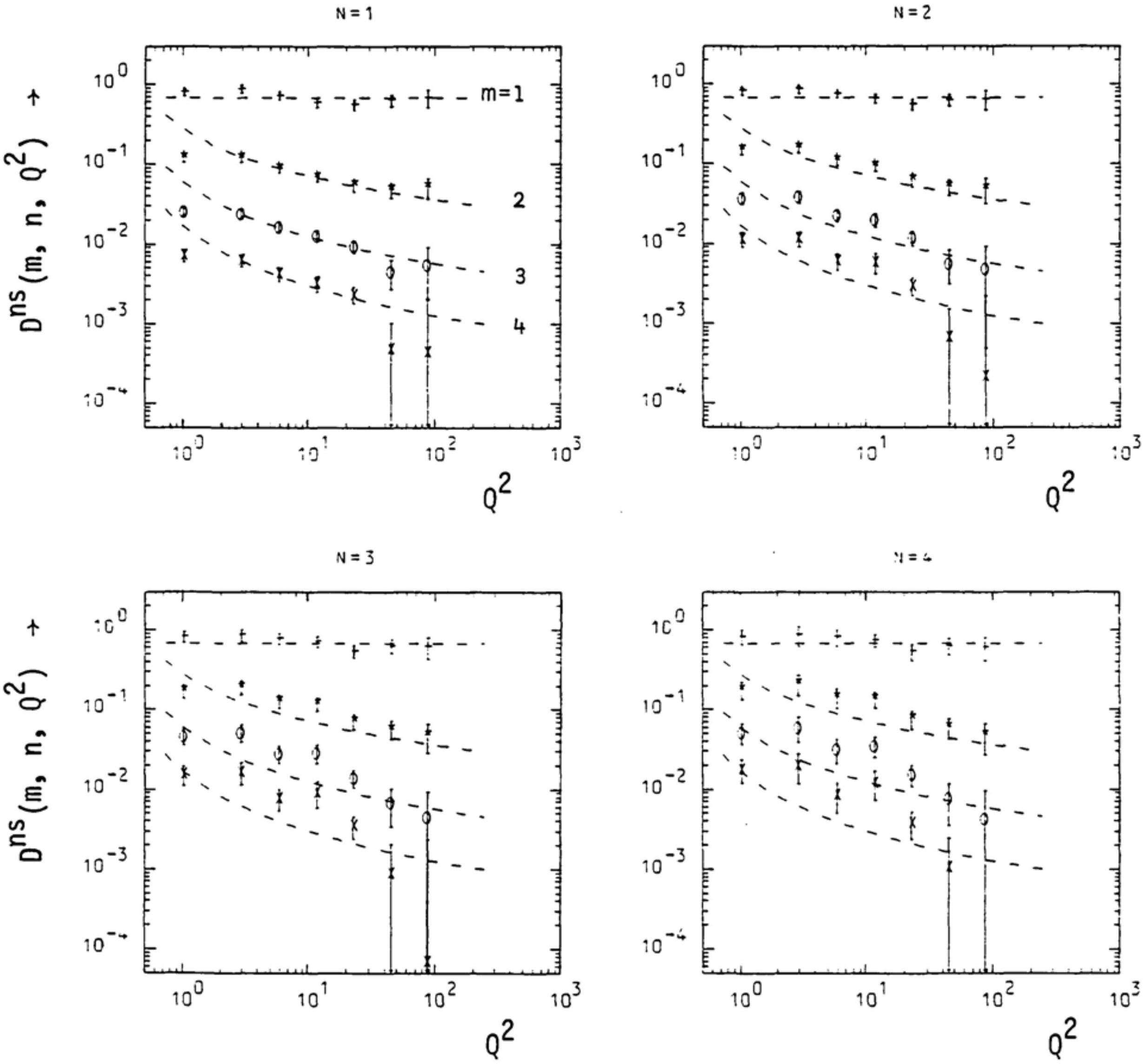

Fig 6.13 Non-singlet double moments in the x_t variable. The QCD curves assume $\Lambda^2 = 0.25$ and $d_{ns} + 1$ for the anomalous dimensions.

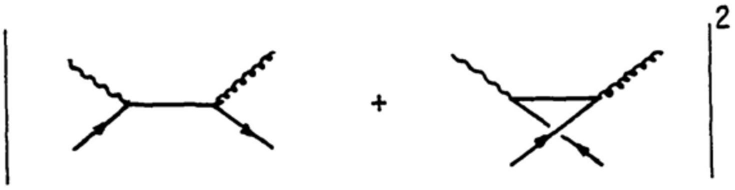

b) W q → g x

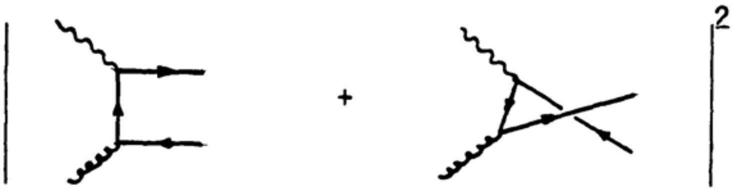

c) W g → q x

Fig 6.10

For the non-singlet combination considered here only diagram a) contributes and so provides the cleanest test. The size of the factorisation breakdown appearing in the double moments is given by the constants c_{nm}:

$$D'_{nm} \sim F_n\,(q^2)\;\;D_m(q^2)\;\;c_{nm} \qquad (7)$$

where $$c_{nm} = 1 + \alpha_s\,(a + b_n + c_m + d_{nm})$$

a being a constant and b_n, c_n, d_{nm} constants dependent on the n'th x and m'th z moment. Taking the ratio of equation 7 for two different n moments gives:

$$R_1\;(n_1, n_2, m) = \frac{D'_{n_1m}\;\;f_{n_2}}{f_{n_1}\;\;D'_{n_2m}} = \frac{D_{n_1m}}{D_{n_2m}}$$

$$= 1 + \frac{\alpha_s}{4\pi} \left(b_{n_1} + d_{n_1 m} - B_{n_1} - b_{n_2} + d_{n_2 m} + B_{n_2}\right) \qquad (8)$$

where B_n are the next to leading order corrections to the structure function moments |9|.

The ratio R_1 is shown in Fig 6.14 for $m = 5$ and two sets of intermediate values of n, for z_{1ab} and z_b. The two variables give similar results for $q^2 > 5$ (Gev/c)^2 but for $q^2 < 5$ (Gev/c)^2 the z_b variable gives smaller values of R_1. The QCD predictions with $\Lambda^2 = 0.25$, (solid line) agrees with the data in the intermediate q^2 range but over-estimates the magnitude of the factorisation break-down at large q^2. Furthermore the data indicates a return to factorisation in the low q^2 region whereas QCD predicts a continued increase in the magnitude of the factorisation breakdown. However this may be due to the unreliability of perturbative QCD in this region of low q^2.

The ratio R_1 contains second order corrections B_n, to the structure function. These can be eliminated by taking the ratio of R_1 for two different values of m:

$$R_2\,(n_1, m_1; n_2, m_2) = \frac{D\,(n_1, m_1)\;\; D\,(n_2, m_2)}{D\,(n_1, m_2)\;\; D\,(n_2, m_1)}$$

$$= 1 + \frac{\alpha_s(q^2)}{4\pi}\; d_{n_1 m_1,\, n_2 m_2} \qquad (9)$$

For the non-singlet the constants $d_{n_1 m_1, n_2 m_2}$ are given by:

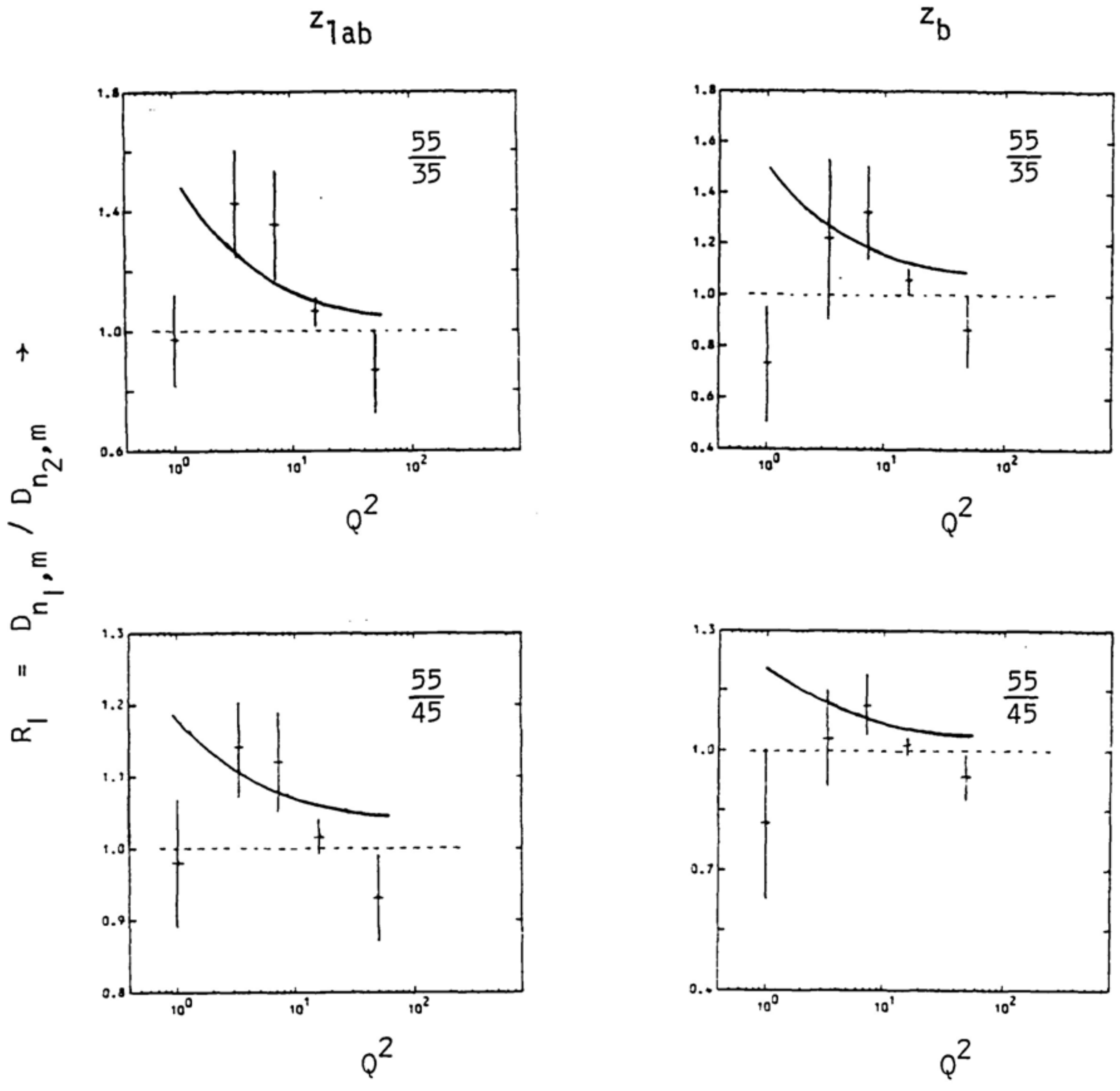

Fig 6.14 Test of non-factorisation using the ratio (R_l) of the double moments. The solid lines are the predictions of next to leading order QCD and the dotted lines of the quark-parton model. (Results are given for both the z_{lab} and z_b variables).

$$d^{qq}_{nm,kl} = \frac{8}{3} \left[\sum_{j=k}^{n-1} \frac{1}{j} \sum_{i=l}^{m-1} \frac{1}{i} + \sum_{j=k+2}^{n+1} \frac{1}{j} \sum_{i=l+2}^{m+1} \frac{1}{j} + \frac{2\,(n-k)\,(m-1)}{(n+2)\,(k+2)\,(m+1)\,(l+1)} \right] \quad \begin{matrix} n > k \\ m > l \end{matrix}$$

Where for clarity n_1 m_1 n_2 m_2 have been replaced by n, m, k, l respectively.

The size of the factorisation breakdown is clearly largest for k, l small and n, m large. However the predictions are expected to be unreliable at large n and m, and in order to get results relatively free of target fragments requires k, l not too small.

The values of $R_2^{\dagger}$ are shown in Fig 6.15 for z_b and z_{lab}. For small values of n_2, m_2 the data is consistent with the QCD prediction at intermediate values of q^2. For larger values of n_2 m_2, for which QCD predicts a very small deviation of R_2 from one, the data is consistent with both QCD and factorisation indicating the need to reduce errors on the data points before firm conclusion about the agreement with QCD can be made. The fact that for values of n_1, m_1, n_2, m_2 which are close together z_b moments give values of R_2 which often fall below one suggests that this choice of variables and frame is not as reliable as using z_{lab} and the centre of mass system, (assuming the sign of the non-factorisation is such as to make $R_2 > 1$). Only z_{lab} will be used for further tests.

† Errors on the ratio tests have been determined by dividing the data into four sub-samples and computing the spread on the mean values of the ratio determined from the sub-samples. Due to the limited number of sub-samples the errors are only approximate.

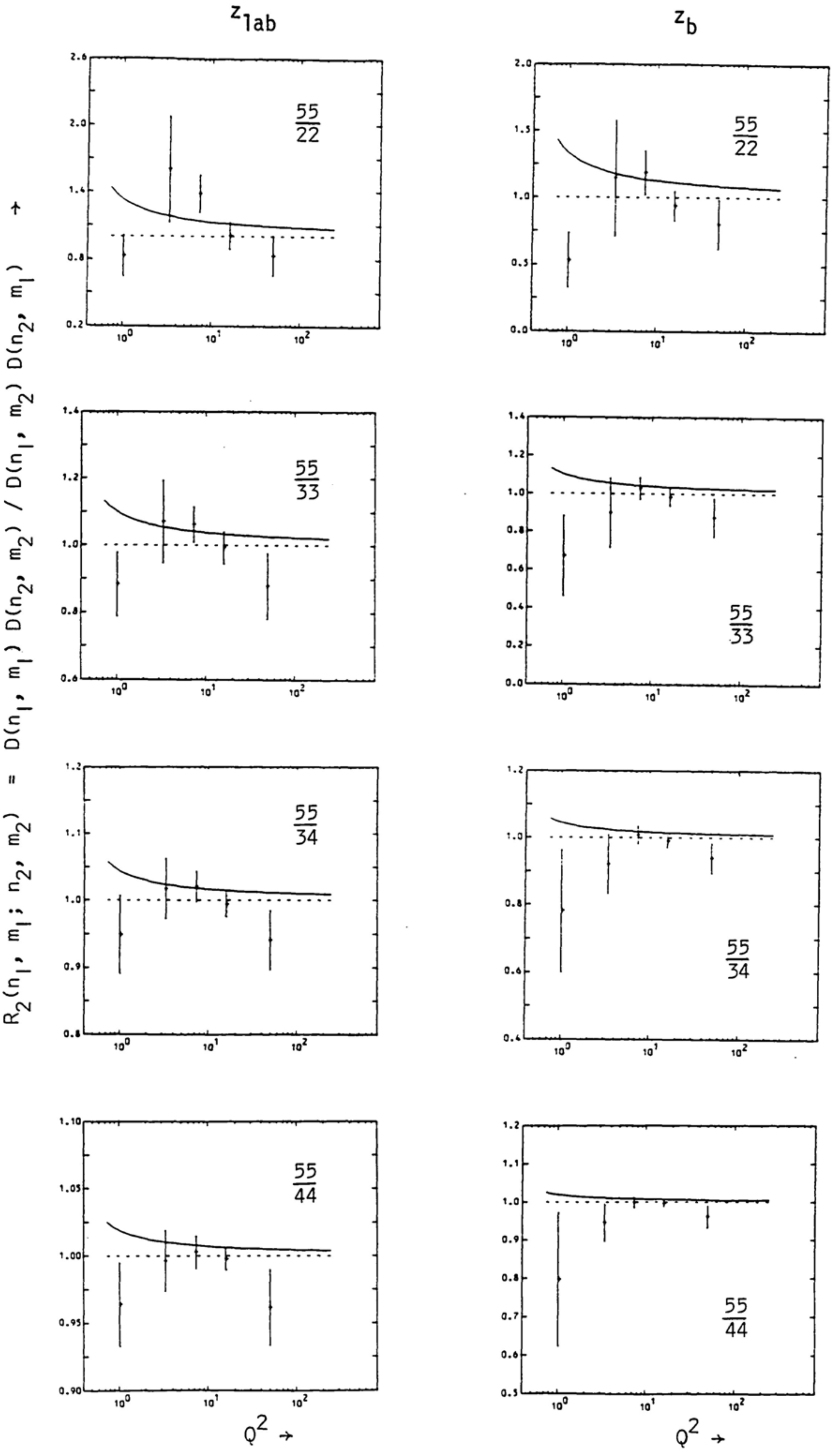

Fig 6.15 Ratio (R_2) of the double moments compared to the predictions of QCD (solid lines) and the quark-parton model (dotted lines)

The dependence of R_2 on α given in equation 9, can be eliminated in order to investigate the n and m dependence of non-factorisation by evaluating the ratio:

$$R_3\ (n_1, m_1; n_2, m_2) = \frac{R_2\ (n_1, m_1; n_2, m_2)\ -\ 1}{R_2\ (n_1', m_1'; n_2', m_2'\ -\ 1}$$

$$= d_{n_1\ m_1,\ n_2\ m_2} - d_{n_1'\ m_1',\ n_2'\ m_2'}$$

Thus the ratio R_3 is expected to be approximately independent of q^2 (as only leading terms have been retained in R_1 and R_2), and dependent only on the non-factorisable part of the non-singlet cross-section. The values of R_3 obtained from the data for z_{1ab} for $n_1, m_1 = 3$ to 5 with $n_2 = n_1 - 1$ and $m_2 = m_1 - 1$; and $n_1', m_1' = 4$ and $n_2', m_2' = 3$ are given in table 6.1. The theoretical predictions are given in brackets.

n_1 n_2 m_1 m_2	2 3	3 4	4 5
2 3	1.99 ± 0.27 (1.66)	1.56 ± 0.26 (1.29)	1.39 ± 0.16 (1.05)
3 4	1.24 ± 0.16 (1.29)	1.00 (1.0)	0.92 ± 0.04 (0.80)
4 5	0.62 ± 0.31 (1.05)	0.51 ± 0.13 (0.80)	0.92 ± 0.10 (0.67)

a) $q^2 = 0 - 150$

b) q^2 = 0 - 5

n_1 n_2 / m_1 m_2	2 3	3 4	4 5
2 3	1.69 ± 0.53	1.36 ± 0.35	1.04 ± 0.21
3 4	1.28 ± 0.16	1.0	0.75 ± 0.08
4 5	0.70 ± 0.19	0.53 ± 0.22	0.39 ± 0.25

c) q^2 = 5 - 25

n_1 n_2 / m_1 m_2	2 3	3 4	4 5
2 3	3.05 ± 0.59	1.59 ± 0.69	1.05 ± 0.43
3 4	1.76 ± 0.46	1.0	0.78 ± 0.07
4 5	0.85 ± 0.89	0.50 ± 0.32	0.42 ± 0.13

d) q^2 = 25 - 150

n_1 n_2 / m_1 m_2	2 3	3 4	4 5
2 3	1.24 ± 0.11	1.75 ± 0.08	2.01 ± 0.05
3 4	0.68 ± 0.07	1.0	1.22 ± 0.02
4 5	0.32 ± 0.13	0.49 ± 0.08	0.61 ± 0.09

Table 6.1

The values of R_3 averaged over the experimental range of q^2 shows a faster decrease with increasing m, and a slower decrease with increasing n than predicted by theory so that the expected symmetry in m and n of the non-factorisable part of the single particle inclusive cross-section is not observed. There is no significant q^2 dependence of R_3 determined for the ranges of q^2 = 1 - 5 and q^2 = 5 - 25 within errors (table 6.1b and C), as predicted. However at larger values of q^2 = 25 - 150, the trend in n changes and R_3 increases with increasing n in contradiction to the theoretical prediction.

6.8 n dependence of Λ

The non-factorisable terms in the single particle inclusive cross-section, given by terms in the constants c_{nm} appearing in equation (7), change the form of equation (2) to:

$$D_{nm}(q^2) = \frac{k_m}{\ln(q^2/\Lambda^2)^{d_{ns}}} \left[1 + \frac{E_{nm}}{\ln(q^2/\Lambda^2)} + \ldots\ldots\right] \qquad (10)$$

Where E_{nm} are constants dependent on n and m due to 2nd order QCD diagrams. Equation (10) can be put into the form of equation (2) by introducing an effective n dependence to Λ |10|:

$$D_{nm}(q^2) = \frac{k'_{nm}}{\ln(q^2/\Lambda_n^2)^{d_{ns}}} \qquad (11)$$

The relation between Λ_n and the QCD free-parameter Λ, is dependent on convention so that only the ratio of Λ_n for different values of n is important. The values of Λ_n obtained from fits to the double moments

m \ n	1	2	3	4	5
2	0.88 ± .5	0.94 ± .12	1.11 ± .31	1.26 ± .49	1.33 ± .46
3	0.09 ± .16	0.32 ± .36	0.11 ± .43	0.99 ± .40	1.14 ± .47
4	<.005	0.04 ± .44	0.41 ± .49	0.79 ± .44	0.99 ± .73
2, 3 & 4	.07 ± .21	.25 ± .23	.63 ± .08	.87 ± .32	1.01 ± .13

Table 6.2

allowing k'_{nm} to vary as a free parameter are given in table 6.2 as a function of n and m. At Larger ~~small~~ values of n (> 2), the experimentally obtained values of Λ_n are consistent with being independent of the m as predicted by the form of equation (11). There is evidence of an n dependence of Λ_n seen from the global fits to m = 2 to 4 moments, indicating the relevance of the higher order QCD corrections.

6.9 Anomalous Dimensions of x_t

6.9.1 Tests based on Chi-Square function

It has been observed (section 6.5.2), that the q^2 dependence of the moments of x_t shows better agreement to the predictions given by the leading order equation (2) if an extra power of 1 is added to the anomalous dimensions of the z moments, for $\Lambda^2 = 0.25$. However the form of equation (2) suggests that Λ and d_{ns} behave in a complementary way so that an increase in d_{ns} is equivalent to a decrease in Λ.

In order to assess if the data shows a preference as to what is the appropriate value of the anomalous dimensions, the chi-squares resulting from global fits to the m = 2 to m = 4 double moments of x_t assuming separately values of the anomalous dimensions equal to d_{ns} and $d_{ns} + 1$ are shown as a function of Λ in Fig 6.16. The chi-square functions for $n > 1$ ($n = 3$ shown) are essentially lateral displacements of the $n = 1$ functions so that the same conclusions can be drawn by looking at any n. The plots of Fig 6.16 suggest that the data indicates only a slight preference for $d_{ns} + 1$ for the anomalous dimensions. This conclusion is reinforced by comparing the values of Λ obtained from global fits to m = 2, to 4 z moments to those obtained from x_t moments. The values are in better agreement for the two cases when $d_{ns} + 1$ is used for the x_t moments, as shown in table 6.3.

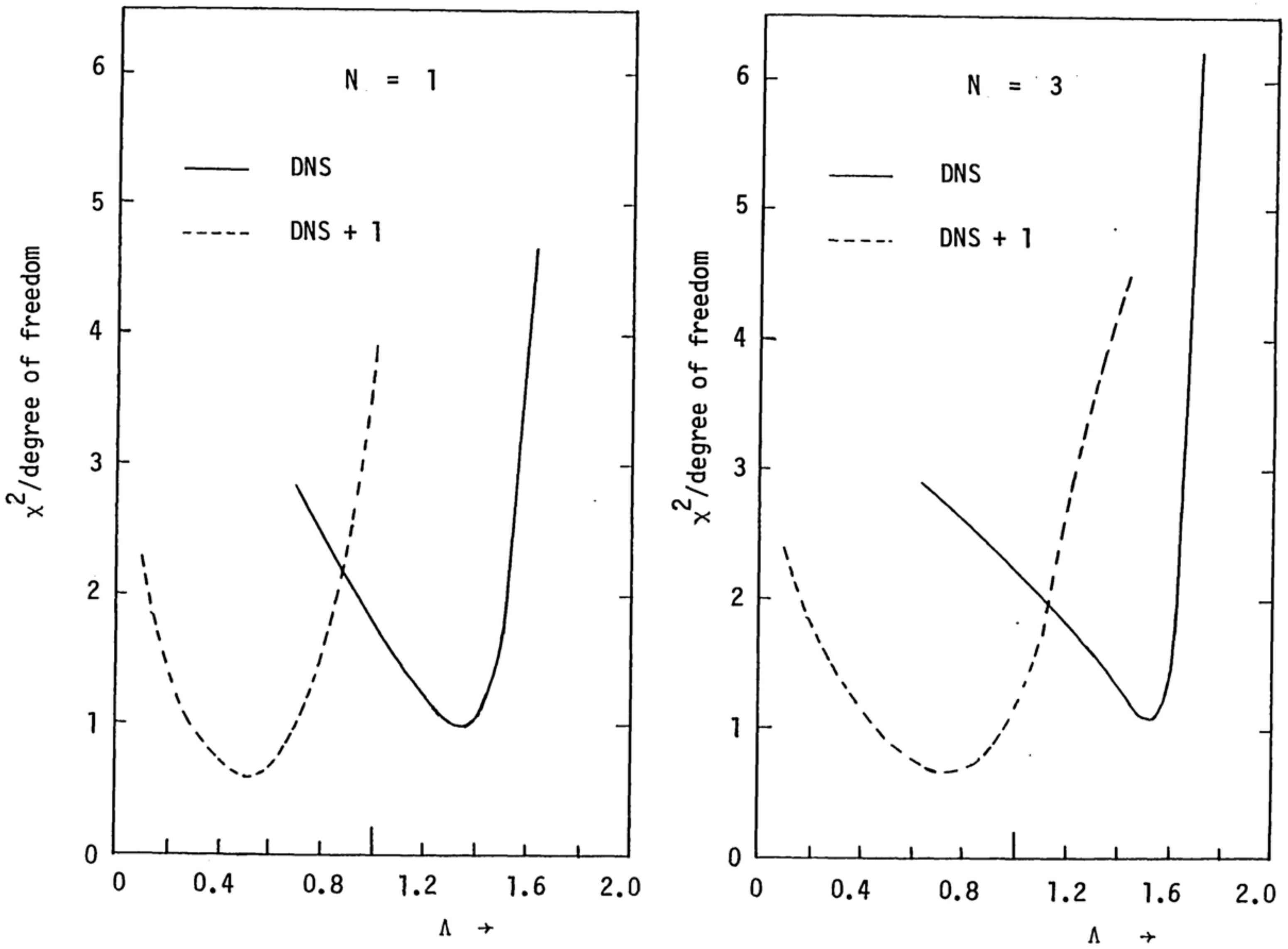

Fig 6.16 Chi-square functions from fits to double moments of x_t, assuming different values of the anomalous dimensions.

Λ \ n	1	2	3	4	5
z	0.11 ± .2	0.34 ± .24	0.73 ± .27	1.01 ± .26	1.15 ± .14
x_t (d_{ns} + 1)	0.52 ± .08	0.67 ± .09	0.75 ± .11	0.81 ± .13	0.85 ± .33
x_t (d_{ns})	1.35 ± .04	1.46 ± .03	1.52 ± .04	1.55 ± .05	1.57 ± .05

Table 6.3

6.9.2 Tests Independent of Λ

The QCD parameter Λ can be eliminated from the lowest order equation (1) (or from the higher order equation 11) by taking logs for two different m moments:

$$\ln D_m = \ln c_m - d_m \ln \ln (q^2/\Lambda^2)$$

and

$$\ln D_{m'} = \ln c_{m'} - d_{m'} \ln \ln (q^2/\Lambda^2)$$

so that:

$$\ln D_m (q^2) = \frac{d_m}{d_{m'}} \ln D_{m'} (q^2)$$

Thus a plot of log D_m vs log $D_{m'}$ should yield a straight line with a gradient equal to the ratio of the non-singlet anomalous dimensions $d_m/d_{m'}$. Such plots are shown in Fig 6.17a for m' = 2, m = 3 at n = 1 and n = 5, (higher values of m have not been used since the z moments for these show little q^2 variation, especially for n = 1, so that the points appear clustered together on the plot and the gradient cannot be evaluated). The data is consistent with a linear behaviour, although it does not properly distinguish the ratios of anomalous dimension of vector gluons (solid line in the figure) from those for scalar gluons (dotted line in the figure) because of large errors.

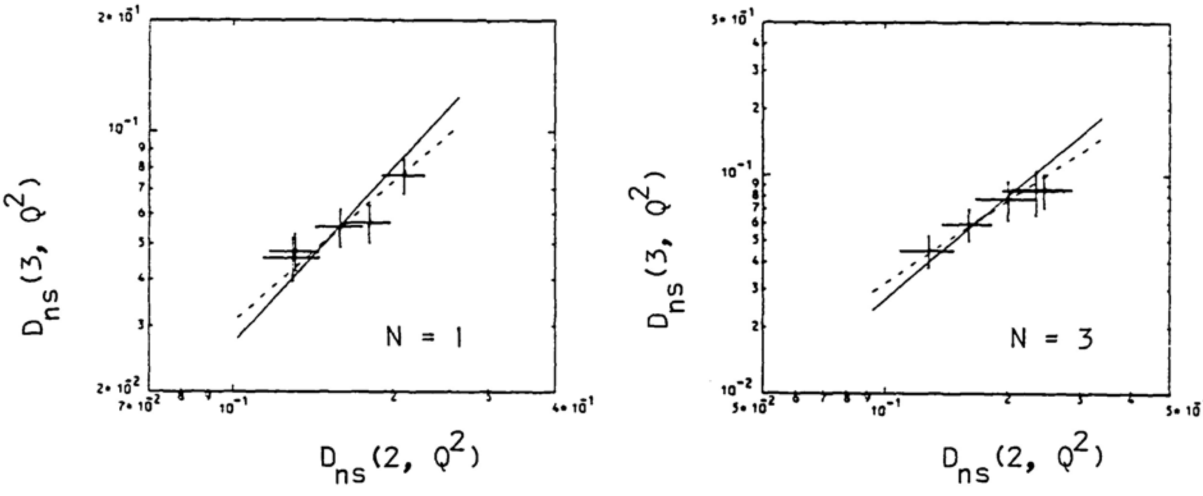

Fig 6.17a Log m vs log m' plot of non-singlet double moments. The straight lines have gradients given by vector gluons (solid) and scalar gluons (dotted).

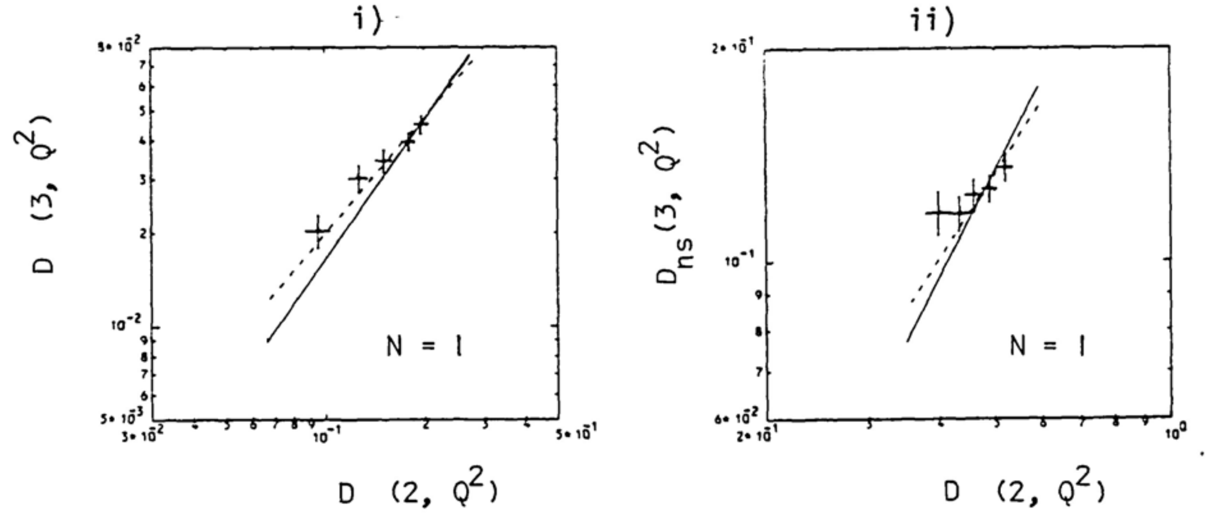

Fig 6.17b Log m vs log m' plot of, i) the negative hadron fragmentation functions (D^-) and ii) of the combination ($D^+ + D^-$). (Straight lines as above for non-singlet case).

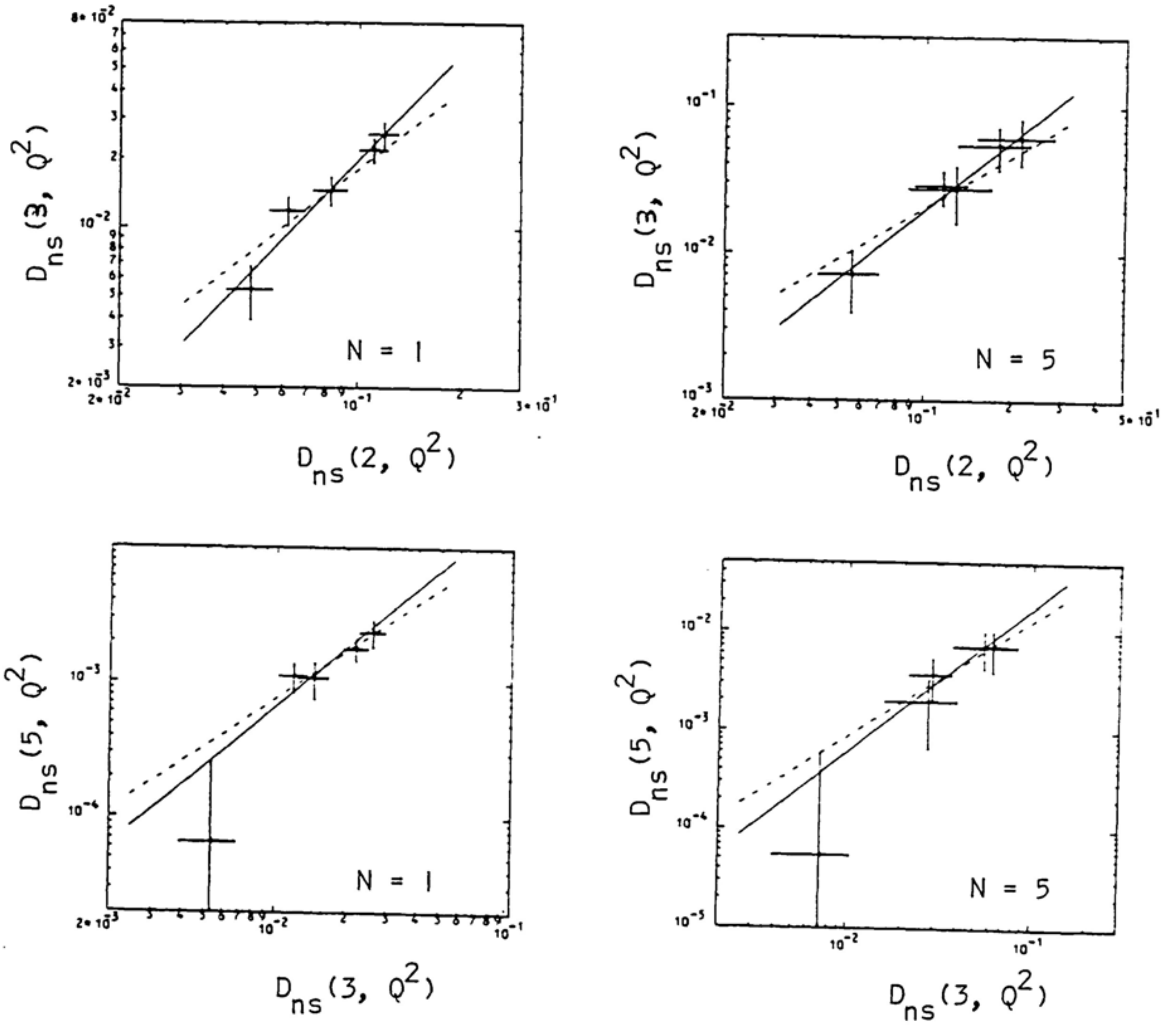

Fig 6.18 Log m vs log m' plot of non-singlet x_t moments. Straight lines have gradients given by vector gluons with anomalous dimensions d_{ns} (solid) and $d_{ns} + 1$ (dotted).

Since the moments of the fragmentation functions are highly correlated (especially for values of m, m' which are close together), log vs log plot for the moments may not be very informative. In order to check the correlations of the moments the negative hadron functions D^-, and the approximately singlet combination $(D^+ + D^-)$ are shown in Fig 6.17b, (positive hadron functions, D^+, show very little q^2 variation). Both D^- and $(D^+ + D^-)$ moments produce gradients which differ from that of the non-singlet combination assuming vector gluons, so that information about the non-singlet z moments is obtained. Thus by looking at such plots of non-singlet x_t moments a check on the anomalous dimensions of x_t can be made.

The different x_t moments are shown plotted against each other in Fig 6.18 for low and high values of n. The data does not distinguish between d_{ns} and $d_{ns} + 1$. (Although an apparent preference is shown for d_{ns} at low m, m', this is not the case at high m, m').

6.10 Higher Twist effects

In the convential perturbative QCD (and parton model) approach to lepton scattering, the initial and final scattered quarks are considered free and on-shell. However in certain kinematical regions the effect of off-shell quark fragmentation, leading to bound state effects in the observed pions, is expected to contribute significantly to the cross-section |11|:

$$\sigma\ (z,\ q^2) \propto (1 - z)^2 + \frac{4}{9}\ (1 - y)\ \frac{p_t{}^2}{q^2} \qquad (13)$$

through diagrams such as:

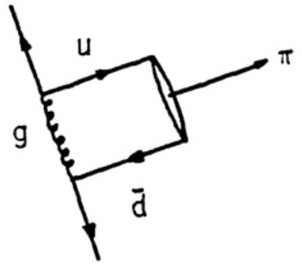

At low q^2 and large z the second term in equation (13), representing the non-scaling, non-factorising part of the non-perturbative cross-section becomes important and implies a dependence of the cross-section on y.

The fragmentation functions of positive and negative hadrons are shown in Fig 6.19 at low and high q^2 for $y \lesssim 0.5$. The positive and negative hadron functions show similar behaviour with z, at low and high values of q^2. There is no evidence of a y dependence, in particular in the low q^2 high z region. Thus the higher twist effects, which are expected to contribute terms giving a $1/q^2$ dependence to the moments of the fragmentation function (which is similar to the $1/\ln(q^2)$ predicted by perturbative QCD) are absent.

Summary

Factorisation, and scaling, of the single particle inclusive cross-section predicted by the QPM have been observed to breakdown, in qualitative agreement with leading order perturbative QCD. Factorisation is however restored if x, q^2 in $D_q^h(x, q^2)$ are replaced by w^2. The size of the factorisation breakdown, as measured by the ratio of double moments (R_1, R_2), is in quantitative agreement with the predictions of next to leading order QCD in the intermediate q^2 range, but the predicted symmetry in m and n of the factorisation breakdown is not observed in the data.

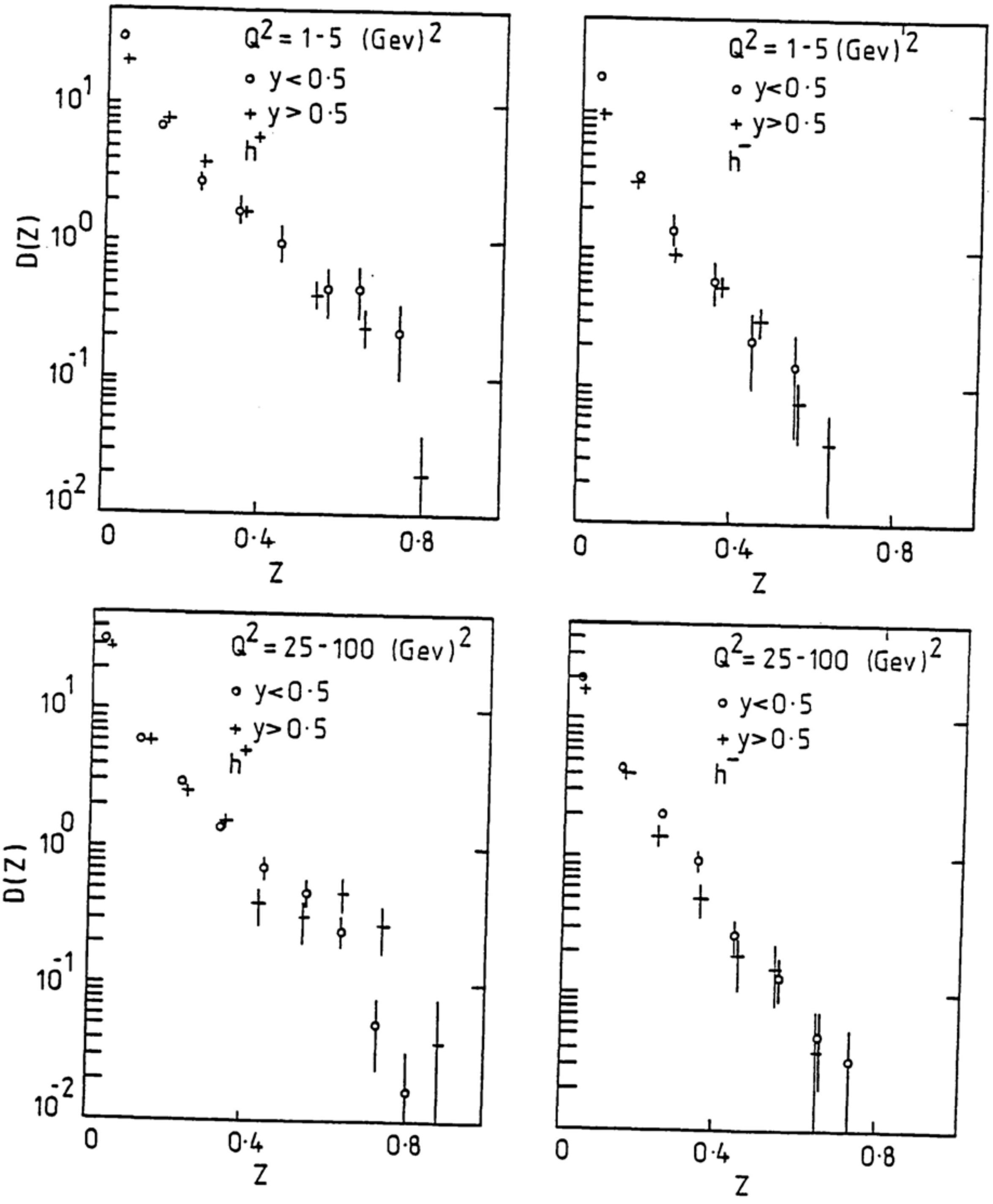

Fig 6.19 Y dependence of positive and negative hadron fragmentation functions at fixed Q^2.

The data does not show a clear preference between d_{ns} and d_{ns} + 1 for the anomalous dimension of x_t moments, and shows no evidence of contributions from higher twist effects due to bound states.

References

1 P C Bosetti et al, ABCLOS Collaboration, Nucl. Phys. B142 (1978) 1-28

2 R P Feynmann, Photon Hadron Interactions, (Benjamin Reading 1972)

3 J Sheiman, Nucl. Phys. B167, 125 (1980)

4 C Chao-hsi, Ref. TH 2736-CERN

5 W G Scott, CERN/EP 79-65

J Ellis et al, Ref. TH 2595-CERN

6 J Blietchau, Phys. Lett. Vol. 87B no. 3

7 T Umatseu, Phys. Lett. Vol. 79B no. 1,2

J F Owens, Phys. Lett. Vol. 76B no. 1 (1978) 85

G Altarelli, Nucl. Phys. B126 (1977) 298-318

8 N Saki, Phys. Lett. 85B (1979) 67

G Altarelli et al, Nucl. Phys. B160 (1979) 301

9 W A Bardeen et al, Phys. Rev. D18 (1978) 3998

10 D W Duke, The Importance of Asymptotic Freedom Beyond Leading Order, Rutherford Laboratory Preprint (1979)

11 E L Berger, Phys. Lett. Vol. 89B no. 2 (1980) 241

C Matteuzzi, paper submitted to the Third Warsaw Symposium, May 1980

Conclusions

The QPM picture of leptonic interactions has been found to be insufficient in describing the final state hadrons resulting from neutrino interactions. First order QCD provides qualitative (and in the case of transverse momentum distributions quantitative) agreement with the experimental data, although no evidence of hard gluon emission has been observed. The non-factorisation of the single particle inclusive cross-section indicates that second (and possibly higher) order QCD corrections are important. However, perturbative QCD calculations do not describe the momentum space structure of final state hadrons. This is due to the low order of present calculations, and the dominance of non-pertubative effects that have been observed.

General agreement between neutrino interactions, k^-p hadronic interactions, and e^+e^- annihilations has been observed. This indicates that the non-perturbative process which converts the elementary parton fields into observed hadrons is similar in all these processes.

Appendix 1

A Monte Carlo program due to A Grant has been used to generate inclusive narrow-band beam spectrum neutrino events within the fiducial volume of BEBC. The out-going lepton is generated assuming a spin ½ quark-model and assuming a form for the structure functions $F_2(x) = s(1 - x^2)^3$, x being the Bjorken variable and s the square of the centre of mass energy of the event.

Hadrons are generated from an interpolation of νH_2 data from BEBC (WA 21), the relevant features of the hadron generation being:

a) The p_t distribution is generated assuming the form:

$$f(p_t) = \frac{p_t}{b} \exp(-p_t/b) \qquad b = \langle p_t \rangle / 2$$

The mean p_t being obtained from the tabulated correlation between X_F and $\langle p_t \rangle$, 'seagull effect' of the WA 21 data, which is very similar to the WA 19/47 νNe data.

b) Smearing of track quantities. This is obtained by following each track out from the vertex until it interacts or stops or leaves the chamber, neutrons being allowed to interact and gammas to convert. From the measured lengths of the tracks errors are computed using the formalism of ref |1|, and the momentum p, dip λ, and azimuth ϕ of the tracks randomised according to the calculated errors.

c) The loss of neutral energy observed in Ne/H_2 data is reproduced by allowing 20% of the event energy to be lost through undetected neutrals.

An extra 1 metre has been added to the length of the muon track for EMI improvement of its momentum determination. The formalism used reproduces well in the mean the $\Delta(1/p)$ distributions for hadrons and μ, and $\Delta\phi$, $\Delta\lambda$ distributions for hadrons. However the $\Delta\lambda$, $\Delta\phi$ distributions for the μ are produced with almost twice the mean values observed in the data, leading to a pessimistic determination of the lepton plane compared to the data. The $\Delta p/p$ distributions for the hadrons is also well reproduced, whilst for the μ the mean is larger than observed in the data. (The various quantities are shown in the table).

	MUON		HADRONS	
	Data	Monte Carlo	Data	Monte Carlo
$\langle\Delta(1/p)\rangle$ Gev^{-1}	1.3	1.9	0.06	0.06
$\langle\Delta\lambda\rangle$ mrad	0.87	1.7	8.8	8.1
$\langle\Delta\phi\rangle$ mrad	0.84	1.4	9.1	9.3
$\langle\Delta p/p\rangle$	0.048	0.057	0.11	0.12

References

1 A Grant, European Committee for Future Accelerators, CERN/ECFA/72/4 vol I, 46

Appendix 2

The q^2 dependence of fragmentation functions is given by the set of diagrams |ref 7 of chapter 6|:

a)

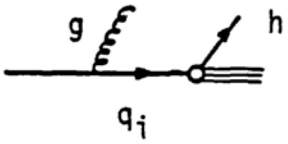

b)

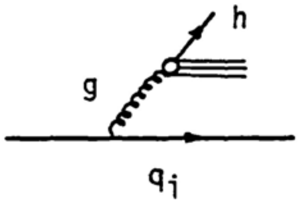

c)

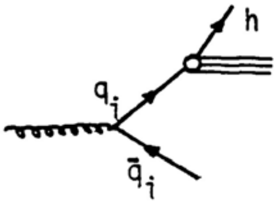

d)

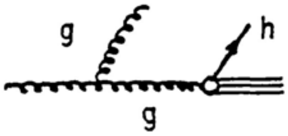

which correspond to:

- a) The fragmentation of a quark q_i emitting a gluon via the decay of q_i into a hadron h. This can be expressed symbolically: $p_{qq}\ D^h_{q_i}$.
- b) The fragmentation of q_i through a gluon represented by $p_{gq}\ D^h_g$.
- c) Gluon fragmentation caused by a q_i-$\bar{q}_i$ pair creation and the subsequent decay of q_i, represented by $p_{qg}\ D^h_{q_i}$.
- d) The gluon fragmentation by a three gluon vertex, given by $p_{gg}\ D^h_g$.

where p_{ij} (z/y), i, j = q, g are the transition probabilities for the process q or g ↔ q or g with initial/final fractional momentum y/z and $D^h_{q_i}$ (z, q^2), (D^h_g (z, q^2)) are the probability distributions for a quark q_i (gluon g) produced at q^2 to decay into a hadron h carrying a fraction z of the quark (gluon) momentum.

These processes are described by the set of integro-differential equations:

$$\frac{\partial}{\partial t} D^h_{q_i}(z, t) = \alpha(t) \int_z^1 \frac{dy}{y} \left[P_{qq}(z/y)\, D^h_{q_i}(y, t) + P_{gq}(z/y)\, D^h_g(y, t) \right] \tag{1}$$

$$\frac{\partial}{\partial t} D^h_g(z, t) = \alpha(t) \int_z^1 \frac{dy}{y} \left[P_{qg}(z/y) \sum_{i=1}^{2m} D^h_{q_i}(y, t) + P_{gg}(z/y)\, D^h_g(y, t) \right] \tag{2}$$

where m = number of flavours (label i runs over q and $\bar{q}$ of all flavours) and t = $\ln(Q^2/Q_0^2)$, Q_0 being a suitable momentum scale.

The effective coupling constant in QCD, $\alpha(t)$ is defined:

$$\alpha(t) = \frac{\bar{g}^2(Q^2)}{4\pi} = \frac{g_0^2}{4\pi\,(1 + \frac{1}{2} b_0 g_0^2 t)}$$

$$= \frac{\alpha(0)}{[1 + \alpha(0)\, 2\pi\, b_0\, t]}$$

g_0 being the coupling constant renormalised at Q_0^2.

$$b_0 = \frac{33 - 2m}{24\pi^2}$$

The equations (1) and (2) are setup in analogy to the equivalent set of equations for the structure functions, which are based on the operator product expansion (OPE). There is no such rigorous treatment available for the fragmentation function moments, and these equations are assumed to be valid on the assumption that the formalism which describes quarks in hadrons should equally describe hadrons in quarks.

For the simpler case of a non-singlet fragmentation function (obtained by considering the differences of equations 1 for various i and j (i ≠ j)) where only diagram (a) contributes the q^2 dependence given by equation (1) simplifies to:

$$\frac{\partial D}{\partial t} (x, t) = \alpha(t) \int_x^1 \frac{dy}{y} D (y, t) \, p_{qq} (x/y)$$

where $D = D_q - D_{\bar{q}} = D_{ns}$

This can be solved by taking the (n -1)th moment with respect to x:

$$\frac{d}{dt} D^n_{ns} (x, t) = \alpha(t) \int_0^1 dx \, x^{n-1} \int_x^1 \frac{dy}{y} D (y, t) \, p_{qq} (x/y)$$

$$= \alpha(t) \int_0^1 dz \; z^{m-1} \; p_{qq} \, D^n_{ns} (q)$$

$$\frac{d}{dt} D^n_{ns} (z, t) = \alpha(t) \, D^n_{ns} (q^2) \; A^n_{ns} \qquad (3)$$

where $z = x/y$

$$D^n_{ns} = \int_0^1 y^{n-1} \; D (y, t) \, dy$$

$A^n_{ns} = \int_0^1 dz \; z^{m-1} \; P_{qq}(z)$ are the non-singlet anomalous dimensions given by:

$$A^n_{ns} = \frac{1}{3\pi}\left[1 - \frac{2}{n(n+1)} + 4\sum_{j=2}^{n}\frac{1}{j}\right]$$

Integrating equation (3) yields for the n'th non-singlet moment:

$$\frac{d\,D^n_{ns}}{D^n_{ns}} = \frac{1}{2\pi\, b_o}\; A^n \;\frac{dt}{t}$$

$$\Rightarrow \qquad D_n(t) = D_n(o)\left[\frac{\alpha(t)}{\alpha(t_o)}\right]^{-\frac{A^n}{2\pi\, b_o}}$$

$$\text{ie} \quad D_n(q^2) = \text{CONST}\left[\frac{1}{\ln(q^2/\Lambda^2)}\right]^{-d^n_{ns}}$$

$$\text{where} \quad d^n_{ns} = \frac{A^n}{2\pi\, b_o} = \frac{4}{33-2m}\left[1 - \frac{2}{n(n+1)} + 4\sum_{j=2}^{n}\frac{1}{j}\right]$$

(In the case of scalar gluons only the first two terms contribute to the anomalous dimensions).

ACKNOWLEDGEMENTS

Thanks are due to a large number of people who have contributed at various stages of this experiment, both at CERN and at Imperial College. Also I have benefited from discussions with many colleagues from the ABCLOS Collaboration, and from help and advice of Dr K W J Barnham.

I am grateful to Prof. I Butterworth for offering me the opportunity to work in the H E N P group at Imperial College, and the S R C for financial support. I thank Dr D B Miller for acting as my supervisor.

Finally, I should like to thank Ninder for the excellent typing of this thesis.